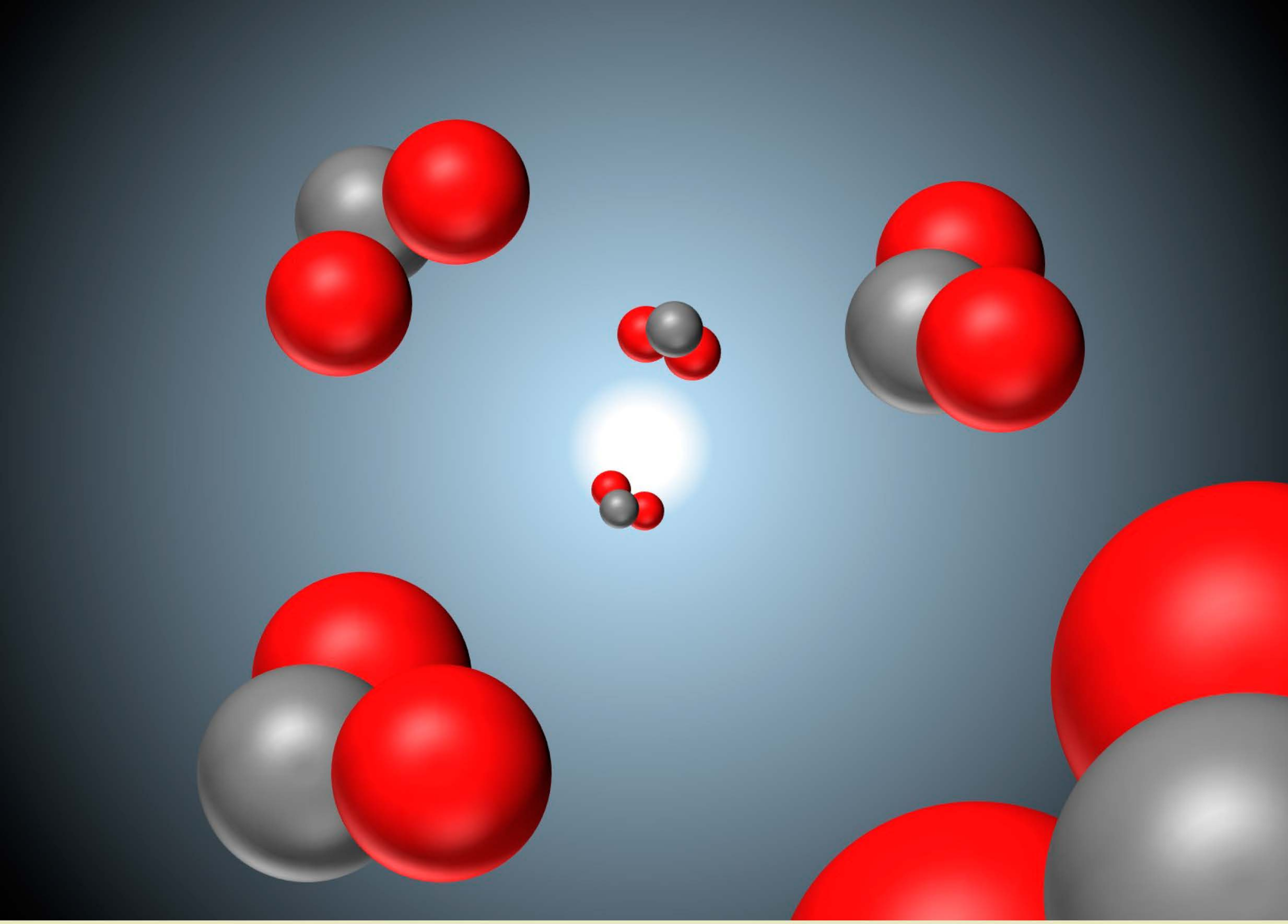

Pedro Manuel Crispim da Costa da Encarnação

Ion Mobility Studies
Mixtures used in Gas Detectors

Master's thesis in the scientific area of Physics Engineering, supervised by Professor Doctor Filipa Isabel Gouveia de Melo Borges Belo Soares and Master André Filipe Ventura Cortez and submitted to the Department of Physics, Faculty of Science and Technology, University of Coimbra

July 2016

UNIVERSIDADE DE COIMBRA

Faculty of Science and Technology
University of Coimbra

• U  C •

Ion Mobility Studies
Mixtures used in gas detectors

Pedro Manuel Crispim da Costa da Encarnação

Final Dissertation for MSc degree in Physics Engineering supervised by
Doctor Filipa Isabel Gouveia de Melo Borges Belo Soares
Eng. André Filipe Ventura Cortez

2016

Supertramp, 1982

”Don’t leave me now
Leave me out in the pouring rain
With my back against the wall
Don’t leave me now
Don’t leave me now

Leave me out with nowhere to go
And the shadows start to fall
Don’t leave me now
Don’t leave me now

Leave me out on this lonely road
As the wind begins to howl
Don’t leave me now
Don’t leave me now

All alone on this darkest night
Feeling old and cold and grey
Don’t leave me now
Don’t leave me now

Leave me holding an empty heart
As the curtain starts to fall
Don’t leave me now
Don’t leave me now
All alone in this crazy world”

In memory of my beloved father

Acknowledgements

The completion of this works is a milestone of one of the most important moments of my academic journey, marking the end of one stage of my life and the beginning of different challenges that lay ahead. However, it would not have been possible for me to get where I am today without the help and support of many people, to whom I would like to express my deepest gratitude.

To Professor Doctor Filipa Borges, who supervised this dissertation, for the constant advice and help, for the continuous support and cheerful words of encouragement, to which I owe a substantial part of my success achieved at LIP. I would also like to leave in writing my appreciation for trusting me with this project, that gave me the opportunity to expand my horizons in many levels.

To Engineer André Cortez, who co-supervised this work, for being an example of dedication and for always being available to share valuable knowledge, essential to the progress of this work. A special thank you for the support and friendship throughout my academic years, and for bringing me into the LIP family.

To Professor Doctor Filomena Santos, for the availability to provide insight regarding this project for numerous times, and for the scientific experience shared, which was a valuable contribution for the development of my work.

To Master Alexandre Trindade who played an important role in my adaptation to the work at the laboratory, for the hours spent tutoring me and for always being available to answer my questions and to help me whenever I needed.

To Doctor José Escada, for being available to share his expertise on this subject, thus enriching the scientific production generated within this project.

To Professor Doctor Carlos Conde, for the time spared to convey words of wisdom and his contagious passion for physics.

To Marco and Miguel, for your companionship, for the delightful conversations and friendly character, which helped to maintain an excellent work environment.

To Doctor Pedro Cidónio and CEMDRX, for the patience and technical help provided for the examination of the GEM conditions conducted by SEM analysis.

To Mr. Américo Pereira and to Doctor Fernando Amaro for the execution of tech-

nical tasks on the detector, namely the cleaning of the GEM and the deposition of the CSI photocathode, respectively.

To FEDER, through Programa Operacional Factores de Competividade-COMPETE and by National funds through FCT- Fundação para a Ciência e Tecnologia for the grant attributed between December of 2014 and June of 2015 in the frame of Project QREN n. 4825, Rad for Life.

To Soraia, Rodrigo and Micael, whose friendship survived the test of time and for always being there for the moments that really matter.

To my friends, Mariana, Francisco, Daniel, André P., Bruno, Olivier, Joana, André S., Isaac, Sara, Fátima, Trenk, Bastos and many others who I had the pleasure to know during this six years. Thank you for the unforgettable moments of fun, for all the support and for the life-long friendships that I take from here.

To my football teammates and UFC Palito, for all the good moments shared in the field, and for the titles that we conquered together;

To Patricia's family, for all the encouragement and kindness shown over this years, and for the support manifested at one of the hardest times of my life.

In the last four paragraphs I would like to thank my family. To you, I owe who I am today. Thank you for being present.

To my great mother, for making everything easier, for the amazing joyful presence. Thank for your concern, your love, your strength, for the values that you taught me and for always being there when I needed. I will be eternally grateful.

To my brother for being a role model to follow, you are the most hard-working person I know. Thank you for all the support and encouragement to pursuit my goals, and for making me see that with perseverance nothing is out of your reach.

To my Patrícia for being the light in a dark and curvy road. Thank you for your love, for understanding me, for being kind and generous and taking care of me. You are unique.

And to you I dedicate this work, because despite not having been with me at the finish line, you've been by my side through every step of my life. It is not the destiny that defines you, it is the journey, and I am glad to have had you by my side to guide me. Thanks for all the support and for all that you gave up for me and João; and for helping me to fulfil my dream. I know you are still here with me and you will give me strength to overcome the journeys ahead.

To all of you that contributed to the end of this journey in so many different levels, a sincere thank you.

Abstract

Time Projection Chambers (TPC) allow a three-dimensional reconstruction of a particle trajectory or interaction that uses a sensitive gas as detection medium. This detectors have large volumes, and for an appropriate and improved operation it is essential to understand what is the detector's behaviour if the gas parameters such as composition, pressure, temperature and type of gas are changed.

In the scope of our participation in the RD51 collaboration/CERN, a common project was established with GSI Darmstag (Germany), Uludağ University (Turkey) and VECC (India) regarding the study of ion transport properties of relevant gas mixtures for ALICE TPC. With this in mind, we performed experimental ion mobility measurements, K_0, for several gases and gas mixtures, namely for pure carbon dioxide, carbon dioxide mixtures (Ar-CO_2, Ne-CO_2, Ne-CO_2-N_2 and N_2-CO_2), pure nitrogen, nitrogen mixtures (Ne-N_2), pure trimethylamine (TMA) and xenon-trimethylamine (Xe-TMA) mixtures. The results are presented for total pressures ranging from 4-20 Torr and for reduced electric fields (E/N) generally in the 10-25 Td range (6 to 60 Td in the case of pure gases), at room temperature.

The IDC (Ion Drift Chamber) used to conduct the ion mobility studies was initially developed by P. N. B. Neves [4]. The techniques to perform the aforementioned studies are described in this report and make used of a Gaseous Electron Multiplier (GEM) and a UV flash lamp to produce the ions.

Also, a new, more practical and automatic method of analysis was developed in the form of a standalone application during this thesis program, which is also explained in this document. Finally, a redesign of the experimental system in order to improve it is suggested.

Keywords: Charge transport and multiplication in gas; Ion sources (positive ions, negative ions); Gaseous detectors; Ionization and excitation processes; Ion mobility.

Resumo

As TPC (*Time Projection Chambers*) permitem fazer uma reconstituição tridimensional da trajetória ou interação de uma partícula usando um gás sensível como meio de deteção. Estes detetores têm um volume elevado, e para que o seu funcionamento seja adequado e possa ser melhorado é essencial compreender qual é a resposta do detetor ao mudar os parâmetros relativos aos gases, tais como composição, pressão, temperatura e tipo de gás.

No âmbito da nossa participação na colaboração RD51/CERN, foi estabelecido um projeto comum com a GSI Darmstag (Alemanha), Universidade de Uludağ (Turquia) e VECC (Índia) que se focou no estudo de propriedades de transporte de iões de misturas gasosas relevantes para o ALICE TPC. Tendo isto em consideração, foram efetuadas medidas experimentais de mobilidade de iões, K_0, para vários gases e misturas gasosas, nomeadamente para dióxido de carbono puro, misturas de dióxido de carbono (Ar-CO_2, Ne-CO_2, Ne-CO_2-N_2 e N_2-CO_2), azoto puro, misturas de azoto (Ne-N_2), trimetilamina pura (TMA) e misturas de xénon-trimetilamina (Xe-TMA). Os resultados são apresentados para pressões totais que variam entre 4-20 Torr e campos elétricos reduzidos (E/N) geralmente entre 10-25 Td (6 a 60 Td no caso dos gases puros), à temperatura ambiente.

A IDC (*Ion Drift Chamber*) usada para efetuar os estudos de mobilidade de iões foi inicialmente desenvolvida por P.N.B. Neves. As técnicas para a realização dos estudos anteriormente mencionados são descritas neste documento e fazem uso de um GEM (*Gaseous Electron Multiplier*) e uma lâmpada de flash UV para produzir os iões.

Para além disto, um novo método de análise mais prático e automático foi desenvolvido sob a forma de uma aplicação standalone durante o programa desta dissertação, e está também explicado neste documento. Finalmente, foram propostas alterações ao sistema experimental de forma a melhorá-lo.

Palavras-chave : Transporte de cargas e multiplicação em gases; Fontes de iões (iões positivos, iões negativos), Detetores gasosos; Processos de ionização e excitação; Mobilidade de iões.

Publications

Scientific Papers

1. P. M. C. C. Encarnação *et al*, Experimental ion mobility measurements in Ne-CO_2 and CO_2-N_2 mixtures," *Journal of Instrumentation*, vol. 11, no. 05, pp. P05005-P05005, 2016.

2. P. M. C. C. Encarnação *et al*, Experimental ion mobility measurements in Ar-CO_2 mixtures," *Journal of Instrumentation*, vol. 10, pp. P01010-P01010, 2015.

Conference Papers

3. A. F. V. Cortez, P. M. C. C. Encarnação *et al*, "Ion mobility measurement in gas mixtures", ION2016 XIth International Conference Ion Implantation and Other Applications of Ions and Electrons, Lublin University of Technology and Wrocław University of Technology, 13th to 16th June 2016, Kazimierz Dolny, Poland

4. P. M. C. C. Encarnação *et al*, "Experimental ion mobility measurements in Ar-CO_2 and Ne-CO_2 mixtures", DCE 2015, 11th-12th, Universidade do Porto, Portugal

Oral communications

5. A. F. V. Cortez, P. M. C. C. Encarnação *et al*-, "Ion mobility measurement in gas mixtures", ION2016 XIth International Conference Ion Implantation and Other Applications of Ions and Electrons, Lublin University of Technology and Wrocław University of Technology, 13th to 16th June 2016, Kazimierz Dolny, Poland

6. P. M. C. C. Encarnação *et al*, "Ion transport in Nitrogen based mixtures", oral presentation, IWAD and 17th RD51 Collaboration Meeting, 8th to 11th of March 2016, CERN, Switzerland

7. P. M. C. C. Encarnação *et al*, "RD51 Collaboration - Ion mobility study of mixtures used in gas detectors", oral presentation, Jornadas Científicas do LIP, 19^{th}-21^{st} February 2016, Universidade do Minho, Braga, Portugal

8. P. M. C. C. Encarnação *et al*, "Ion transport in CO_2-N_2 mixtures", oral presentation, IWAD and 16^{th} RD51 Collaboration Meeting, 16^{th} to 17^{th} of October 2015, CERN, Switzerland

9. P. M. C. C. Encarnação *et al*, "Ion mobility in Ne-CO_2-N_2 mixtures", oral presentation, 15^{th} RD51 Collaboration Meeting, 18^{th} to 20^{th} of March 2015, CERN, Switzerland

10. P. M. C. C. Encarnação *et al*, "Ion mobility in Relevant Gas Mixtures- A Review", oral presentation, IWAD and 14^{th} RD51 Collaboration Meeting, 27^{th} to 31^{st} of October 2014, Kolkata, India

11. A. F. V. Cortez *et al*, "Ion mobility measurement in gases", oral presentation, Café com Física (Dep.Física / Univ. de Coimbra), 26^{th} of March 2014, Coimbra, Portugal

12. A. F. V. Cortez *et al*, "Ion mobility measurement in Ar-CO_2 mixtures", oral presentation, RD51 Collaboration Mini-week, 16^{th} to 19^{th} of March 2014, CERN, Switzerland

13. A. F. V. Cortez *et al*, "Ion mobility measurement", oral presentation, 13^{th} RD51 Collaboration Meeting, 2^{nd} to 5^{th} of February 2014, CERN, Switzerland

Poster communications

14. P. M. C. C. Encarnação *et al*, "Experimental ion mobility measurements in Ar-N_2 mixtures", 2016 IEEE Nuclear Science Symposium, Medical Imaging Conference and Room-Temperature Semiconductor Detector Workshop, 29 Octoberth to 6^{th} November 2016, Strasbourg Congress Center Palais Des Congres, Strasbourg, France

15. P. M. C. C. Encarnação *et al*, "Ion mobility study mixtures used in gas detectors", poster communication, Avaliação Intercalar, 17^{th} of February 2016, Universidade de Coimbra, Portugal

16. P. M. C. C. Encarnação *et al*, "Experimental ion mobility measurements in Ar-CO_2 and Ne-CO_2 mixtures", poster communication, DCE 2015, 11^{th}-12^{th}, Porto, Portugal

17. A. F. V. Cortez *et al*, "Ion mobility measurement in Ar-CO_2 mixture", poster communication, Física 2014- 19ª Conferência Nacional de Física, 2^{nd}-4^{th} September 2014, Lisboa, Portugal

Contents

List of Figures

List of Tables

Nomenclature

α neutral polarisabily ($\AA$)

μ ion-neutral reduced mass (u)

ALICE **A** **L**arge **I**on **C**ollider **E**xperiment

Ar Argon

C_2H_6 Ethane

CF_4 Tetrafluoromethane

CH_4 Methane

CMS **C**ompact **M**uon **S**olenoid

CO_2 Carbon Dioxide

CsI **C**aesium **I**odide

E/N Electric Field (SI units-V/m)

E/N Reduced Electric Field - normally express in Td (1 Td = 10^{-21}) V.m^2

GEM **G**as **E**lectron **M**ultiplier

k Rate Constant

K_0 Reduced mobility (common units cm^{2}V^{-1}s^{-1})

M Neutrals Mass (u)

m Ions Mass (a.u.)

MSE **M**ean **S**quare **E**rror

N Gas number density

N_0 Loschmidt number - 2.6867 $\times 10^{25}$ m^{-3}

N_2 Nitrogen

Ne Neon

QE **Q**uantum **E**fficiency

SEM **S**canning **e**lectron **m**icroscope

SNR **S**ignal **N**oise **R**ation

TMA Trimethylamine

$Torr$ is a unit of pressure based on an absolute scale. 1 Torr = 1/760 atm $\approx$ 133.3 Pa

TPC **T**ime **P**rojection **C**hamber

UV **U**ltra**v**iolet

v_d Drift Velocity (SI units-m/s)

$VECC$ **V**ariable **E**nergy **C**yclotron **C**entre

Xe Xenon

Chapter 1

Introduction

1.1 Brief History

The first studies on ion mobility and the development of the early analytical tools occurred between the last decade of the 19^{th} century and throughout the first 3 decades of the 20^{th} century. This innovation period is the result of studies carried out by research centers in England and Germany on electrical discharges occurring in air or other gases at atmospheric pressure, from which it was concluded that the gases could pass from insulators to electric current conductors through various processes. In this period, it was determined that the conductivity present in the gas was caused by the formation of electrons and ions, leading to new research studies to determinate the mobility of these ions. Examples of these are experimental studies on the mobility of ions using X-rays, that were started by Rutherford [1].

On the theoretical side, in 1905 was published the first theoretical treatment of the ion mobility, which described the role of attractive forces of a charged particle on a neutral molecule and its influence on the mobility of ions in gases. This sophisticated treatment, based on the polarisation interaction, was developed by Paul Langevin and contributed to a better understanding of the experimental results of ion mobility in gases at atmospheric pressures [2]. In 1908, Chapman and Enskog developed a more general theory, that was later applied to the calculation of mobilities and diffusion coefficients. However, both are limited to spherically symmetric ion-molecule combinations [3].

In 1916 and 1918, Max Trauz and William Lewis, proposed independently, the collision theory that explains how chemical reactions occur and why reaction rates differ for different reactions [4]. The collision theory is based on the kinetic theory of gases and it is important to clarify the chemical species detected in experimental

systems with special attention for the ones that do not have a mass spectrometer.

Prior to 1930, only primitive experimental techniques were available to measure the transport properties of gases in electric fields. In these experiments, the impurities had a significant role in the gas samples used and led to conflicting results in mobility values obtained experimentally. Improvements in gas handling techniques and the development of new methods for measuring ionic mobilities resulted in reliable, reproducible data [3].

In the late 30's, Tyndall and his co-workers [5] from Bristol University made great progress in the experimental study of the drift velocity of ions. They accomplished an extensive and important series of mobility measurements by developing the four-gauze electrical shutter method. According to Loeb [6], this method was, at the time, the most reliable and the most widely used, with a high resolving power and that yielded mobility values with great accuracy, allowing the study of pure gases well below the atmospheric pressure. Twenty four years later, Beaty reproduced Tyndall's experiment and in order to improve the results, he took advantage on the advances in electronics and vacuum techniques. Neither Tyndall's nor Beaty's apparatus employed a mass spectrometer, however both systems were able to produce results that could easily be analysed and interpreted.

The transport theory for gaseous ions underwent a slow development up to the early 1950s, until Wannier published, in 1953, a theoretical work about the motion of ions in gases in the presence of strong electric fields. According to the author, for high E/N, the motion is assumed to be characterized by a constant mean free time and the total energy of the ion consists of three parts: thermal energy, drift energy, and random field energy [3].

In the early 60's, the development of the drift tubes (figure 1.1) represented a remarkable progress in the field of the characterization of mobility and mass identification of certain ions present in a gaseous mixtures, elucidating the complicated effects of chemical reactions between the ions and gas molecules. By the 70s', reliable data on ionic mobilities, and for the first time, on diffusion coefficients, started to appear for several gases and ions species.

After this, an important compilation of experimental data on ionic mobilities and diffusion coefficients for ions in neutral gases under an externally applied electric field at room temperature was performed by H. W. Ellis, R. Y. Pai, E. W. McDaniel, L. A. Viehland, E. A. Mason, M. G. Thackston, D. L. Albritton and S. L. Lin. This compilation has four parts, the first of which was published in 1976 and the last one made literature coverage of the experimental data up to 1995 [8–11]. Some of the data present in these

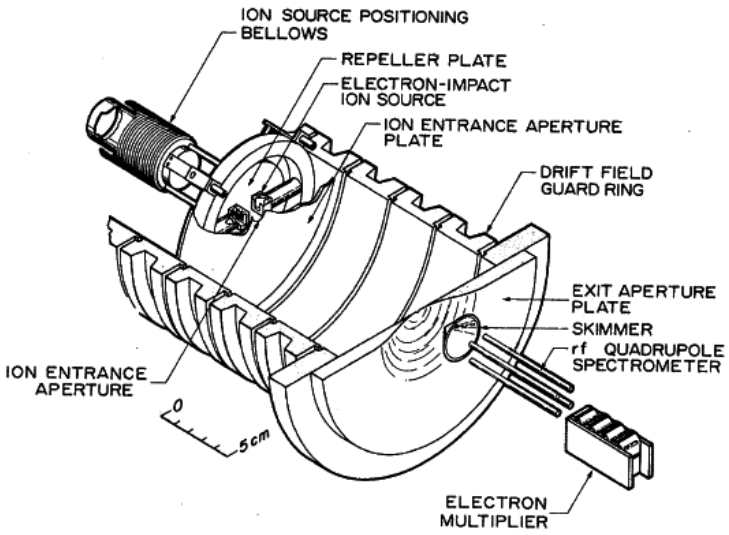

Figure 1.1: Schematic view of the basic component drift-tube mass spectrometer developed in the 60s at Georgia Institute of Technology. Picture taken from [7]

papers was used in this report in chapter 3 as comparison with our results.

Development of the ion mobility spectrometers and commercial applications

The development of the mobility-tube-mass-spectrometer, in early 60s', and a base-knowledge of the behaviour of ion-molecule interactions led to the development of a new method, the Ion Mobility Spectrometry (IMS). This method was designed for the identification of substances based on the drift velocity of gas-phase ions under an electric field, allowing the detection and identification of volatile and semi-volatile organic compounds [1].

The first modern analytical ion mobility spectrometers were introduced commercially in 1970 for military and security applications. With advances in technology, the IMS spectrometers began to have an increase in their detection sensitivity, speed of response and became portable, making their use possible in different areas, such as pharmaceutical and clinical analysis, safety (drug detection), food analysis, environmental analysis, process monitoring, space exploration or medical uses [12]. For example, explosives are highly detectable due to the presence of electronegative nitrated derivatives. In the case of drugs, they contain amido groups, and therefore exhibit high affinity to form positive ions, facilitating their detection.

As an example, SmithsDetection ® is one of the companies that uses IMS technology in several commercial and military applications. Examples of portability and

((a)) Sabre5000 ((b)) GID-3 SIM

Figure 1.2: Commercial examples of recent ion mobility spectrometers.

applicability of this technology are SABRE 5000 and GID-3, shown in figure 1.2. The first is a portable detector that can identify traces of explosives, chemical agents, industrial products and narcotics. It is capable of detecting more than 40 hazardous substances (such as volatile and unstable chemicals used for making home-made explosives, for instance ammonium nitrate) in approximately 20 seconds. The GID-3 is a detector of chemical warfare agents that allows the detection of toxic chemicals to life such as neurotoxins, hemotoxins and toxins aggressive to the skin and respiratory system. It was developed for military scenarios and can be used in war vehicles.

1.2 Theoretical Background

In this section, we introduce theoretical information relevant for the following chapters and in figure 1.3 is depicted a flowchart that shows the connection between the theoretical concepts present throughout this section.

1.2.1 Ion transport properties-Mobility

In the absence of an electric field, the movement of ions occurs in the opposite direction of the concentration gradient of these ions in the gas, this phenomenon is named diffusion. If an external electric field is applied, the ions will then move according to the field, and in the case of positive ions, they will move in the direction of decreasing potentials. In this situation, depending on the intensity of the reduced electric field (E/N), which is the intensity of the field divided by the number gas density, usually expressed in Townsend (Td) units (1 Td = 10^{-21} V.m^2), the mobility of the ions could depend of this quantity.

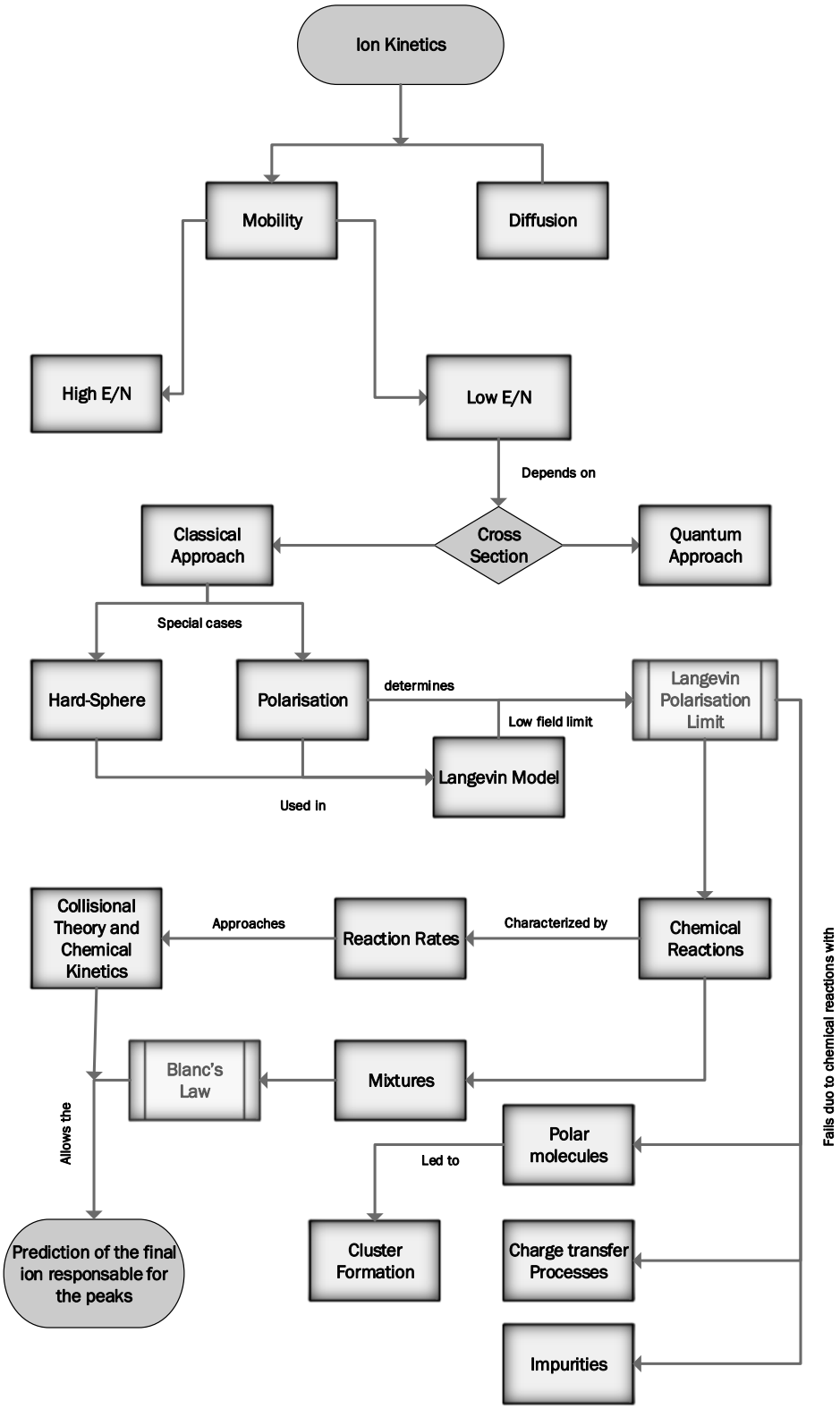

Figure 1.3: Flowchart describing the relationship between the concepts stated in this chapter.

In the low field region the ion drift energy is small compared to the thermal energy and, in this case, K_0 is independent of E/N and has a magnitude called the zero-field mobility. One of the theories that describes the zero-field mobility, where the polarisation is the main interaction, is the Langevin model, discussed in section 1.2.2.

When a group of ions is originated in a weakly ionized gas moving under a uniform electric field, the ions collide with the neutral molecules of the gas, losing energy in the collisions and gaining/losing energy from the electric field. Depending on the collision cross section and on the electric field intensity a steady state will eventually be reached. In this case the average speed of this group of ions, also called drift velocity, v_d, is directly proportional to the electric field intensity, as expressed by the following equation:

$$v_{\mathrm{d}} = KE \tag{1.1}$$

where K is the mobility of the ions and E the intensity of the drift electric field. In the literature, the ion mobility, K, is frequently expressed in terms of the reduced mobility K_0, as follows

$$K_0 = KN/N_0 \tag{1.2}$$

where N is the gas number density and N_0 is the Loschmidt number ($N_0 = 2.6867 \times 10^{25}$ m^{-3}).

Since the ions' mass is usually close to the molecular one, only a few collisions are necessary for the ions to reach a steady-state condition after the electric field is applied [3].

Concerning the dependence of the ion mobility on E/N, there are several accurate transport theories, described in [3, 13]. According to the authors, the transport theory was developed along two different approaches which lead to identical results (Boltzmann - Enskog method and Maxwell - Chapman method). Both theories predict the validity of the equation 1.1 in the low-field region where the energy is close to thermal, justifying its use. This was also proven in a review article performed by H. E. Revercomb and E. A. Mason [14].

1.2.2 Langevin Polarization Limit

In Langevin's theory [2], three assumptions are made. First, both ions and atoms/molecules of the gas act like elastic spheres, being the atoms/molecules polarisable in the field of the ions. Second, the interactions between atoms and ion only have two origins: the polarisation attraction and the hard sphere repulsion. Finally, the velocity distribution of ions and molecules is considered a Maxwell-Boltzmann distribution.

The Langevin limit corresponds to the value of K_0 in the double limit of low E/N and low temperature, conditions which ensure the dominance of the polarization attraction over the hard sphere repulsion. This limit is given by equation 1.3,

$$K_0 = 13.88\left(\frac{1}{\alpha\mu}\right)^{\frac{1}{2}} \tag{1.3}$$

where α is the neutral polarisability in cubic angstroms ($\AA^3$) and μ is the ion-neutral reduced mass (a.u.), described by equation 1.4, wherein M and m are the neutral and ions' mass, respectively.

$$\mu = \frac{mM}{m+M} \tag{1.4}$$

The Langevin limit can be obtained from the low-field expression for K and from the calculation of the corresponding collision integral, assuming that the polarisation is the only interaction taking part in the ion-neutral collisions. The deduction of this expression can be found in [4].

An aspect to be noticed is that if the polarisation attraction is already dominant at room temperature, a limiting value for the mobility at room temperature is also expected. A decrease in the temperature only increases the predominance of the polarisation interaction, though not significantly [15].

Usually, equation 1.3 gives values of ionic mobilities that are in good agreement with experimental observations at room temperature. However, there are some deviations from the Langevin limit that are usually attributed to chemical reactions with impurities or the presence of charge transfer processes, defined in section 1.2.3.

1.2.3 Charge Transfer

A charge transfer reaction is a reaction between an ion (A) with a neutral (B) or collision partner ion in which some or all of the charge on the reactant ion is transferred to the neutral or collision partner ion.

$$A^+ + B \rightarrow A + B^+ \tag{1.5}$$

if A and B are identical atoms, it is called a resonant charge transfer (eq.1.6).

$$A^+ + A \rightarrow A + A^+ \tag{1.6}$$

Usually, this type of reaction, although not changing the original ion tends, to delay the final ion, reducing its mobility value. This process is often given as a justification

for the discrepancy between the mobility of a detected ion and the prediction given by the Langevin limit.

1.2.4 Clusters

Cluster ions are composed by a central ion with one or more neutral atoms and molecules. They bind together by the attractive force between the ion charge and the induced molecules. Typically the binding energy between them is in 0.1 – 1.5 eV range, in the middle of chemically bound molecules and van der Waals molecules[16]. The formation of a most simple cluster, with only one neutral, being in the same species as the ion, is described by chemical equation 1.7.

$$A^+ + A + M \rightarrow A.A^+ + M \tag{1.7}$$

1.2.5 Mixtures - Blanc's Law

Binary gas mixtures have been used in a number of technologies involving low temperature plasmas, such as plasma display panels, gaseous lasers, and plasma etching devices. Additionally, in gaseous detectors such as drift and wire chambers, gas electron multipliers (GEMs) and ionization and scintillation chambers, the use of gas mixtures is commonly adopted. Mixtures can be used to optimize radiation detection, in particular by adding molecular dopants to noble gases to improve the change on the electron drift velocities and minimize diffusion [17].

Blanc's empirical law, which resulted from Blanc's work in the mobility of ions in binary gaseous mixtures, has proven to be most useful when determining ions mobility using mixtures of gases. Blanc found that the mobility of ions in gaseous mixtures, K_0, obeyed a simple relationship as long as the charge transfer interaction is negligible compared to the polarization attraction and short-range repulsion between ions and atoms/molecules.

This relationship can be expressed as follows:

$$\frac{1}{K_{0mix}} = \frac{f_1}{K_{0g1}} + \frac{f_2}{K_{0g2}} \tag{1.8}$$

where $K_{0\,mix}$ is the reduced mobility of the ion in the binary mixture; $K_{0\,g1}$ and $K_{0\,g2}$ the reduced mobility of that same ion in an atmosphere of 100% of gas 1 and 2 respectively; f_1 and f_2 are the molar fraction of each gas in the binary mixture [18].

1.2.6 Collision Theory and Chemical Kinetics

The collision theory is built on the idea that reactant particles must collide for a reaction to occur. However, only in a portion of the total collisions, do ions have enough energy and the right orientation, at the moment of impact, to react and transform into products.

Considering a chemical reaction between two different species, A and B that originate species C and D:

$$aA + bB \rightarrow cC + dD \tag{1.9}$$

where a, b, c and d correspond to the stoichiometric coefficients, giving the molar quantity of each reactant and product involved in the reaction. This reaction is described by reaction rate R, which is directly proportional to the change in the concentration of a chemical species taking part in the reaction as a function of time. Increasing the concentration of the reactants or raising the temperature will originate more collisions and therefore many more effective collisions will occur, increasing reaction rate, defined as:

$$R = -\frac{1}{a}\frac{d[A]}{dt} = -\frac{1}{b}\frac{d[B]}{dt} = \frac{1}{c}\frac{d[C]}{dt} = -\frac{1}{d}\frac{d[D]}{dt} \tag{1.10}$$

where [A],[B],[C] and[D] are the concentrations of the species. The units of the reaction constant depends on the reaction type. The reaction rate can also be expressed as:

$$R = k[A]^m[B]^n \tag{1.11}$$

where k is named the rate constant, while m and n are the order of reaction of the reactants A and B. For an approximate calculation, the stoichiometric coefficients a and b can be used to determine the rate constant, despite of the true reactant order can only be determined experimentally.

In the case of a first-order reaction (A $\rightarrow$ products), the reaction rate has the following form:

$$R = k[A] = -\frac{d[A]}{dt} \tag{1.12}$$

Integrating the equation 1.12 in order of time, an expression for the concentration [A] can be obtained:

$$\int \frac{d[A]}{[A]} = -\int k dt \tag{1.13}$$

$$[A]_t = [A]_0.e^{-kt} \tag{1.14}$$

in which $[A]_t$ is the concentration of reactant A after a period of time t and $[A]_0$ is its initial concentration. Knowing the rate constant, k, for a particular reaction conditions and the initial concentration of reactant A, we can determinate the concentration [A] at any instant (t).

As it will be discussed in he following chapter, bimolecular and trimolecular reactions are more likely to occur in our experimental system. The respective reaction rates of second and third order for these chemical reactions are described as:

$$R = -k[A][B] = \frac{d[A]}{dt} \tag{1.15}$$

and

$$R = -k[A][B][C] = \frac{d[A]}{dt} \tag{1.16}$$

A similar deduction can be made for these reactions, however with an increase in the reaction order, the differential equation becomes much more complicated to solve and to track back the concentration of the different reactants. To solve this problem we can use the pseudo-first-order method as an approximation.

In the case of a bimolecular reaction, if [A]≫[B] we can assume that the concentration of A remains constant during the reaction, and equation 1.15 can be written as:

$$\frac{d[A]}{dt} = -k_{(2n)}[A][B] = -k_{(n)}[B] \tag{1.17}$$

in which

$$k_{(n)} = k_{(2n)}[A] \tag{1.18}$$

and the lower index n, 2n,..., corresponds to the reaction order.

For a third order reaction we have to assume that two of the chemical species involved remain constant throughout the reaction. In this example, it is considered that [A],[C]≫[B]

$$\frac{d[A]}{dt} = -k_{(3n)}[A][B][C] = -k_{(n)}[B] \tag{1.19}$$

in which

$$k_{(n)} = k_{(3n)}[A][C] \tag{1.20}$$

Elementary chemical reactions with higher orders than three are theoretically possible but have not been found to take place in nature, since the collision of more than three particles at once is highly improbable [4].

In chapter 3, we use the described method as an approximation to solve the differential equation and plot the concentration of ions versus the time of reaction, since in this case the availability of the gas molecules can in fact be considered constant when compared with the ions originated in the gas.

1.3 Our experiment

Between 2005 and 2009, Pedro N. B. Neves, as part of his doctoral program, developed a new experimental technique for measuring the mobilities of positive ions in their parent gases with a primary objective of distinguishing the atomic and dimer ions of rare gases. The method developed does not provide conditions for the positive identification of ions, but it allows measurements at higher working pressures than other experiments that use a mass spectrometer. This aspect is of great interest, for instance, for gaseous radiation detectors that typically work at atmospheric pressures [4].

In the scope of this work, he developed a prototype that makes use of a GEM (Gas Electron Multiplier) and a pulsed UV lamp to produce ions. The GEM was invented by F. Sauli and his first work about this subject was published in 1997 [19]. Originally this structure was developed for particle physics experiments, however, over the years this device has been used in a large number of applications. A recent attempt, made by the inventor, to summarize the progress of this structure can be found in [20]. The GEM consists on a thin Kapton foil coated with copper on both sides and perforated by a regular pattern of closely spaced holes.

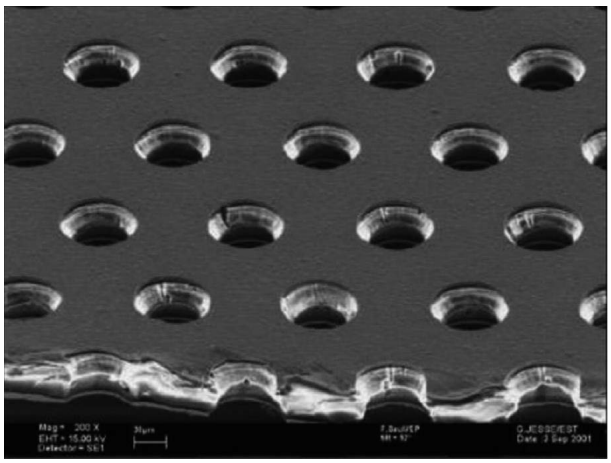

Figure 1.4: Electron microscope picture of a section of a typical GEM electrode, 50 μm thick. The holes pitch and diameter are 140 and 70 μm, respectively. Picture taken from [20].

In our work, a GEM was used for the ion production. In figure 1.4 it can be observed a picture of a GEM taken with an electron microscope.

A detailed description of the prototype can be found in chapter 2 of this report and a timeline of the ion mobility studies conducted by our group since the development of the detector can be found in figure 1.5.

Pure gases studies

The first experimental studies were carried out by P.N.B. Neves, who measured the mobility of monoatomic and diatomic ions in rare gases, like Argon (Ar) [4, 21, 22], Krypton (Kr) [22, 4] and Xenon (Xe)[4, 22]. In the Ar case, the measurements were made for pressures in the range of 6 to 30 Torr and values of reduced electric field (E/N) up to 60 Td. Regarding Kr, the measures were taken at pressures in 4–6 Torr range and electric field values up to 66 Td. The measures of K_0 for Xe were made at pressures in the range of 2-10 Torr and for values of E/N up to 86 Td. From here he concluded, as expected, that the Xe ions have the lowest mobility of these three gases. Also, the reaction rate constants for the 3 body collision reaction that results in the dimer's ion formation were measured by comparison of the peak's area of the time-of-arrival spectra obtained, for Ar, Kr and Xe [23]. For Ar, k_{Ar}=(1.2$^{+}_{-}$0.2)x10^{-31} cm^6 s^{-1}, for Kr, k_{Kr}=(2.1$^{+}_{-}$0.9)x10^{-31} cm^6 s^{-1} and for Xe k_{Xe}=(1.48$^{+}_{-}$0.18)x10^{-31} cm^6 s^{-1}.

In the continuity of this line of work (rare gases), in 2011 was performed a mobility study for Neon [24]. According to the authors, they were able to get the mobility values for the dimer and atomic ions of Neon, which an extrapolation to a reduced zero electric field produces mobility values in agreement with other published data.

In 2012, A.N.C. Garcia conducted a study on the N_4^+ ion mobility in molecular nitrogen (N_2)[25], which is known to have good properties as a buffer. This study led to a mobility of 2.37 $cm^2V^{-1}s^{-1}$, when $E/N \rightarrow 0$ Td, which was in good agreement with the literature, according to the author. This work is also summarily described in this report in section 3.3, and compared to additional data taken for N_2 with higher voltages across the GEM.

In the same year, A. M. F. Trindade published the results of the measurements of positive ions mobility of methane (CH_4) in methane [26]. This gas is often used as quencher in gas-filled detectors hence the importance of studying its properties. He reported the presence of two peaks for pressures in the range from 3 to 10 Torr and for E/N between 10 to 60 Td. The peaks were identified as CH_5^+ ions in the case of the 1^{st} peak and as $C_2H_5^+$ and $C_3H_7^+$ ions for the 2^{nd} peak.

For similar pressures and reduced electric fields, A.F.V Cortez made in 2013 an

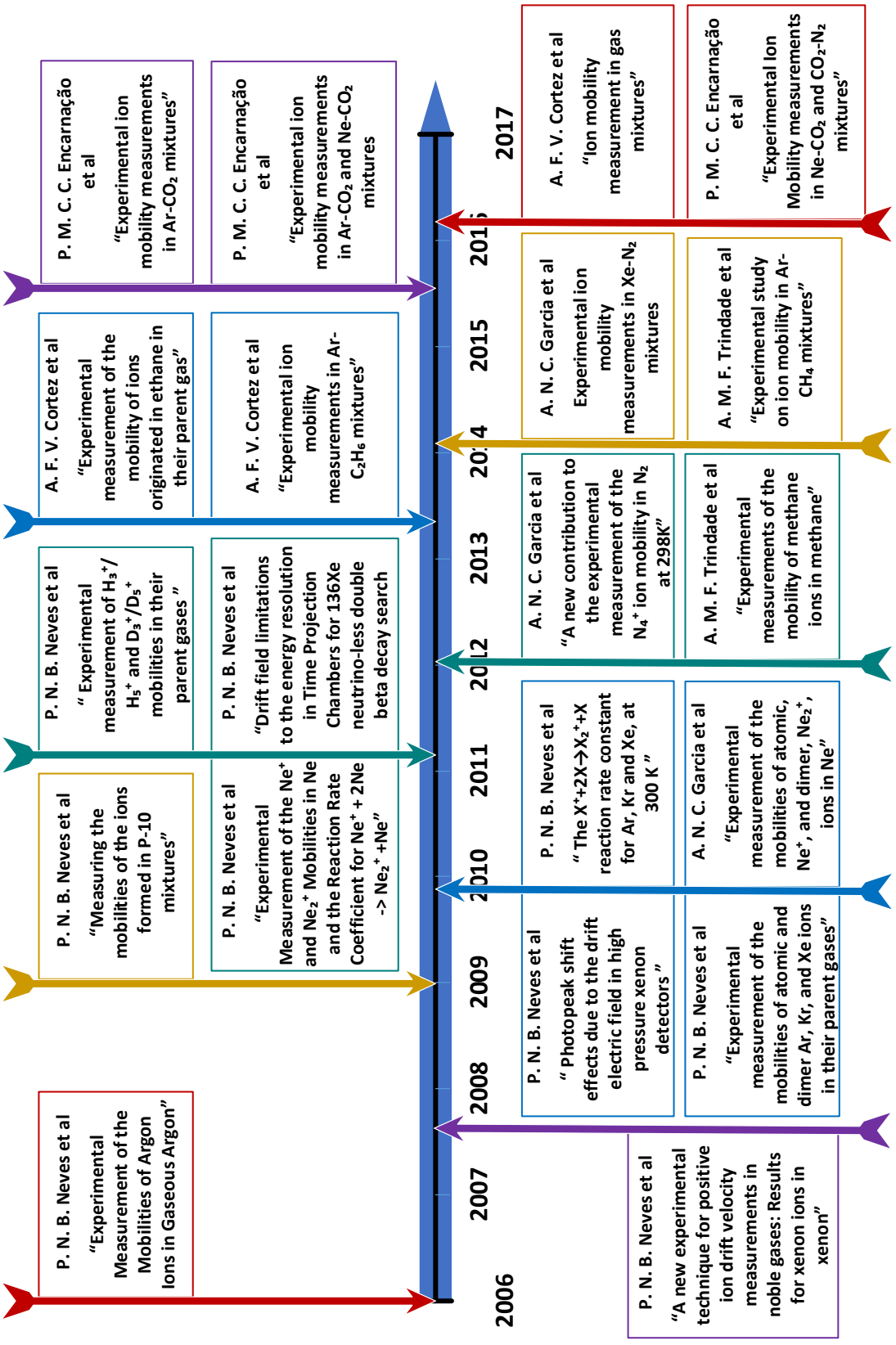

Figure 1.5: Timeline regarding the scientific and conference papers published with the results obtained in the experimental system developed by P. N. B. Neves at LIP-Coimbra.

analogous mobility study for ethane [27]. Similarly to methane, the time of arrival spectra revealed two peaks which probably belong to a 3-carbon ions group, which includes $C_3H_5^+$, $C_3H_7^+$, $C_3H_8^+$ and $C_3H_9^+$, and to a 4-carbon ions group which includes $C_4H_9^+$ and $C_4H_{10}^+$ ions, respectively.

Mixtures studies

Since the development of the experimental setup, eight different studies of ion mobility in mixtures were performed. A small compilation of the results obtained for a reduced electric field (E/N) of 15 Td, at room temperature and pressures typically in a range of 6 to 12 Torr can be found in chapter 4.

The first study of ion mobility in mixtures using this system was carried out by A.F.V Cortez *etal.*, in 2013. The mobility of ions in argon-ethane gaseous mixtures (Ar-C_2H_6) was studied for pressures ranging from 6 to 10 Torr and for reduced electric fields in the 10 Td to 25 Td range, at room temperature. The experimental results obtained by the authors can be found in [28]. The authors found that for Ar concentrations below 80% only two peaks were observed in the time of arrival spectra, which were attributed to ion species with 3-carbons ($C_3H_7{}^+$, $C_3H_8{}^+$ and $C_3H_9{}^+$) and with 4-carbons (which includes $C_4H_7{}^+$, $C_4H_9{}^+$, $C_4H_{10}{}^+$ and $C_4H_{12}{}^+$ions). A third peak appears for Ar concentrations above 80% which the author attributes to the $C_5H_{11}{}^+$ ion.

In 2014 two papers were published presenting the results of the ion mobility measurements made in gaseous mixtures of argon (Ar) and methane (CH_4) [29] and for gas mixtures of xenon (Xe) with nitrogen (N_2)[30]. In the first A. M. F. Trindade performed measurements for a pressure range from 5 to 8 Torr and for low reduced electric fields (in the 17 Td to 43 Td range). The time of arrival spectra obtained for the several mixture ratios studied revealed that the relative abundance of the ions formed depend on the mixture ratios. For CH_4 concentrations in the 2.5–10% range three well defined peaks were observed, which were attributed to single-carbon ions (CH_5^+), 2-carbon ions ($C_2H_4^+$ and $C_2H_5^+$), and 3-carbon ions ($C_3H_4^+$, $C_3H_5^+$, $C_3H_6^+$ and $C_3H_7^+$). The time of arrival spectra for CH_4 concentrations of 2.5%, 5%, 10% and the reduced mobilities of the ions obtained from the peaks observed are presented in this paper. The measurements in the second paper were conducted by A. N. C. Garcia. For 0–100% range of Xe concentrations in the mixture, only one peak was observed, which was attributed to Xe_2^+. The mobility results obtained by the authors obeyed Blanc's law prediction.

Concerning the work developed in the scope of the work presented here, the following gases and gas mixtures were studied:

- **CO_2**
- **N_2**
- **Mixtures of Ar-CO_2**
- **Mixtures of Ne-CO_2**
- **Mixtures of CO_2-N_2**
- **Mixtures of Ne-CO_2-N_2**
- **Mixtures of Ne-N_2**
- **Trimethylamine (TMA)**
- **Mixtures of Xe-TMA**

The results and analysis of these measurements are present in chapter 3 and in appendix B of this report. The results of pure and carbon dioxide mixtures, have already been published in JINST [31, 32].

Chapter 2

Experimental setup and Methodology

In this section we describe the experimental system and methods used to conduct the studies of positive ion mobility in gas mixtures. This experimental system and related methods of analysis have proven to be a valid solution for the ion identification problem, as can be seen through several scientific contributions described in section 1.3.

In section 2.1 the working principle of the detector is described, with reference to the physical processes that lead to the production and detection of ions and how their reduced mobilities are determined. The detector structure and the electronic system associated with it are described in 2.2, and it is based on the last of three prototypes developed by P.N.B. Neves between 2005 and 2009.

The vacuum and gas admittance system, filling process and the gases used in the experiment are detailed in 2.3. In section 2.4 it is described the GEM conditions and the methods used to clean the detector and the deposition of a new CsI layer. In section 2.5 is shown a new, more practical and automatic program of analysis that was developed in the form of a standalone application, and in section 2.6 is illustrated how the ion identification process is performed. The limitations of the experimental measurements are explained in section 2.7.

Figure 2.1 shows a photo of our experimental apparatus. It is possible to observe the detector and pre-amplifier designed for the detection of positive ions and amplification of the signal generated, and the pressure gauges used either to control the pressure of mixture within the system or to verify whether there is a suitable vacuum level to perform the measurements. It can also be seen the digital oscilloscope responsible for the recording of the detector signals.

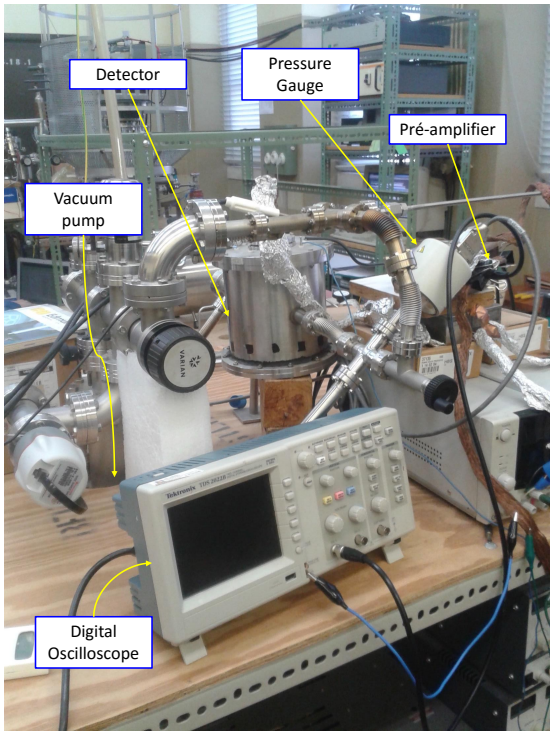

Figure 2.1: Experimental Apparatus.

2.1 Operation Principle

The experimental system, schematically shown in figure 2.2, is initiated by the flash of the Hamamatsu Xenon Flash UV lamp (model L2439) that emits photons with a frequency of 10 Hz with a pulse duration shorter than 0.5 μs. These photons impinge on the CsI photocathode deposited on the top of electrode of the GEM and release photoelectrons.

The GEM is polarised so that these photoelectrons are conducted through the holes to the bottom GEM electrode and in their way, they gain energy from the electric field and ionize the gas atoms and molecules when the electrons' energies are higher than the gas ionisation threshold. The electrons start multiplying in avalanche, increasing exponentially along the holes[4], since the energy gained by the ions through their path is roughly equivalent to the voltage difference between top and bottom of the GEM, by controlling the voltage difference between the electrodes, we can control the maximum energy that the electrons can gain, limiting this way the type of ions formed - this feature is one of the most import aspects of our ion identification process, as it will be discussed in section 2.6.

The electrons avalanche migrates to the bottom electrode of the GEM, where the electrons are collected, while the cations that result from the ionization of the gas

molecules in the GEM holes flow in the opposite direction, drifting towards grids G1 and G2 under an uniform electric field. Grid G2 acts as a Frisch grid, avoiding signal induction by the group of ions in the collecting grid G1 during their drift between the GEM and G2. So the output signal in G1, will correspond only to the portion of the positive ion's motion that takes place between G2 and G1 [33].

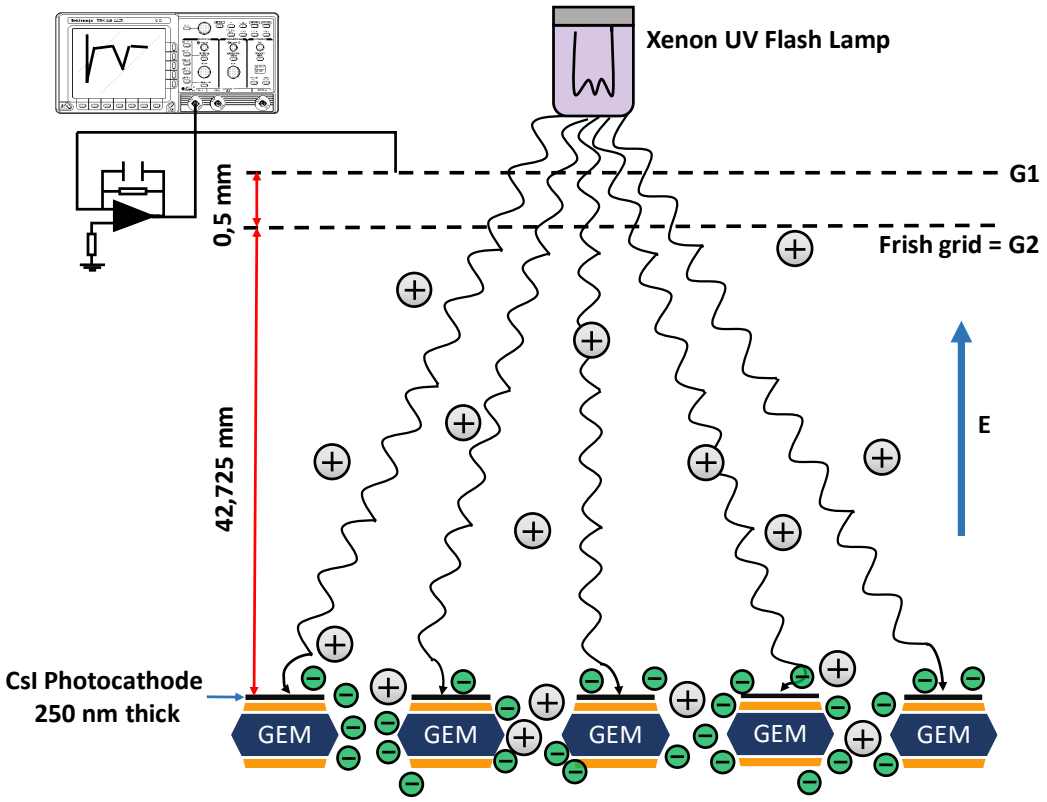

Figure 2.2: Shematic representation of the physical processes that lead to the production and detection of ions For more details see [4].

Ideally the ions should cross the gap between the grids G1 and G2 as quickly as possible, but the electric field between these two grids cannot be too high otherwise it could disrupt the uniformity of the drift electric field [34].

A pre-amplifier is used to convert the electronic pulse collected in G1 from current to voltage, after which the time spectrum is recorded in a digital oscilloscope (Tektronix TDS 1012). To filter the instabilities in these measurements, an average of 128 spectra are recorded This data is then processed by a specially developed application.

A standalone application named Azarus, (section 2.5) was developed in Matlab® to provide accurate Gaussian fittings to the obtained time-of-arrival spectra. The calculation of both drift velocity and mobility is achieved using the centroid of the Gaussian fit, since it corresponds to the ions' drift time along the known distance from the GEM

to grid G2.

The maximum error introduced in the mobility value is yield by the ratio of the two distances (drift distance and distance between the grids), although this value is usual substantially low, due to the electric field applied between the two grids. For example, in the case of Ne^+ in pure Ne, for a reduced electric field of 10 Td, the mobility of the group of ions is 4.32 ± 0.02 $cm^2V^{-1}s^{-1}$, which corresponds to a drift time between the GEM and the grids equal to 300 μs. Assuming that the mobility of these ions remains between the two G1 and G2 grids (which is not correct because the field is actually much more intense), the ion group will cross the grids in just 0.2 μs, which corresponds to 0.07% of the total time drift. Even if there is a difference in reduced mobility value due to the different E/N in the drift and gap regions, this will not affect the mobility measured significantly.

2.2 Detector

Some pictures of the inside of the detector are shown in figure 2.3. The prototype was also designed in SolidWorks® for posterior modifications (see section 5.2.1) and is depicted schematically in figure 2.4. Figure (2.3(a)), is a photograph of the body of the detector without the upper flange, in which is assembled the functional part and where we can observe the gas inlets of the detector and also one of the O-rings that is placed between the detector's body and the flanges, guaranteeing system isolation.

As it can be observed in picture 2.3(b), the GEM is assembled in the last disk of stainless steel. It is possible to observe two schematics views of its geometry in figure 2.5. Because of the etching process, the holes are not cylindrical but conical, being narrower in the middle. The GEM's thickness is 60 μm, with 50μm of Kapton and a 5 μm copper layer on each side. The GEM has an active area of 10x10 mm^2 and was assembled on a G-10 (glass fibre material). Regarding the holes, they have a wider diameter of 70 μm at the metal surface and a inner diameter of 55 μm in the insulating layer. They have an hexagonal spatial arrangement wherein the center of each hole is distanced 140 μm from the others, as seen in figure2.5(a). The GEM geometry is one of the reasons to use it as an ion source, because it allows us to know the initial position of the ions and consequently the drift time with great accuracy, since its thickness is a very small when compared to the drift distance (of the order of a few cm).

The electric field that is applied between the two electrodes of the GEM, allowing the ionization of the gas molecules is accomplish using two high power DC supplies, Fluke 415B and HP 6110A. The first is connected to the top electrode of the GEM and

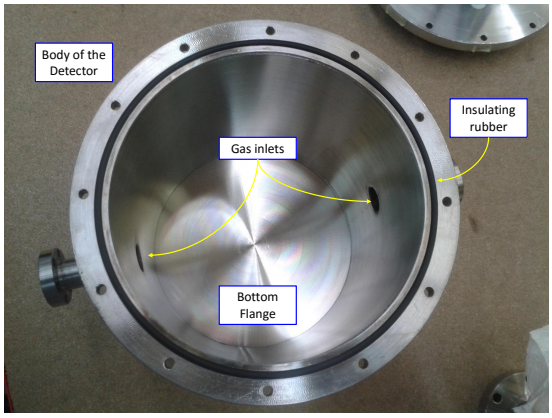

((a)) Interior of body's detector

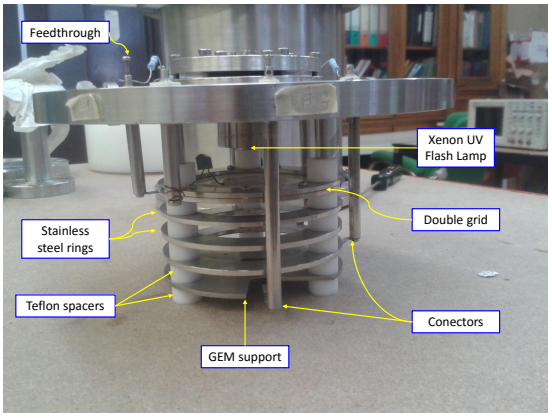

((b)) Interior profile (from top to bottom)

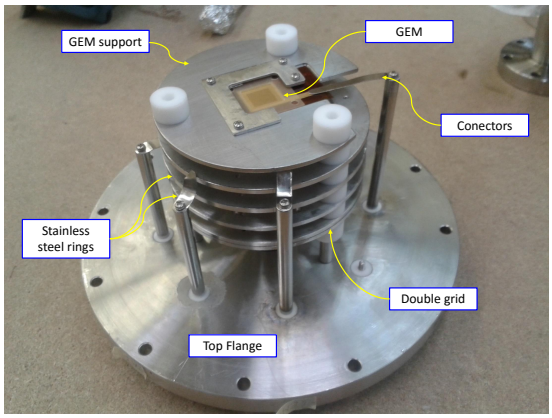

((c)) Interior profile (from bottom to top)

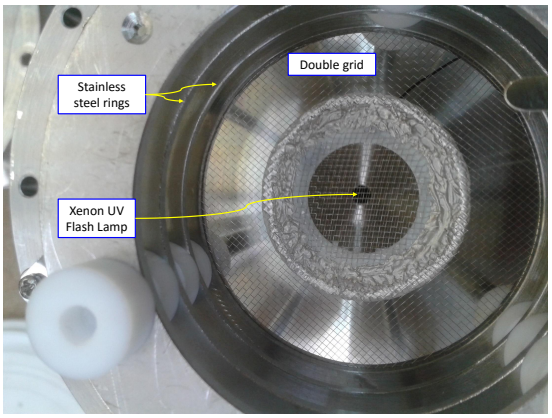

((d)) Double grid

Figure 2.3: Components of the ion mobility detector.

it is also used to establish the electric field in the drift region of the chamber and the second to the bottom electrode. The voltage difference between the two electrodes limits the maximum energy gained by the electrons.

The electric field intensity in the drift chamber, E, is given by the ratio of the potential difference between the top electrode of the GEM and grid G1 and the drift distance.

The uniformity of the electric field in the drift region was accomplished by setting several 2 mm thick stainless steel rings equally spaced using Teflon spacers. A correct voltage was set to the rings by a chain of resistors of 2.76 MΩ.

A 250 nm thick layer of high purity CsI was vacuum deposited on the top surface of the GEM to operate as the photocathode and initiate the process of ion production, as explained in section 2.1. The thickness of this layer was later changed to 320 nm after cleaning the detector, as will be explained in detail in section 2.4.

In the last sub-figure 2.3(d) it is possible to observe the component responsible for the detection of the group of ions, which consists of two closely spaced meshes, desig-

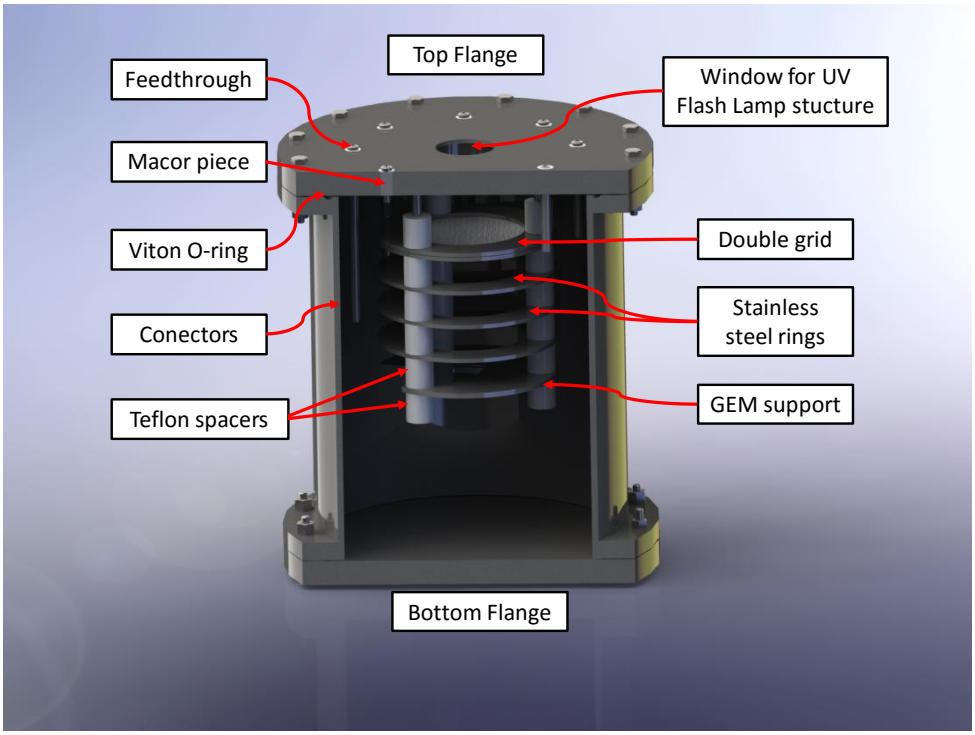

Figure 2.4: Schematic representation of the detector designed in SolidWorks ®.

nated by G1 and G2, separated by a $0.5^{+}_{-}0.1$ mm thick MACOR spacer. The grids are made of stainless steel wire, 80 μm in diameter and 900 μm spacing. The voltage difference between G1 and G2 was set on 30 V by a precision DC power supply Thandar TS2022S. This value was select so that the ions were able to cross G2 and be collected in G1, rapidly. The drift distance, d, between the GEM and the double grid was set to $42.73^{+}_{-}0.2$ mm and measured with a cathetometer. The window of the Hamamatsu Xenon UV Flash Lamp (model L2439) can also be observed. This lamp was fed by a DC power supply Topward 6303D, and operated at a repetition rate of 10 Hz, with the pulse width (FWHM) is inferior to 500 ns.

Regarding the signal retrieved at G1, a voltage pre-amplifier is used to amplify the pulses and is connected to an oscilloscope. An image of the pre-amplifier is shown and depicted schematically in figure 2.6. This component is a high density charge sensitive pre-amplifier, model A250F/NF, designed by AmpTEK ®. The resistors were chosen to maximize the gain on one hand, and minimize the noise on the other [4]. A decoupling capacitor was used between ground and the output channel to reduce the induction effect by circuit elements in the signal. Also, the pre-amplifier was shielded with a copper box with 1 mm thickness to avoid electrical noise from external sources.

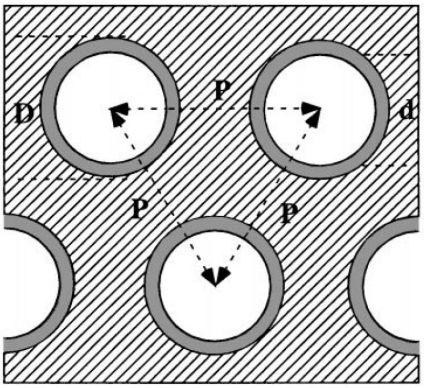

((a)) Upper view of a standard GEM

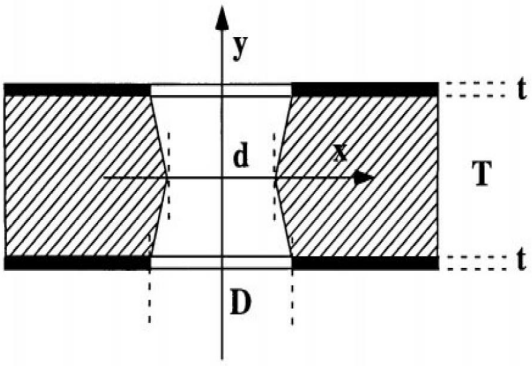

((b)) Section view of a hole of the GEM

Figure 2.5: Geometry of a standard GEM. P = 140 μm, D = 70 μm, d = 55 μm, T = 50 μm, t = 5 μm [35].

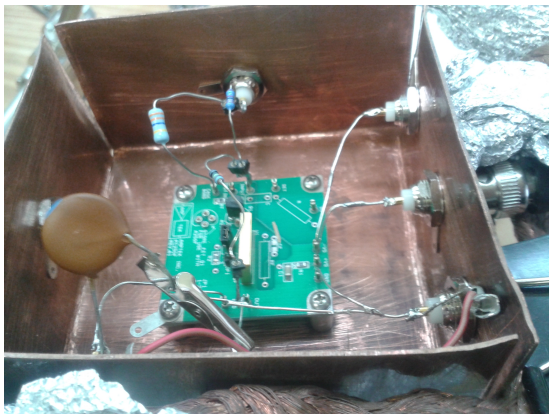

((a)) Picture of our pre-amplifier

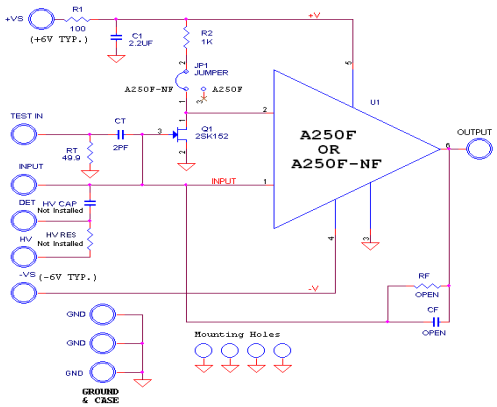

((b)) Schematic of voltage pre-amplifier

Figure 2.6: Voltage pre-amplifier used to amplify the ions pulses.

2.3 Vacuum and Gas admittance System

Regarding the vacuum system used, shown schematically in figure 2.7, it includes an evacuation system and a region of gas admission. Vacuum is performed by an Edwards EXPT Pumping Station, a fully automatic pumping system composed by a backing pump that performs medium-level vacuum (to a maximum vacuum level of 1.5 Torr) and a turbomolecular pump which can evacuate our experimental system up to $1x10^{-7}$ Torr.

To perform vacuum throughout the whole system, valves V1, V3, V4 and V5, must be open. In order to evaluate the vacuum quality in the system, we use an Edwards WRG-5-NW35, designated P1 in the scheme, that is a gauge combination that uses Pirani technology for the upper pressure range, with a uniform switch that changes to an

inverted magnetron for the lower pressures offering the capability of single port pressure measurement in the range from atmosphere to 10^{-9} mbar with a linear output, which makes its use suitable for our experimental conditions [36].

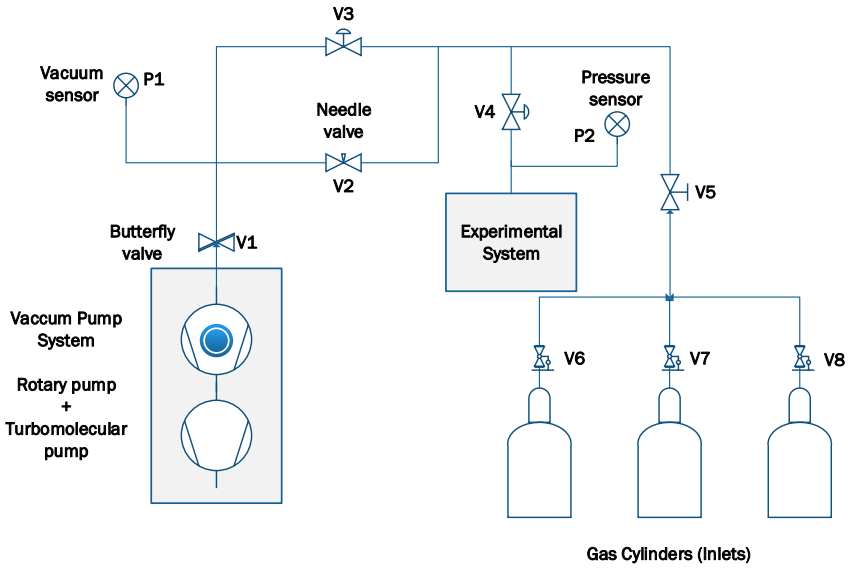

Figure 2.7: Schematic of the vacuum system used to evacuate the experimental set-up. P1 is the pressure sensor used to measure the pressure of the vacuum system during the evacuation. P2 is the pressure sensor used to measure the pressure of gas inside the experimental system. Vi, i=1,2,...8 are to the valves used in the vacuum system.

The most important valves are V1 (butterfly valve) and V4 valves. The first one (V1) allows direct isolation of the vacuum line from atmospheric pressure when the vacuum pump system is turned off, since there is air admittance in the vacuum pump when its shut down. V4 allows the isolation of the experimental system for maintenance purposes in the remaining vacuum line or when a leak is detected. The valve V5 function is to isolate the region of gas admission from the rest of the system as support for valves V6 to V8, when one or more gas cylinder containers have to be changed.

Concerning the admission of gas in the experimental system, we have three inlets which allow installing three gas cylinders to produce the desired mixtures. To introduce correctly the right amounts of each gas, we use a dual-stage high-purity gas pressure regulators (V6, V7 and V8), where the gas pressures introduced are verified by digital display Edwards 1575 MON ANALOG connected to a membrane pressure gauge Edwards Barocel Pressure Sensor 600AB Trans 1000TR [37] (labelled P2). To fill the detector with gas from the vessels, V3 and V2 valves stayed closed.

The filling procedure of the detector is a simple but very sensitive method. Even with a lot of practice, it is quite easy to miss the amount of gas, by excess, that is intended to fill the detector. Eventually we can perform corrections of internal pressure creating a small "leak" through V3 or V2 valves (V2 is a needle valve, ideal for a small adjustment). However, these corrections cannot always be done since when working with mixtures, the filling up must be done with one type of gas at each time. It is not possible to adjust the ratio of each gas after the filling is complete. That means that after the second gas is allowed in it is not possible to remove any gas or re-introduce more gas from the first type without compromising the mixture true ratio.

2.3.1 Filling Process

The reduction of the error in the composition of the desired mixture is achieved through the order at which each gas of the mixture is introduced in the detector since the pressure gauge (P1) used has a reading accuracy of 0.15% [37].

Since the error is directly proportional to the pressure, gas that will have a lower relative amount in the mixture should be inserted first. The following example is given to better clarify this situation: Consider a mixture of Ar-CO_2 with relative amounts of 99% - 1%, respectively, at an absolute pressure of 10 Torr. So, we have 9.9 Torr of Ar and 0.1 Torr of CO_2 to insert in the chamber. Consider that Ar is the first gas introduced in the detector and for that reason will have an uncertainty of ± 0.015 Torr. In second place, we will introduce 0.1 Torr of CO_2, but the uncertainty of the measurement is 0.15% of 10 Torr (Ar plus CO_2 pressures) which gives ± 0.015 Torr. This corresponds to a relative error of 15% of the CO_2 quantity inserted and the mixture has a total uncertainty of ± 0.03 Torr. On the other hand, if we introduce the CO_2 quantity first, the total uncertainty of the filling process for the mixture will be ± 0.015 Torr and ± 0.00015 Torr for CO_2, a half and a hundredth of the error obtained by the other method, respectively.

Another aspect to take into account is the error introduced in the filling process by human mistakes, due to the sensitivity of the valves. According to our experimental standards, we discard fillings with absolute variations greater than 0.008 Torr.

2.3.2 Gases used

The present study was carried out using different high purity gases for research purposes, with exception of TMA which only has a purity level of 99% due to manufacturer limitations. Table 2.1, displays some properties of the gases used according to

the manufacturer. This is important since the experimental system does not have gas purification included.

Table 2.1: Purity level of the gases used to conduct the studies of ion mobility. Detailed information by the manufacturer can be found in [38–43], respectively for the Ar, N_2, Ne, Xe, CO_2, TMA gases.

Gas	**Ar and N_2**	**Xe**	**Ne**	**CO_2**	**TMA**
Purity %	≥ 99.9999%	≥ 99.999%	≥ 99.999%	≥99.998%	≥99%
Impurities (ppm/V)	O_2 (≤0,5) H_2O (≤0,5) C_nH_m (≤0,1) CO (≤0,1) CO_2 (≤0,1)	Ar(≤1) CO_2 (≤1) CF_4 (≤0,5) H_2 (≤2) Kr (≤5) N_2(≤2) O_2(≤0,5) THC(≤0,5) H_2O(≤0,5)	CO_2 (≤0,5) CO (≤0,5) He (≤8) CH_4 (≤0,5) N_2 (≤1) O_2 (≤0,5) H_2O (≤0,5)	O_2 (≤2) H_2O(≤3) N_2(≤10) THC(≤4) CO (≤0,5)	Not specified

2.4 CsI deposition in the GEM due to the photocathode aging

During our experiments with the chamber, the signal amplitude began to decrease over time and electric discharges occurred for lower electric fields than previously. We concluded that these phenomena were related to the aging of the photocathode. There are several known phenomena responsible for the deterioration of the photoemission features of CsI like exposure to air and water molecules, the impact of photons, ions bombardment, contamination by impurities or the action of charged particles [44]. In our experimental conditions, the aging due to photon flux must be the main reason as will be further discussed.

The UV flash lamp used to initiate our experimental procedure, as mentioned in section 2.1, where the operating principle is described, can have a negative effect on the CsI. When the photocathode experiences an intense photon flux, its ageing is accelerated due to a photolysis process, leading to its metallization. It is believed that the dissociation of CsI molecules is described by [45, 46]:

$$h\nu + \mathrm{CsI} \rightarrow \mathrm{Cs}^{+} + \mathrm{I} + \mathrm{e}^{-} \tag{2.1}$$

This dissociation causes the evaporation of iodine atoms, resulting in an excess of cesium in the subtract, which can originate a reduction of quantum efficiency (QE) of CsI, resulting in a loss of signal because less charge is created.

The metallization process could also explain why we had experience discharges with lower electric fields. Even though the CsI resistivity may not be a stable quantity and may be influenced by various experimental conditions, for similar air exposures to ours (measured in good vacuum conditions a few hours later after 10 minute exposure to air), the authors reported a resistivity of $6\text{x}10^{13}$ Ω m [47]. The CsI has a good ohmic behaviour but if the dissociation in equation 2.1 occurs, the iodide evaporates and we have a conductive material near the GEM holes, originating pathways for possible discharges, since the resistivity of cesium is considerably lower than CsI, $20.46\text{x}10^{-8}$ Ω m at room temperature (20 ºC)[48].

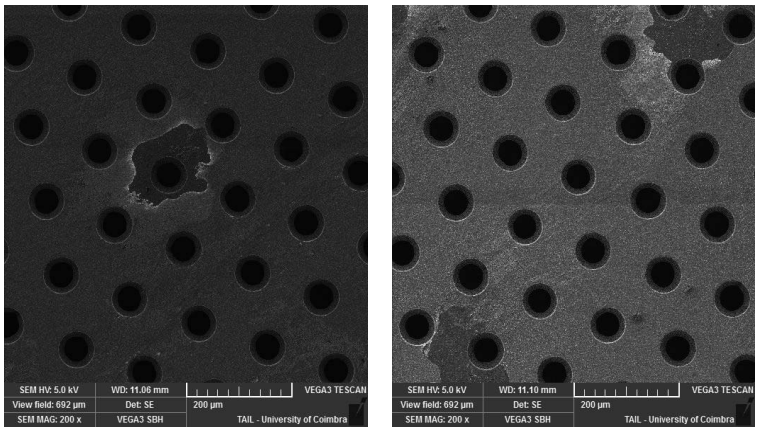

Figure 2.8: Deterioration of the photocathode on top of the GEM viewed by SEM at a magnification of 200x.

Regarding exposure to humidity, the reactions with CsI are well know and many studies can be found in literature [44, and references therein]. The decay of the photoemission features of CsI are caused by hydrolysis of the material surface. However, since it was evaporated on the GEM and assembled inside the chamber, the CsI photocathode did not suffer significant exposures and no leaks were found in the system that could explain such a significant abrasion. Yet, we believe that the visible deterioration in figure 2.8, may have been produced when mobility studies were performed with trimethylamine (TMA) that in contrast with the other gases used, has about 1% impurities, mainly water.

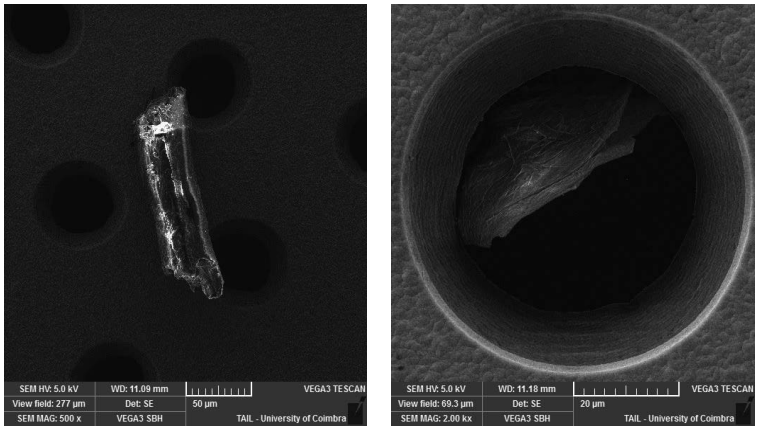

Figure 2.9: Impurities found in both sides of the GEM viewed by SEM at magnification of 500x and 2000x, respectively.

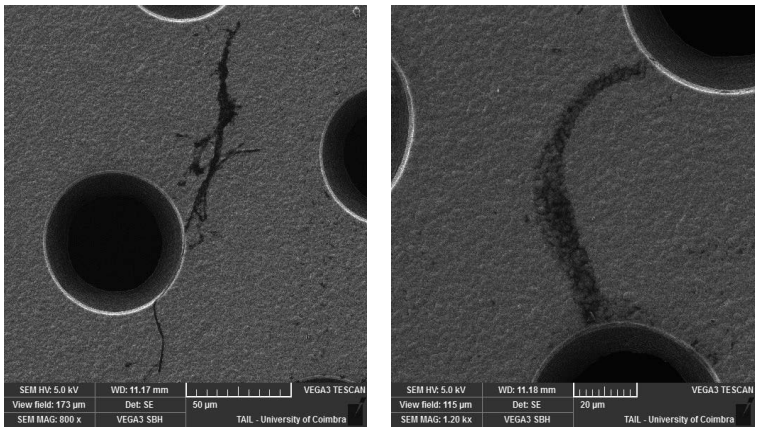

Figure 2.10: Two different discharge pathways on the bottom layer of the GEM viewed by SEM at magnification of 800x and 1200x, respectively.

Another effect that may originate photocathode aging are the collisions between the ions/charges and the photocathode, whose consequences are similar to those caused by photon flux action [44]. Nevertheless, since the electric field applied prevents these collisions, we do not expected this to be the main cause of the photocathode degradations.

In order to evaluate the superficial conditions of the GEM, it was used a Scanning Electron Microscope (SEM) TESCAN Vega3 SBH, capable of providing images with amplifications between 4.5 - 1.000.000x. A scanning across the active area of the GEM was made, on both sides. Some examples of the images taken, showing the photocathode aging, impurities and discharge traces in our GEM are presented in figures 2.8, 2.9 and 2.10, respectively.

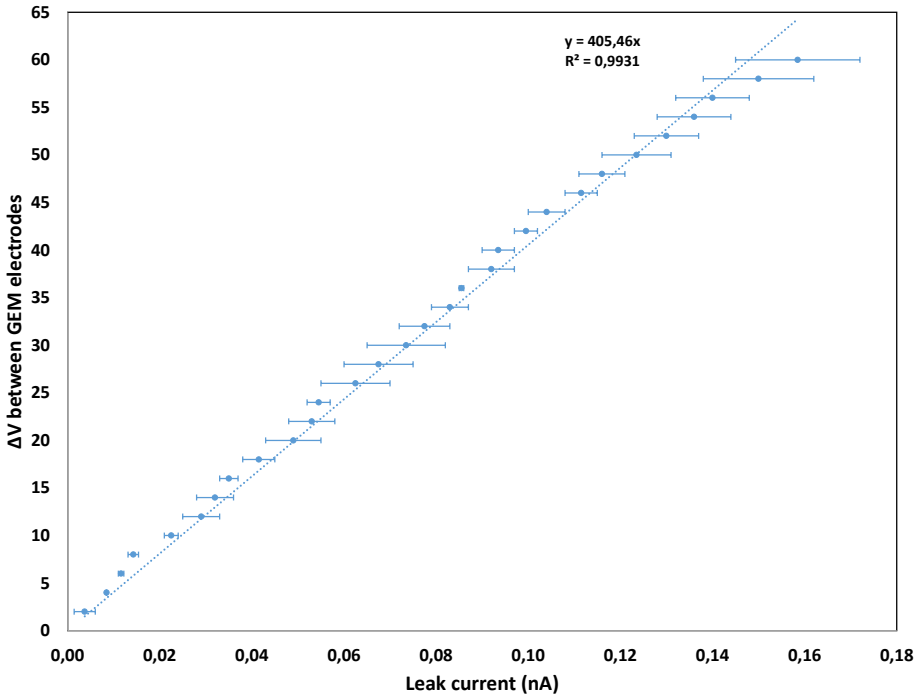

Figure 2.11: Voltage applied between GEM electrodes versus the leak current of the GEM, in nA, measured with a electrometer Keithley 6512.

To remove the CsI deposit and impurities, the GEM was cleaned up, in a clean chamber, with deionized water and placed to dry in the oven for 24 h. After this, the electric properties of the GEM were tested. The procedure consists in measuring the leakage current, through a electrometer Keithley 6512, by slowly increasing voltage difference between the GEM electrodes, from 0-60V in 2V steps. The results are plotted in figure 2.11 and a linear fit to the data was performed, where the slope represents the resistance between GEM electrodes. As specified in [49], the standard acceptance criterion demands less than 5 nA leakage current at 500 V between the electrodes, meaning that a GEM is in good electric conditions if the resistance is higher than 100 GΩ. As it can be confirmed by the graphic, we obtained a value of 405 GΩ, which allowed us to expect a proper operation of the GEM.

The chamber was dismantled at the beginning of the ion mobility study of the Ne-N_2 mixture, when the signal amplitude became too small to allow proper measurements. As described in section 2.4, the GEM was in good electrical conditions, so we used the same one when reassembling the detector.

A new layer of CsI was deposited in the top electrode of the GEM using the evaporation plant shown in figure 2.12(a). The CsI was placed in a metal strip (2.12(b)), which, when crossed by a current, heats by Joule effect, causing evaporation of CsI substrate.

((a)) General set-up ((b)) Metal strip to evaporate the CsI

Figure 2.12: Evaporation plant used make the deposition of CsI in the GEM.

By controlling the current, we can control the evaporation rate of the subtract, ensuring ideal conditions of deposition. According to [44], to ensure that the best possible QE of CsI is obtained, the evaporation is done in vacuum conditions varying between 10^{-5} and 10^{-8} Torr with a rate of the order of 1 to 10 nm/s, in general. We carried out the deposition with a rate of 1.1 nm/s when an ultimate pressure in the system of $5x10^{-6}$ Torr was achieved, conditions that are close to the ones described.The CsI film thickness was increased to 320 nm,.

The GEM was mounted in the chamber and vacuum was made to it in order to avoid ageing of the photocathode, in less than 5 minutes. After this procedure an improvement of signal-to-noise ratio was achieved and also the discharges no longer occurred as previously.

2.5 Data Analysis - Azarus Standalone application

One important aspect of this work is the data analysis and the method used in previous works took a lot of time to analyse the data obtained. In this method it was necessary to:

- Convert the data to a compatible file extension;
- Import the files of the reading folder individually;
- Choose the start conditions of the fit (iteratively until obtaining a suitable fit);
- Save the figures of each file manually and copy the files to a previously formatted Excel sheet;

- Graphically determine the UV lamp offset and correct the mobility value;

If some of these aspects were performed automatically and in a more user-friendly way, the data analysis could be made much quicker. With this purpose it has been developed for Windows based operating systems a Standalone application named Azarus. It was developed with MATLAB ®code, version 2016a. Also, it was compiled with the deploy toolbox in a standalone application so it can work in any PC, even without the Matlab products installed.

This program's interface is shown in figure 2.13, and it is capable, through a list of files, of automatically reading and improving the signals obtained directly through the oscilloscope, and also generating suitable Gaussian fits to the signal and recording the figures obtained in different formats (like .pdf and .png extensions) as well as providing the information generated from adjustments or other important data (.csv and .xlsx extensions).

We will now describe the features of the developed application using the letters shown in figure 2.13.

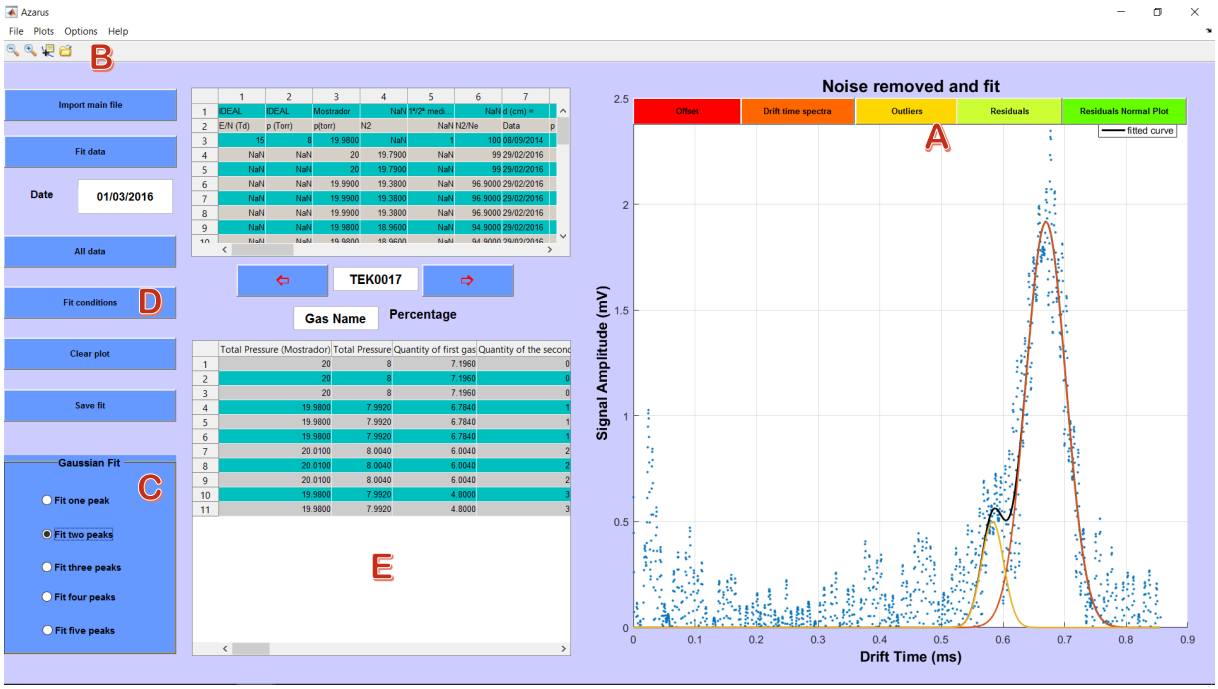

Figure 2.13: Capture of Azarus application.

A-Plots

Letter A is located in the position where the different plots provided by the program can be accessed. As it can be seen in figure 2.13 the Azarus application offers 5 types of plots, and it is possible to alternate between them by clicking on the five buttons in the top right corner of the interface.

The first plot, shown in figure 2.14, displays the spectrum obtained in the experiment after the background noise is subtracted and the signal is de-noised. It also displays the data fit made by the program. A more detailed explanation about signal's de-noising and fit methodology is made in sections 2.5.1 and 2.5.2, respectively.

The other four plots that are generated by Azarus are shown in figure 2.15 and they represent the signal induced by the UV flash lamp (figure 2.15(a)), the outliers excluded by the program (figure 2.15(b)), improving the fit quality, and the distribution of residuals, which has to be approximately Gaussian. Figures 2.15(c) and 2.15(d), allow us to evaluate if any important data was not consider by the fitting procedure (see section 2.5.2.1).

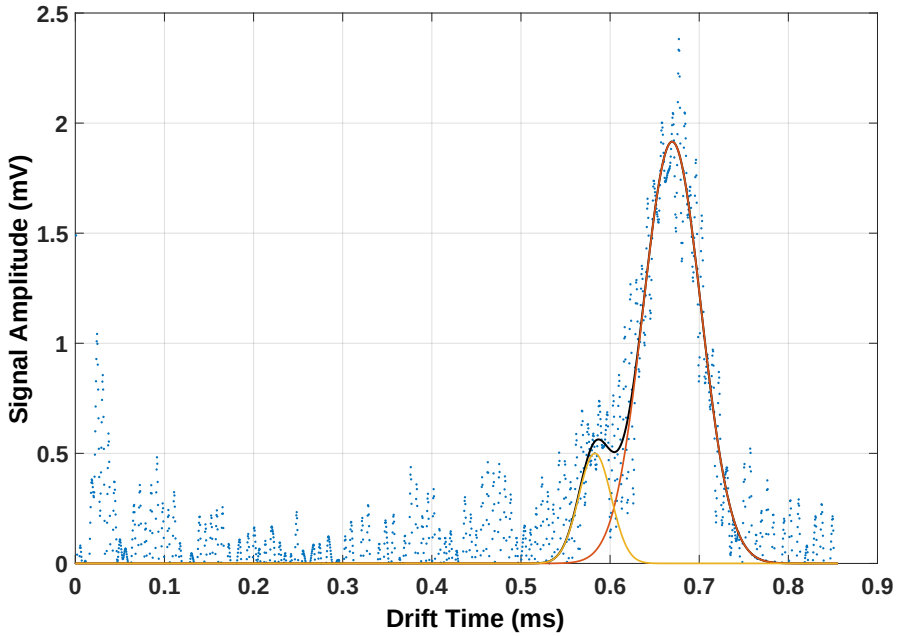

Figure 2.14: Time-of-arrival spectrum averaged over 128 pulses for pure N_2 at a pressure of 8 Torr, temperature of 298K and for a reduced electric field of 10 Td with a voltage across GEM of 30 V. The figure was generated by Azarus, where the background noise has already been subtracted, the signal de-noised and the fitting to the data performed

Regarding the offset in the trigger caused by the lamp, it typically adds time to the ion drift time and if this value is not subtracted, the mobility value will present an error in the third decimal place. For this reason, the algorithm implemented to calculate this value, automatically, but if for any reason the user believes that the offset is not well calculated, the tools presented in Menu (location B) can be used to determinate the offset value using the plot of lamp' signal.

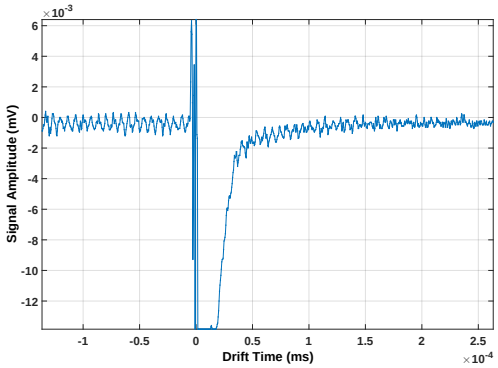

((a)) Signal induced by UV lamp

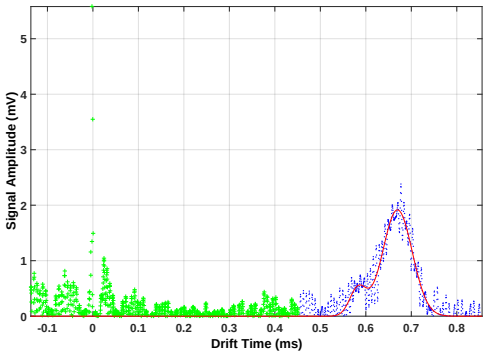

((b)) Outliers removed by the program

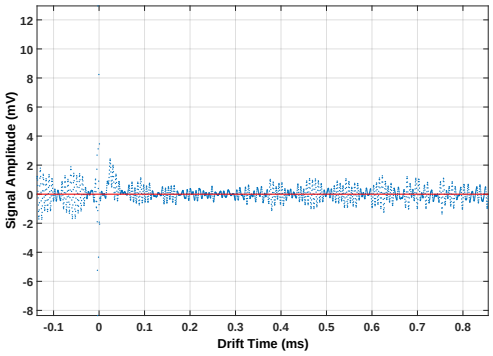

((c)) Residuals of the fitting

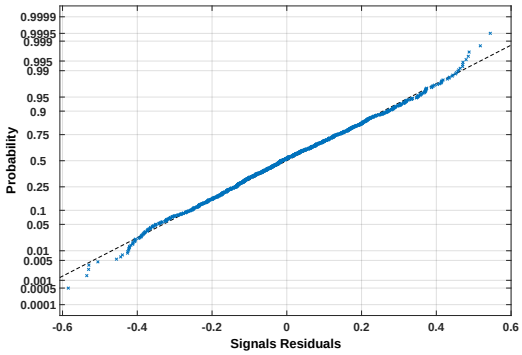

((d)) Probability plot(normal distribution)

Figure 2.15: Azarus analysis.

B-Menu

The location B corresponds to the menu bar. Here the user can find many functions as importing data, saving figures and exporting data to excel, zooming the plots and retrieving information from the plots and other minor functions.

C-Fit and D-Start Conditions

The interface buttons labelled by C and D relate to the type of Gaussian fit and its initial conditions . The user can set which fit is best for the data, by choosing a fit with 1 to 5 Gaussians, clicking in one of the five radio buttons shown. Furthermore and although the program makes adjustments automatically, if the result is not acceptable, the start point of the fit (amplitude, mean and standard deviation of each Gaussian) can be set by the user so that the fitting can converge to a more suitable result.

E-Data Fitting

In location E, the information of the fit, experimental conditions, value of lamp threshold offset, goodness-fit-statistics, calculated value of reduced mobility and other informations can be found. It is also possible to export these data to an excel file.

2.5.1 Signal's de-noising techniques

As it is well known, signals obtained in real systems have noise associated with them. When the signal-noise ratio (SNR) is high [50] we can rule out the noise effects, but we found that for some of the gases studied the signal-noise ratio obtained from some recorded signals can be small and sometimes it was impossible to make reasonable fits to the data. To improve this situation and also to obtain better and more reliable fits, after removing the background noise to the main signal file, de-noising of the signal was made. This signal improvement was accomplished using wavelets theory and is based on the work proposed by D.L. Donoho and I.M. Jonhstone[51]. According to the authors, de-noising data can be achieved in 3 steps, by choosing a right threshold and a suitable family of wavelet. In this work it is assumed also that the signal is deteriorated only by near Gaussian white noise with mean zero and a known variance σ^2, although it is possible to generalize it to other types of noise [52].

In our case the Wavelets Toolbox from MATLAB ® library was used to apply the proceedings, described in [51], in a more easy and automatic way, and allowing the use of few computational resources by Azarus application. Regarding our data it was considered that the noise present in the signals recorded is in generally random, and therefore, it is white noise (Gaussian dispersion).

From the toolbox, the WDEN function was used to de-noise the signal obtained. This function is an automatic de-noising process of a one-dimensional signal, using wavelets that can be optimized and made suitable for different signals by changing the parameters of the function. In order to determine which parameters yield the best results, Mean Square Error, MSE was used, as metric in the following sections, normally used in signal and image processing. It is represented by equation 2.2, where N is the total size of the data signal and n(i) and s(i) are each element of the de-noised signal and the original, respectively.

$$MSE = \frac{\sum_{i=1}^{n} (n(i) - s(i))^2}{N} \tag{2.2}$$

However, the information given by this metric is doubtful and often debated because if simple smoothing de-noising is considered, the lesser the smoothing, the lesser is the noise removed, resulting in less differences between the new signal and the original, and so leading to better metric results. However in this scenario, less noise has been removed which is not the objective. The same situation happens with other current metrics usually used, like MAE (Mean Absolute Error), SNR (Signal to Noise Ratio) or PSNR (Peak Siganl to Noise Ration). Nevertheless, as it will be discuss in the next

segments, the de-noising technique applied to the signal, varying only the parameters of WDEN function, visually showed no significant differences in the final generated signal (figure 2.17). Hence, the MSE was still used as the criteria, considering that the parameters yielded minor error, thus better conserving the features of the original signal.

Choice of Thresholds

There are two general categories of thresholding, hard or soft (the plots and equations about thresholding types can be found in appendix A). In hard thresholding, the features of the signal are preserved, like peak heights, and its even possible to recreate the old signal from the de-noised one. The soft threshold generally produces reconstructions with less noise than the hard, or approximately none, but at the cost of shrinking the signal's real features.

The nature (hard or soft) of wavelet thresholding relies on the choice of a threshold value [53]. Some typical thresholds used in signals and images de-noising are VisuShrink[54], SUREShrink[55] and minimax method, all developed by Donoho and Johnstone.

Wavelets Toolbox provides 4 simple commands that apply these 3 selection rules:

- **Rigrsure:** Based on SUREShrink method.
- **Sqtwolog:** Based on VisuShrink, where a single value of threshold is applied globally to all the wavelet coefficients.
- **Heursure:** This option is a mixture of the last two. It uses the SURE method if the signal-noise ratio is not poor. Otherwise, it uses a fixed threshold. This option is quite useful when we are unaware of the conditions of the signal.
- **Minimaxi:** Based on minimax principle, normally used in statistics.

We tested these selection rules and the results are shown in figures 2.16 and 2.17. Regarding the selection rules mentioned before, the *'rigrsure'* based on SURE method was the one with the best metrics. Another aspect to take into account was that the results obtained by selection rules *'heursure'* and *'sqtwolog'* were the same. This outcome is due to the fact that *'heursure'* rule is a mixture from *'sqtwolog'* and *'rigrsure'* rules and if the signal to noise ratio is very small, this option use a fixed form threshold given by *'sqtwolog'* selection rule. Notice in figure 2.17 that the de-noised signals obtained for the different selection rules were very similar.

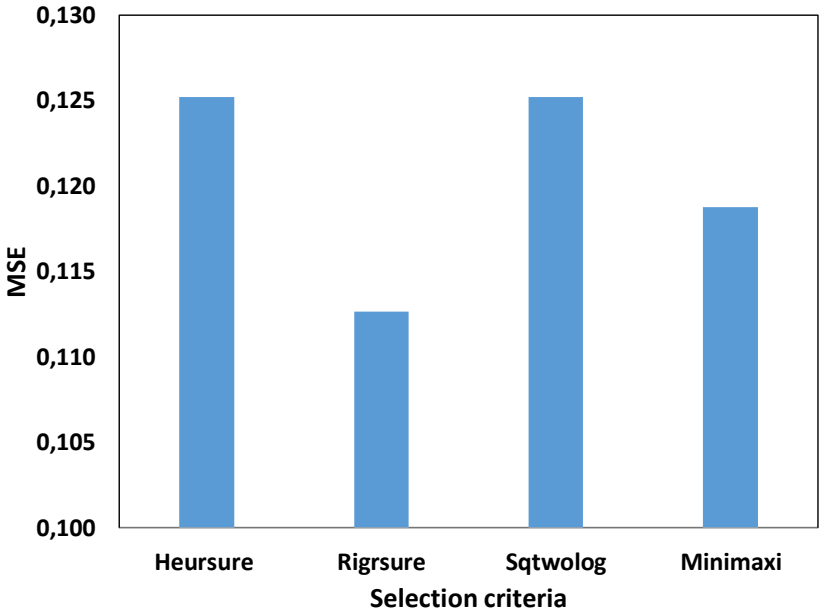

Figure 2.16: Metrics of de-noising process depending on the choosen criteria of thresholding selection

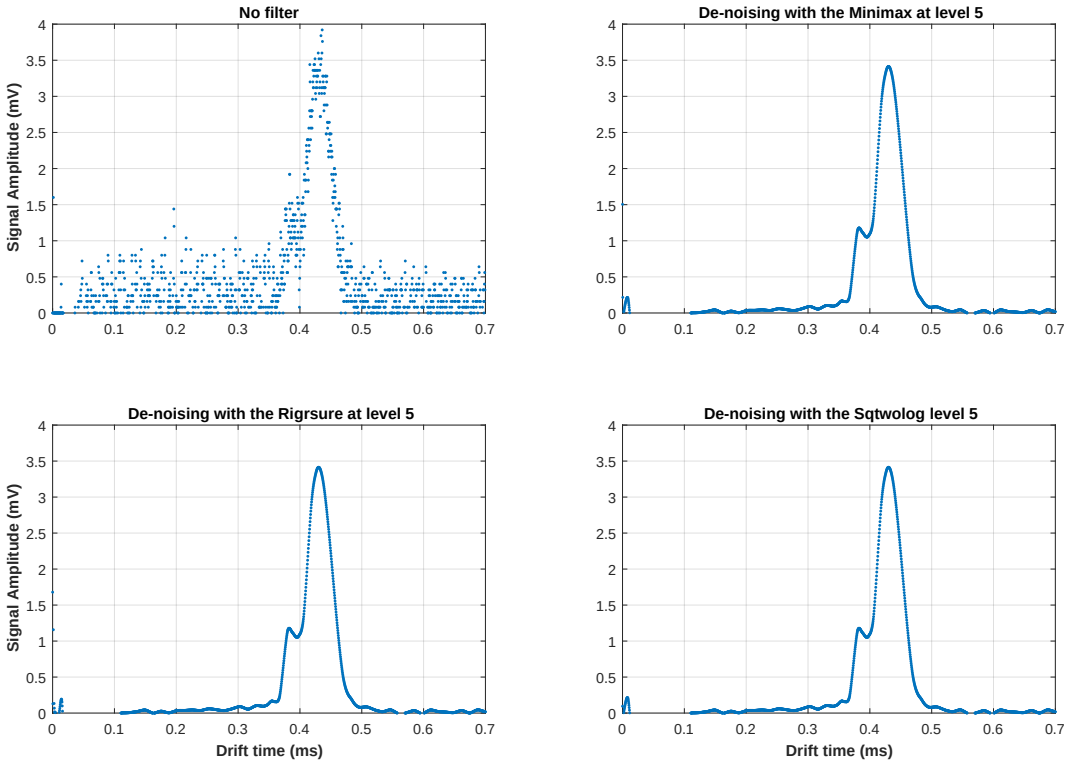

Figure 2.17: Time-of-arrival spectrum averaged over 128 pulses for pure N_2, with different levels of thresholding

Choosing the right wavelet

Another point is which family of wavelets is the proper one to choose. An extensive theoretical study of wavelets and their characteristics can be found in [56, in chapter 6]. From here we chose 3 different families of wavelets commonly used: *Dauchebies*, *Symlets* and *Coiflets*. For the first two wavelets were tested with orders of 2 up to 8 and 3 up to 5 in the case of the third family.

The results obtained, shown in figure 2.18, were similar for every wavelets used, with $cf3$ (*coiflets* of third order) and $db6$ (*Dauchebies* of sixth order) having a slightly better performance.

After this study, we concluded that the best parameters were:

- **Wavelet**: *Coiflets* 3 [Wavelets info and graphs can be found in 56, 57]
- **Threshold selection rule:** Rigrsure
- **Threshold level:** 3

Note that we reduced the level of thresholding (figure 2.19) because if the level of de-noise is high (without any noise contributions) and the fit does not overlap the de-noised signal (which could happen), the value obtained for the peaks centroid is poorly determined, specially for smaller peaks. This influence can be observed in the residual analysis. So we discoverd that by reducing the threshold level for a value equal to 3 we obtain smoothly results as can be seen in figure 2.15.

2.5.2 Fit Methodology

After the signal processing described in section 2.5.1 the program's next step is to perform an appropriate fit to the signal. This section is intended to describe the techniques used to determine the fits, as well as evaluate their quality and how it is carried out to the determination of their error.

In order to avoid disturbances in the fits due to the signal induced by UV lamp contributions, the data is divided into two parcels, the first concerning the lamp's signal represented in the figure 2.15(a) and the second referring to the signal induced by the group of ions. Then it is performed a first Gaussian fit to the data, which will allow the program to identify the best starting point as well to remove possible outliers. After that, a second fit is performed with the information retrieved from the first one, improving the results obtained. Both fits are performed with the Non-Linear Least Squares method with trusted region reflective as the convergence algorithm. This fit

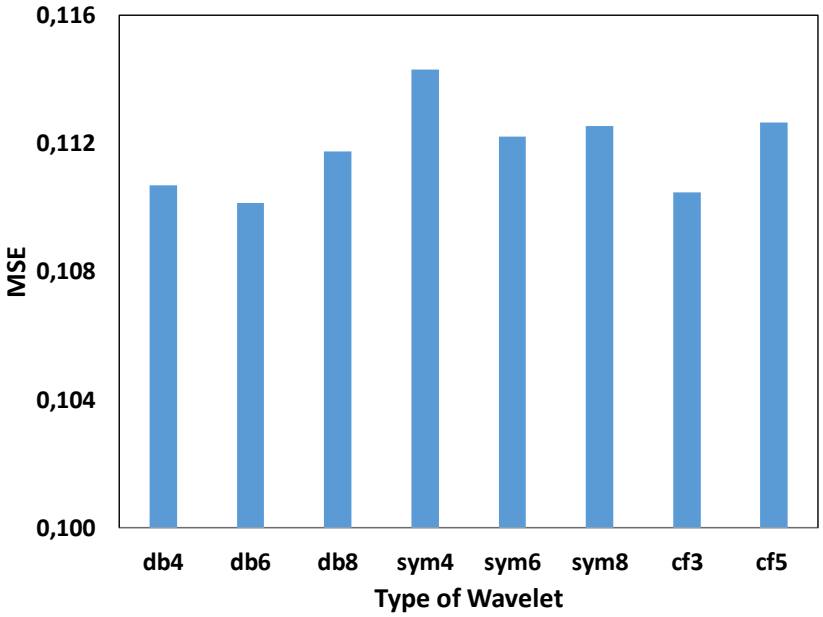

Figure 2.18: Metrics of de-noising process depending on the threshold selection rule

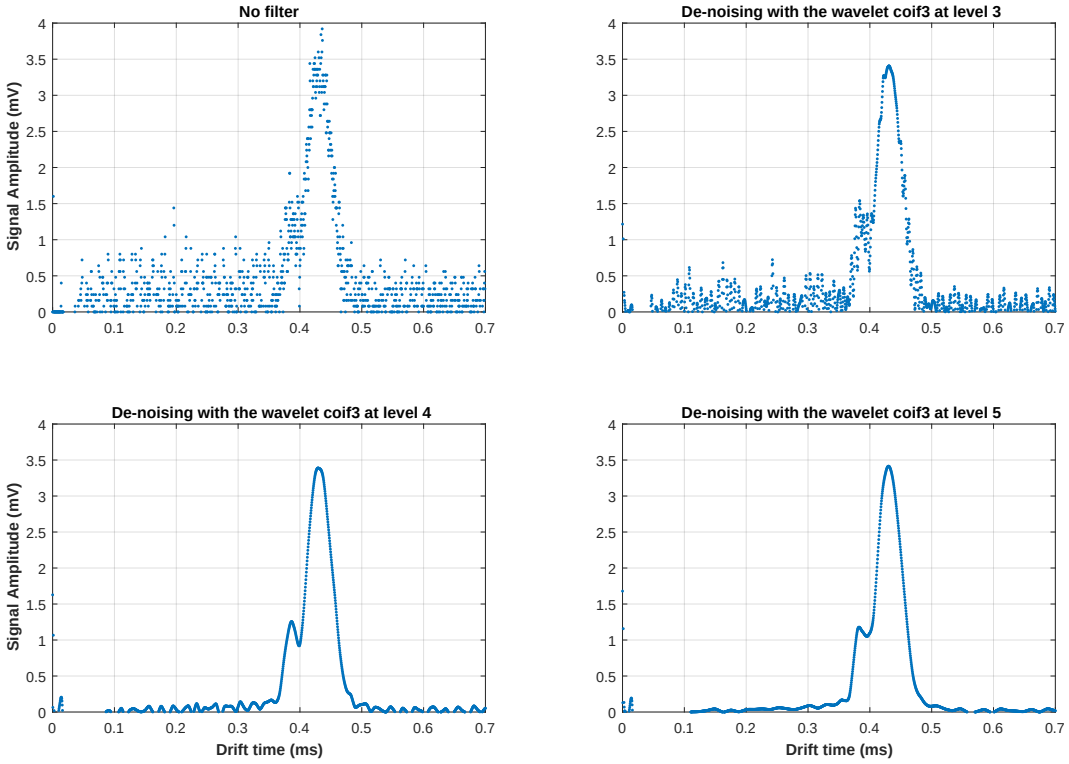

Figure 2.19: Time-of-arrival spectrum averaged over 128 pulses for pure N_2, with different de-noising techniques

methodology was applied in our program through the resources developed by Mathworks ®. An explanation of the resources used can be found at [58, 59], and in the references therein for more information about the mathematical approach to this method or to the algorithms behind it.

The programme is usually capable of generating the proper fit to the data, nevertheless, as explained before, the user has the choice to redefine the type and initial conditions of the Gaussian function, if the results obtained are not satisfying.

Regarding the error in the peaks' centroid, an approximate formula, suggested by [60], calculates the error of the peak centroids when the Gaussian fit is estimated through the least-squares method, is described in 2.3.

$$\text{Peaks centroid uncertainty} = \sqrt{\frac{2.355\sigma}{a}} \tag{2.3}$$

were σ is the standard deviation and a is the amplitude of the Gaussian function. According to the authors, this expression is only valid when the background can be negligible and also the number of data points used in fitting is sufficiently large.

The process of evaluating the fit is made in three steps:

- **Visualizing the correlation between fit and data**
- **Goodness-of-fit Statistic tests**
- **Residuals Analysis**

Regarding the Goodness-of-fit Statics tests, the Adjusted R-square is used as the main parameters, since it measures how successfully the fit represents the data variation of the signal by determining the correlation between the signal values and the fit's prediction. A value closer to 1 (maximum) establishes that almost all data of the signal is taken into account by the fit. As an example, a value of 0.9795, it means that the fit explains 97.95% of the total variation in the data about the average.

2.5.2.1 Residuals Analysis

Residuals are useful for detecting outlying values and checking if the data is well represented by a specific fit. There are several types of residual plots that help to quantify their influence in the data. From them, we chose a plot of residuals and a normal plot. About the first one, shown in figure 2.15(c), it reproduces the differences between the original signal and the values predicted by the fit. If the residuals are not distributed randomly in a straight line of zero value (y=0) and if it is possible to notice the presence of a curvilinear relationship between the data, this suggests that a fit with a higher term is more suitable. Concerning the second plot, after all

systematic variation has been removed from the data, the residuals should look pretty much as a sample from a normal distribution [61].To confirm this hypothesis, we used the probplot function from Matlab, that creates a normal probability plot and allows the comparison with our data distribution. This type of plot is presented in figure 2.15(d), and the fit residuals follows a normal distribution if they override the dashed line between 0.05 and 0.95 of probability. If not, the fit is considered inadequate.

2.6 Ion Identification Process

Even though this method does not allow direct identification of the ions, it has some features which allows its indirect identification. We will now explain briefly the general procedure used in ion identification.

One of the features of this method is the capability of controlling the voltage across the GEM (V_{GEM}) and thus, the energy gained by the photoelectrons as they move across the GEM holes. This enables the identification of the primary ions based on the ionization energies, and identifying the primary ions will allow to pinpoint secondary reaction paths that lead to the identification and validation of the products collected in the grid. After positively identifying the ions originated in their parent gases, Blanc's law can be most useful in the identification of the ions present in the different mixtures, and that appear in the obtained spectra.

Although elaborated, the experimental method described together with the knowledge of the dissociation channels, product distribution and rate constants represents a valid solution to the ion identification problem.

2.7 Limitations of the experimental measurements

Every system has its own limitations and an operating range in which results can be trusted. Examples of limitations, intrinsic to our device, are the effects of the impurities due to system degassing, the electric field and pressure values possible to use in order to obtain a signal induced by the group ions with quality or without the occurrence of discharges that may damage the components, and also the limits associated with the electronic equipment used.

The impurities efficiently convert ions of the gas, specially the rare ones like Ar and Ne, to other ion types through collisions. Particularly, if the impurities are polar or highly polarisable, they will produce clusters or if they have a low ionisation potential they can be ionised at the expense of primary ions through charge transfer

processes. An extensive study about the effects of impurities in the signal for rare gases was performed by P.N.B Neves [4].

These impurities have two main origins: outgassing processes and impurities present in the gases used (see section 2.3). Regarding the outgassing process, it refers to the slow release of gases that were trapped, frozen or absorbed in the chamber material. Their extent depends on the materials used which have different rates of outgassing, contact area of the material and volume of the detector. The rate of outgassing is temperature dependent, which means that the impurities, mainly water molecules, could be reduced using the vacuum pump and by heating the experimental set-up, this is , heating up the chamber which contributes to the degassing of the system. However, this it is not possible because the epoxy used to glue the feedthroughs does not withstand temperatures above 100 ºC.

Because these contributions are hard to reduce, a rough calculation of the system degassing for periods of 10 and 60 min was made in order to quantify its effects on the mixture. For this estimate it was only considered the chamber, which has a volume of 2.84 dm^3, and the components inside (electric field rings, connectors, stainless steel and Teflon supports). The epoxy is one of the materials that contributes to the outgassing, however it was not included in this estimate because it was difficult to quantify its contact area. Additionally, the contributions from the pipes were not included. The outgassing rates used in this calculation were taken from [62]. According to the estimation made, after ten minutes of filling, the pressure due to impurities accomplished by outgassing was $6x10^{-3}$ Torr, and $3.7x10^{-2}$ Torr after 60 min of filling. This last value was approximately close to the one measured by the pressure gauge. For a gas filling with 8 Torr, after 60 min the outgassing contributions represent 0.47% of the final mixture, which could affect the type of ions formed.

In order to minimize these outgassing effects, a strict gas filling procedure was carried out. No measurement was considered until the signal stabilised, and all measurements were done in a 2–3 minutes time interval to prevent the degradation of the ions' induced signal due to outgassing. Before each experiment the vessel was vacuum pumped down to pressures of 10^{-6} – 10^{-7} Torr to guarantee minimal contamination of the system.

Regarding the limited range of the reduced electric field values used to determine the ions' mobility, it has two distinct origins: on one hand the electric discharges that occur at high E/N values (could be influenced by the ageing of the photocathode, see section 2.4); and on the other hand the observed deterioration of the time-of-arrival spectra for very low values of E/N (below about 5 Td, depending of the gas).

Chapter 3

Results and Discussion

3.1 Introduction

In Time Projection Chambers (TPC) with great volume, a fundamental aspect to a proper and improved operation is to understand how the detector's response is if the gas parameters such as composition, pressure and temperature are changed [63]. It was common practice to use the Ne-CO_2 mixture as filling gas in these detectors, such as in NA49, CERES and ALICE TPCs.

Usually the Ne choice lies on the high mobility of its ions and long radiation length, helping to reduce the charge accumulation in the drift volume. As for CO_2, it is used as quencher to avoid ageing. Some TPCs use CH_4 as a quencher instead of CO_2, however this gas leads to intense ageing of the detector after a few years of operation [64]. The Ne-CO_2 mixture also has a small diffusion which is desired in this kind of detectors. Normally, the gas choice is highly dependent on simulations since experimental data on effective ion mobility for mixtures of two and three gases is scarce, although this data is important for the improved performance of these gaseous detectors, with especial attention for ALICE TPC (A Large Ion Collider Experiment - Time Projection Chamber).

The ALICE TPC consists in a 90 m^3 volume filled with gas, which is the detecting medium, and its performance depends crucially on the gas choice, stability and quality, since these influence the charge transport in the drift volume and the amplification processes in the readout chambers [65]. To date, not much data on ion mobility in mixtures relevant for the ALICE TPC exist or dedicated studies were performed about the filling mixtures used like Ne-CO_2 and Ne-CO_2-N_2 [63], although mobility measurements for several gases has been performed since long [8–11]. In the scope of the RD51 collaboration we have been asked to study the dynamics of different gas

mixtures that could be used to fill the ALICE TPC in order to be able to optimize the mixture in the readout chambers.

In this chapter we present the results and discussion of the mobility studies conducted and it is divided in three main sections: studies of CO_2 mixtures in section3.2, which includes the complete study of the ions of CO_2 in its parent gas (section 3.2.1), in mixtures with Ar (3.2.2), with Ne(3.2.3) and with N_2 (3.2.4). The study of N_2 mixtures in its parent gas (section 3.3.1) and also the preliminary results of Ne-N_2 mixtures (section 3.3.2); and finally the results obtained for Ne-CO_2-N_2 (90-10-5), in section 3.4. The results for pure TMA and Xe-TMA mixtures are presented in appendix B.3, although a discussion for this gas is not presented in this report.

In the case of the mobility studies that are concluded, to guarantee that the results presented are reproducible and trustworthy, each mobility measurements for different conditions of field, pressure and voltage across the GEM were repeated four to ten times, and the final result considered is the arithmetic average of all results obtained for the same conditions. The errors in the tables and plots of this chapter, as well as in appendix B, are a result of the sum of systematic and statistical error for the drift distance and drift time.

Regarding the graphics, 4 different types will be shown. The first one is a time-of-arrival spectrum that was recorded using a digital oscilloscope and corresponds to an average of 128 pulses, with the background noise subtracted. To this data is performed a signal de-noise and a fit, as was described in section 2.5. The second is a plot of the inverse of reduced mobility versus the reduced electric field in the case of pure gas or the inverse of reduced mobility versus the relative amount of one of the components, if the study concerns a gaseous mixture. In this type of plot, the values of reduced mobility obtained by other authors are also shown for comparison.

In order to explain the nature of a peak or whether there are impurities present that will influence the mobility of the ions detected, a signal degradation study is performed when considered necessary. This analysis consists in maintaining the original gas mixture in the detector for a longer period of time and recording the signal in equally-spaced time intervals. As a result, the time-of-arrival spectra should display a significant change in the peaks relative abundance if they are due to the presence of impurity molecules. Normally the impurities present are mainly ions and water cluster, originated by outgassing processes or due to the purity of the gas.

Finally, the last plot type exhibits the reaction paths that occur in a specific gas, enlightening which ions had enough time to be produced. The concentration of reactants were obtained through the numeric integration of equation 1.14, when the pseudo-first

order reaction could be applied, as described in 1.2.6.

In order not to overload the chapter, the results obtained for other experimental conditions can be found in appendix B. An explanation of the rare gases behaviour (Ne, Ar, Xe) which were performed by P.N.B. Neves in this experimental system can be found in [4, 24].

3.2 CO_2 Mixtures

3.2.1 Pure CO_2

Carbon dioxide is one of the essential constituents of the atmosphere, being present in many biological and chemical processes. Studies of collisions between electrons and this molecule have been theoretically and experimentally studied since 1920 and it is therefore one of the best known molecules, and it is widely used in laboratory studies and manufacturing processes. The carbon dioxide molecule have a ionization energy equal to 13.78 eV. [66]. The mobility of this molecule in its parent gas was first measured in 1971 by W.T. Huntress Jr for pressures bellow 1 Pa.

Regarding our mobility results for pure carbon dioxide (CO_2), we measured the mobilities of its ions for different reduced electric fields, E/N (from 6 Td up to 45 Td) and for a pressure in the 8 Torr range at room temperature. In several time-of-arrival spectra only one peak was observed. An example of this time-of-arrival spectra is displayed in figure 3.1. In this case, the experiment was conducted at 8 Torr, at reduced electric field of 15 Td, and for a voltage across the GEM, V_{GEM}, of 20 V.

For each pair of pressure and reduced electric field studied, the respective mobility was determined according to the method described in chapter 2. The resulting mobilities, K, were plotted against the reduced electric field, E/N, and an extrapolation was then carried out in order determine the reduced mobilities of these ions when $E/N \rightarrow 0$ (Langevin's limit). Taking this into account, the experimental value for the mobility of the only peak observed is 1.17 $cm^2\ V^{-1}\ s^{-1}$ (see figure 3.2 and table 3.4).

The ion identification process is extremely important. Furthermore, when dealing with molecules composed of several atoms, such as CO_2, it is important to exclude some possible reactions in order to identify the ion species present. By keeping V_{GEM} as low as possible we were able to reduce the variety of primary ions produced in the GEM holes. For a V_{GEM} of typically 25 V, the photoelectrons can gain a maximum energy of 26 eV, since the photoelectrons' initial energy can reach up to 1 eV. table 3.1 summarizes the possible reactions due to electron impact in CO_2 for electron energies of 25 eV, together with the respective cross-sections, appearance energies and

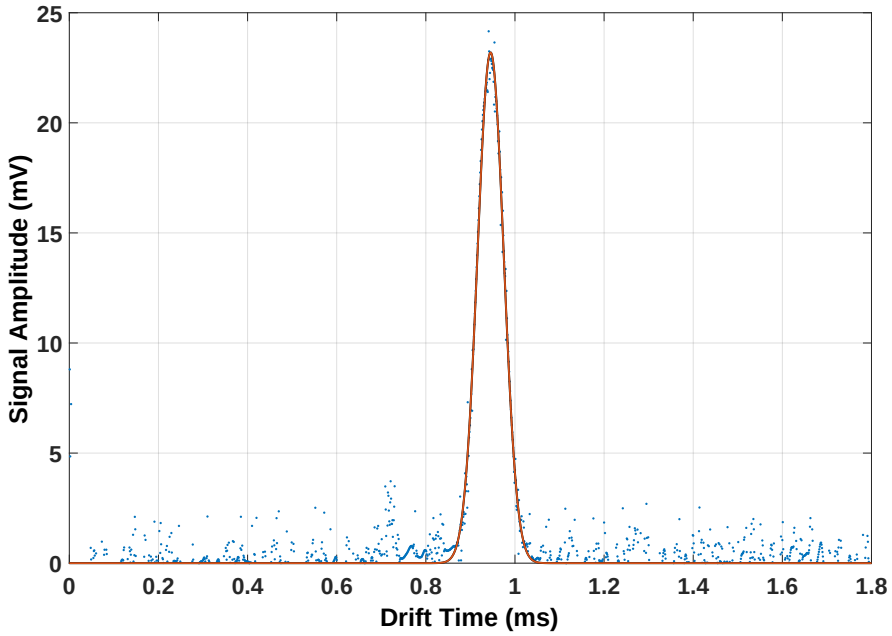

Figure 3.1: Time-of-arrival spectrum of an average of 128 pulses for pure CO_2 at a pressure of 8 Torr, and for E/N=15 Td, V_{GEM}=20 V, at room temperature.

the product distribution. The displayed probabilities were obtained using the cross sections for each primary ion of CO_2 and the total ionization cross section provided in [66], allowing us to infer the product distribution of this primary ionization. All these primary ions (CO_2^+, CO^+, O_2^+) will rapidly undergo reactions, being transformed into secondary ions. Table 3.2 presents a summary of secondary reactions, product distributions, and reaction rates, for collisions between CO_2 and the primary ions from table 3.1, at room temperature.

Table 3.1: Ionization products, ionization cross sections for electron impact (E=25 eV) on CO_2, appearance energies (A.E.), and respective product distribution [Adapted from 66].

Reaction	**Cross Sec. (10^{-16}cm^2)**	**A. E. (eV)**	**Prod. Dist.**
$CO_2 + e^- \rightarrow CO_2^+ + e^-$	1.00	13.8	84.7 %
$CO_2 + e^- \rightarrow CO^+ + \frac{1}{2}\,O_2 + e^-$	0.044	19.5	3.7 %
$CO_2 + e^- \rightarrow O^+ + CO + e^-$	0.064	19.1	5.4 %

Taking a closer look at table 3.1 is possible, see that the most probable primary ion to be formed by electron impact is CO_2^+. In addiction, the results described in table 3.2 allow us to conclude that three ions can be formed CO_2^+, $CO_2^+.CO_2$ and O_2^+.

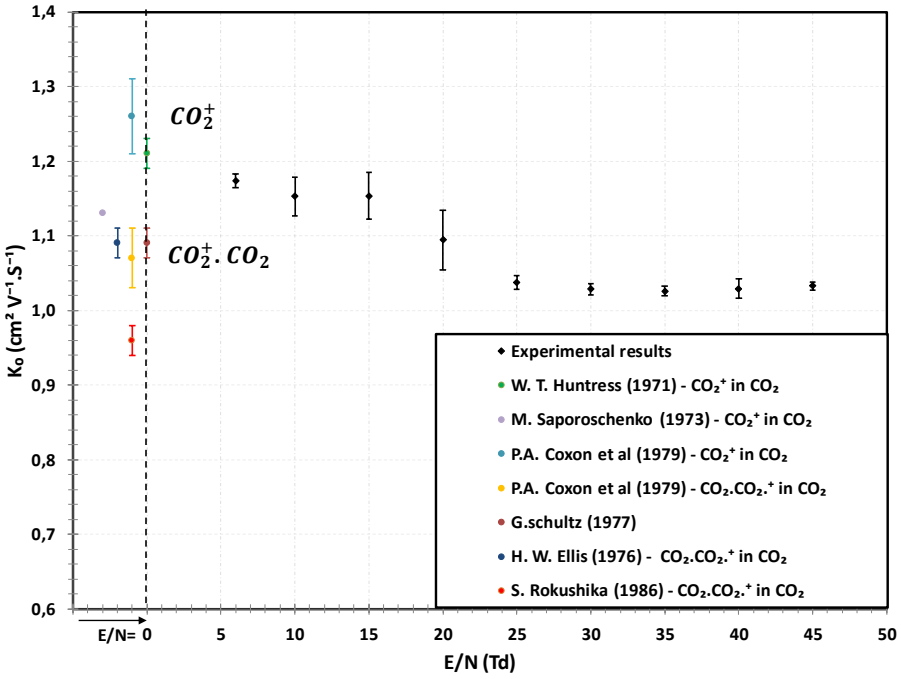

Figure 3.2: Reduced mobility of the ions produced in CO_2 for a pressure of 8 Torr and for E/N values in the 6-45 Td range.

figure 3.3 shows the conversion of the primary into secondary ions over the time of the reactions. The concentration of the different ions was determined through the pseudo first order method using the rate constants described in table 3.2. It was considered that the initial concentration of each type of ion depends on the gain given by the GEM and the primary products distribution that can be seen in table 3.1. The concentration of CO_2 neutrals was considered constant (8 Torr) through all reactions, and the quantity of molecules present in the detector is approximately one hundredth of those present at NTP conditions ($2.5x10^{19}$).

Table 3.2: Secondary reactions, product distribution and rate constants for the collisions of the primary ions of CO_2.

Reaction	**Rate Const. (k)**	**Reference**
$CO_2 + CO_2^+ \rightarrow CO_2^+ + CO_2$	$0.370 \pm 0.037 \times 10^{-9}$ $cm^3 s^{-1}$	
$CO_2 + CO^+ \rightarrow CO_2^+ + CO$	$1.10 \pm 0.11 \times 10^{-9} cm^3 s^{-1}$	[67]
$CO_2 + O^+ \rightarrow O_2^+ + CO$	$1.10 \pm 0.22 \times 10^{-9} cm^3 s^{-1}$	
$CO_2 + CO_2^+ + M \rightarrow CO_2^+.(CO_2) + M$	2.4×10^{-28} $cm^6 s^{-1}$	[68]

Regarding the formation of O_2^+, the reaction only takes approximately 10 ns to convert almost all O^+ into O_2^+. In spite of that, only one peak is visible. Since the amount of O_2^+ is residual, we believe that it may be enclosed within the main peak, once O^+ has a very small relative concentration (representing only 5.4 % of the total ions distribution).

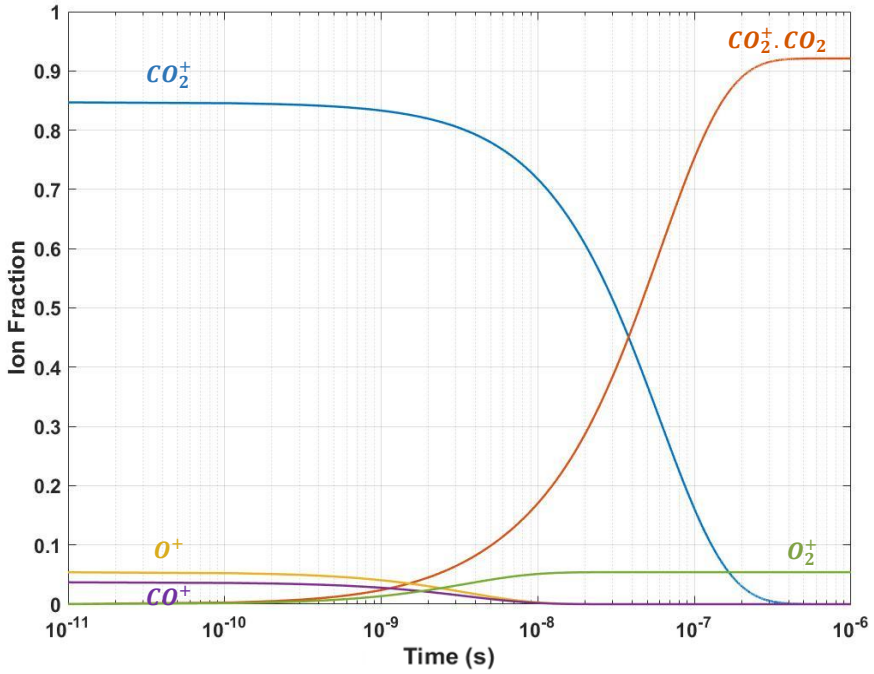

Figure 3.3: Ion abundance with time for pure CO_2 calculated with Matlab ®.

So, the ion responsible for the peak is either CO_2^+ or $CO_2^+.(CO_2)$. At 8 Torr, the cluster formation is the slowest reaction present in pure CO_2. Nevertheless it is only required 0.3 μs to convert 99% of all CO_2^+ into $CO_2^+.(CO_2)$. This corresponds to ≈0.003% of the total drift time when a reduced electric field of 15 Td is applied. Even though the charge transfer reaction is much faster than that the cluster (≈70 ns), after a charge transfer between CO_2 molecules, a 3-body-collision can occur leading to the cluster formation.

A comparison with the zero field mobilities found in the literature is shown in table 3.3 and in figure 3.2. As can it be seen, many authors identified both CO_2^+ and $CO_2^+.(CO_2)$ in pure CO_2. In spite of the fact that the working pressures of these experiments were different form ours, an extrapolation can be made.

P.A. Coxon *et al* [71] could identify both ions in pure CO_2. In their experiment they measured mobilities of CO_2^+ for E/N between 40 and 1400 Td and for pressures between 0.03 to 0.1 Torr, obtaining a zero field mobility of 1.26 ± 0.05 $cm^2V^{-1}s^{-1}$. In the

Table 3.3: Zero field mobilities of CO_2^+ and $CO_2^+.(CO_2)$ ions in pure CO_2. In some cases the extrapolations for zero-field mobilities were performed by Kalkan, 2015 [16].

Reference	Mobility ($cm^2V^{-1}s^{-1}$)		Pressure range (Torr)
	$CO_2{}^+$	$CO_2^+.(CO_2)$	
W.T. Huntress (1971) [69]	$1.21^{+}_{-}0.02$	-	<0.008
M. Saporoschenko(1973)[70]	1.13	-	0.58
P. A. Coxon *et al* **(1979) [71]**	$1.26^{+}_{-}0.05$	$1.07^{+}_{-}0.04$	0.03 to 0.1 0.4 to 0.5
G. Schultz *et al* **(1977)[72]**	-	$1.09^{+}_{-}0.02$	760
H. W. Ellis *et al* **(1976)[73]**	-	$1.06^{+}_{-}0.02$	760
S. Rokushika *et al* **(1986) [74]**	-	$0.96^{+}_{-}0.02$	760
This work (2015) [31]	$1.17^{+}_{-}0.04$		8

case of the dimer, $CO_2^+.(CO_2)$, it was measured for E/N between 14 and 200 Td and for pressures between 0.4 to 0.5 Torr, obtaining $1.07^{+}_{-}0.04$ $cm^2V^{-1}s^{-1}$ when E/N→0. W. T. Huntress Jr. [69] performed measurements at pressures below 0.008 Torr obtaining a zero-field mobility of $1.21^{+}_{-}0.02$ $cm^2V^{-1}s^{-1}$ for CO_2^+. This value is in good agreement to the one reported by P.A. Coxon *et al*. Both experiments were specially careful with the purity of the gas samples. M. Saporoschenko [70] also detected CO_2^+ in pure CO_2. He measured the mobility of this ion for E/N≥140 Td at 0.58 Torr and through an extrapolation to zero field, a mobility value of 1.13 $cm^2V^{-1}s^{-1}$ was obtained. However, as described in [71], this system used a glow discharge as ion source and identified the principal ions present in pure CO_2 as CO_2^+, O_2^+ and $O_2^+.CO_2$ which could suggest that the system had a potential oxygen contamination (≈100 ppm) modifying the mobility values distribution, thus explaining the discrepancy between this measure and those reported by W. T. Huntress and P. A. Coxon.

Regarding the experimental systems of G. Schultz *et al* [72], H.W. Ellis el al [73] and S. Rokushika *et al* [74] they worked at atmospheric pressure. In this pressure conditions a fast formation of large clusters of CO_2 are expected, due to its polarisability, and the ion core should have a minor role in the cluster aggregation. In contrast to the experiments of Ellis and Rokushika, the first experiment does not allow the direct identification of the ion measured due to the lack of a mass spectrometer. However, their work was conducted at the same pressure and temperature as the second ones and obtained a similar mobility value of the cluster.

Taking a closer look at figure 3.2, it can be noticed a step in the mobility value for

E/N between 10 and 20 Td. We cannot explain the reason for this effect and this does not help in the identification of the ion that appears in our pressure conditions. In one hand if the extrapolation of the K_0 for $E/N \rightarrow 0$ is made with values greater than 20 Td for E/N, we obtain a K_0 of 1.07 $cm^2V^{-1}s^{-1}$ which is closer to literature values for the cluster. In the other hand if all data is consider in the extrapolation, we obtain a value of 1.17 $cm^2V^{-1}s^{-1}$ which is approximately the value of mobility encountered for CO_2^+. Despite the chemical reactions suggesting that the ion is $CO_2^+.(CO_2)$, with our experimental data we cannot claim with absolute certainty which ion causes the peak obtained.

Table 3.4: Mobility of the ions observed in this work for pure CO_2 at room temperature (298 K) for different E/N and a pressure of 8 Torr.

E/N **(Td)**	**Mobility ($cm^2V^{-1}s^{-1}$)**
$5.89^{+}_{-}0.01$	$1.17^{+}_{-}0.01$
$9.85^{+}_{-}0.05$	$1.15^{+}_{-}0.03$
$14.80^{+}_{-}0.04$	$1.15^{+}_{-}0.03$
$19.74^{+}_{-}0.04$	$1.09^{+}_{-}0.04$
$24.63^{+}_{-}0.03$	$1.04^{+}_{-}0.01$
$29.49^{+}_{-}0.03$	$1.028^{+}_{-}0.007$
$34.42^{+}_{-}0.03$	$1.026^{+}_{-}0.007$
$39.31^{+}_{-}0.02$	$1.03^{+}_{-}0.01$
$44.20^{+}_{-}0.01$	$1.033^{+}_{-}0.005$

Both our results and the ones present in the literature are substantially different from the theoretical ones of CO_2^+, K_0=1.82 $cm^2V^{-1}s^{-1}$ sustained with the Langevin limit. If CO_2^+ is the ion responsible for the peak observed and the cluster formation does not occur, we suspect that the inconsistency with the theoretical value is due to charge transfer phenomena between the parent gas and the CO_2 ion. As for $CO_2^+.(CO_2)$, Kalkan [16] reported that due to the mass dependence of the Langevin formula, the mobility of clusters is expected to be smaller than the polarisation limit given by Langevin.

The mobility values obtained for pure CO_2 for a pressure of 8 Torr and for E/N values between 6 and 45 Td are shown in table 3.4.

3.2.2 Ar-CO_2

In argon-carbon dioxide (Ar-CO_2) mixtures with CO_2 concentrations higher than 20% only one peak was observed, as can be seen in figure 3.4. The ion responsible for this peak is the same ion present in pure CO_2, CO_2^+ or $CO_2^+.(CO_2)$.

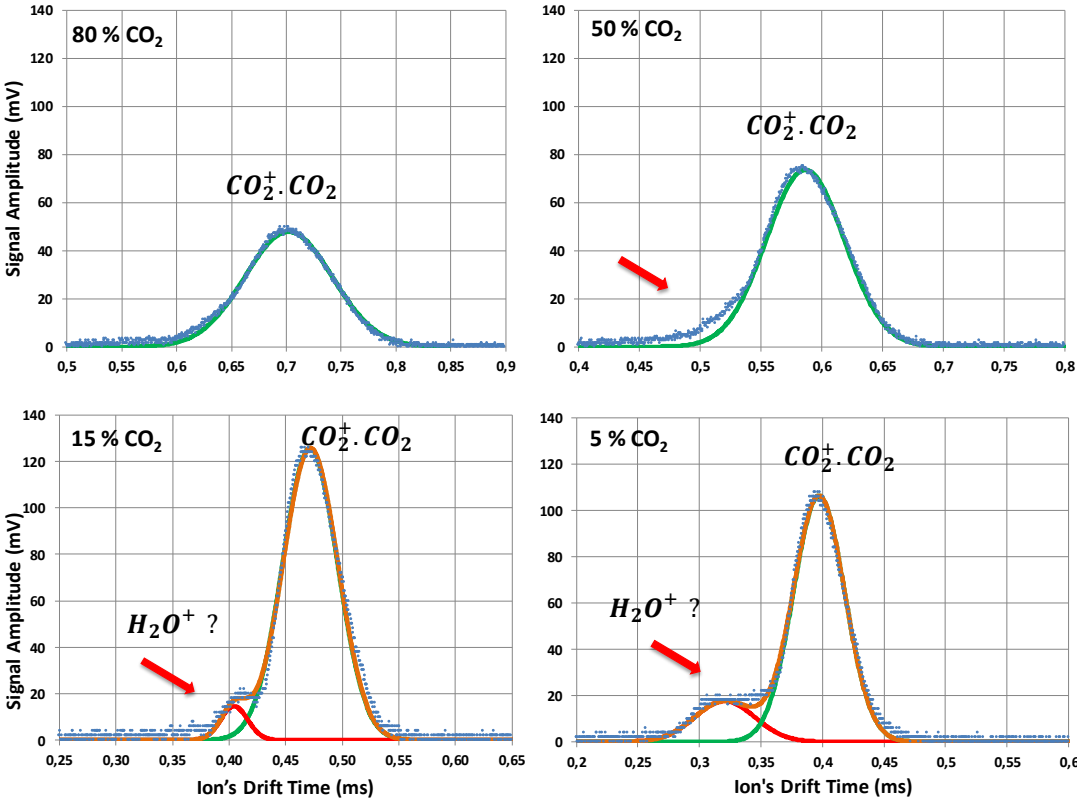

Figure 3.4: Time-of-arrival spectrum of an average of 128 pulses several Ar-CO_2 mixtures (20%, 50%, 70%, 95% of CO_2) at a pressure of 8 Torr, temperature of 298 K and at a pressure of 8 Torr, and for E/N=20 Td, V_{GEM}=25 V (background noise was already subtracted). The ions responsible for the peaks appearing in this time-of-arrival spectra are CO_2^+ or $CO_2^+.(CO_2)$ and probably H_2O^+.

As known from the literature the electron impact ionization cross section for Ar at 25 eV is 1.24×10^{-16} cm^2 [75] which is similar to the cross section for CO_2 (at 25 eV, 1.18×10^{-16} cm^2 [76]), therefore it is expected that, even at low CO_2 concentrations, both ions from Ar and CO_2 are produced. In addition, according to the rate constant for the formation of Ar_2^+, Ar^+ ions are more likely to react with CO_2 (reaction 3.1),

$$CO_2 + Ar^+ \rightarrow CO_2^+ + Ar \tag{3.1}$$

$$Ar^+ + 2Ar \rightarrow Ar_2^+ + Ar \tag{3.2}$$

than with Ar via reaction (3.2) (k=1.2×10^{-31}cm^{6}s^{-1} [4]) which has a lower reaction time. As a result, the presence of Ar^+ ions leads also to the formation of CO_2^+, modifying the ion product distribution of pure CO_2 (by reinforcing the channel leading to the formation of CO_2^+), which results in an amplitude growth of the main peak (see figure 3.4).

Taking a closer look at figure 3.5 it is possible to observe the evolution of the types of ions formed along the drift region. The ion fraction is plotted as a function of time for a pressure of 8 Torr and it is illustrated the case of 95% Ar and 5% CO_2 where the reaction time has more influence in the final ion detected. In this case it takes approximately 120 μs to convert 99% of the ions into $CO_2^+.(CO_2)$ clusters. This reaction time should decrease when larger quantities of CO_2 are present in the mixture. When an electric field of 20 Td is applied in the chamber the drift times measured extended between 400 μs and 735 μs for 5% CO_2 to 95% CO_2, respectively. With this in mind, for 95% Ar and 5% CO_2, according to the reaction rates, at least one third of the drift distance is travelled as CO_2^+, influencing the mobility of the final ion measured. As for the formation of the argon dimer (reaction 3.2) it is unlikely to happen because, as can be seen in figure 3.5, even if 95% of the initial ions are Ar^+, the conversion to Ar_2^+ is scarce. This happens because, as already be mentioned, Ar^+ transfers more easily its charge to CO_2 at low pressure.

Another key point of this study is that when the concentration of CO_2 in the mixture is bellow 20%, a second peak begins to appear. At first we suspected that this second peak, of smaller dimensions, was due to the formation of O^+ since its partial cross section at 25 eV represents 5.4% of the total ionization cross section (see table 3.1). However, when a voltage of 18 V, below the appearance energy of the O^+ (19.1 eV), was applied to the GEM, the second peak remained visible under the same circumstances, for CO_2 concentrations lower than 20%. Another possibility could be the detection of both CO_2 and its dimer $CO_2^+.(CO_2)$, due to an incomplete reaction. Yet we believe that this is not the case because, due to the calculated reactions time, it is expected that this will only change the distribution of the main peak, modifying the mobility measured for the cluster, which will be closer to the CO_2^+ mobility.

Since to our knowledge there is no other product possible to be formed, we believe that this second peak is most likely due to impurities, such as H_2O^+, that result from outgassing processes inside the detector. To prove this theory, we performed a signal degradation study, to observe how the signal would be shaped over time. This study is shown in figure 3.6. It is possible to notice a decrease in the amplitude of the main peak and an increase in fastest peak, in agreement with the presence of impurities. As

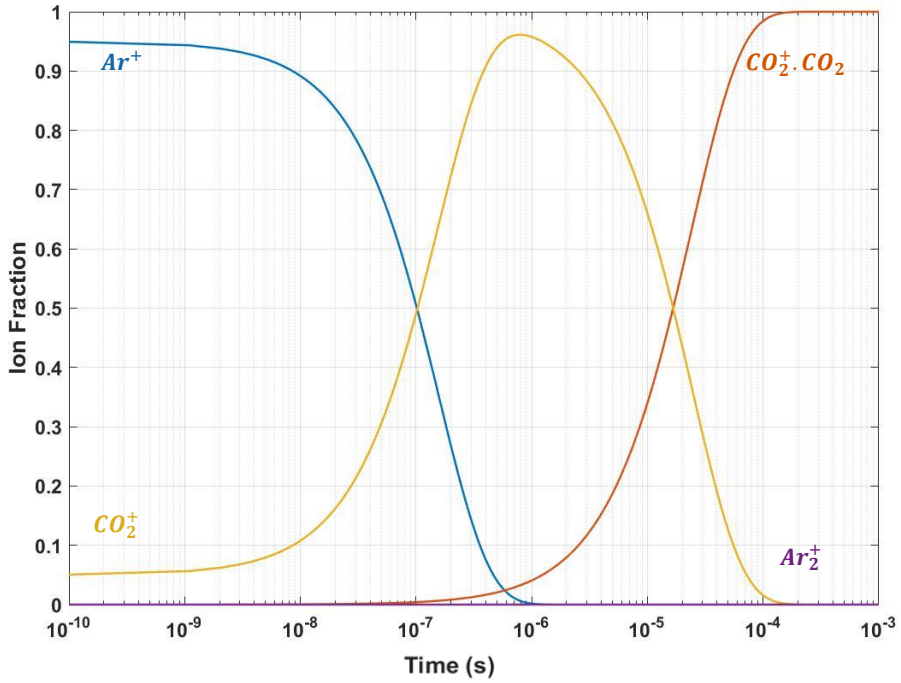

Figure 3.5: Ion abundance with time for a mixture of 95% Ar and 5% CO_2 at a pressure of 8 Torr

it can be seen in figure 3.7, in the light of the mobilities present in the literature it is possible that this peak corresponds to the presence of H_2O^+.

Additionally, in the time-of-arrival spectra of figure 3.4 there is a shift of the peaks towards the origin, i.e., an increment of the mobility of the ions when the concentration of CO_2 decreases, as can also be confirmed in figure 3.7. This can be due to an increasing availability of Ar, that not only decreases the probability of collision between $CO_2{}^+$ and CO_2 gas molecules, leading to a significant increase in the formation time of $CO_2^+.(CO_2)$, but also, as can be observed in figure 3.4, as Ar concentration increases, there is an increase in the peak amplitude, suggesting that the charge transfer process between Ar^+ and CO_2 (see equation 3.1) favours the formation of CO_2^+, as referred previously. Nevertheless, for an Ar concentration above 85%, we observed a slight decrease in the peak amplitude that was attributed to a decreasing availability of CO_2, considering that the peak resolution remains the same.

In figure 3.7 we plot the reduced mobility of the ions produced in the Ar-CO_2 mixture for different mixture ratios, for a pressure of 8 Torr and for E/N of 20 Td at room temperature. In this plot there are several points to stress out. Firstly our experimental data it represented in black (this data is also shown in table 3.5); secondly, for pure Ar (0% of CO_2) 4 points are shown, a blue one that corresponds to the mobility of CO_2^+

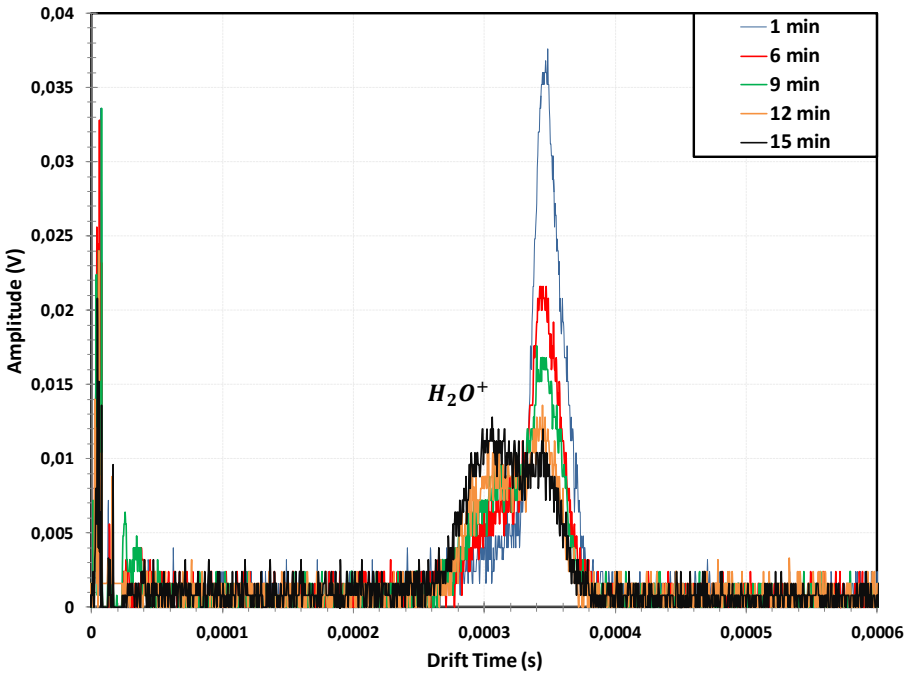

Figure 3.6: Signal degradation study to time-of-arrival spectra for Ar-CO_2 mixtures at a pressure of 10 Torr, temperature of 298 K and for a reduced electric field of 20 Td with a voltage across the GEM of 25 V. The ion responsible for the second peak appearing in this time-of-arrival spectra is probably H_2O^+ .

in Ar obtained by W. Lindinger [77], a red one, which corresponds to the mobility of H_2O^+ in Ar determined by H. Bohringer [78] in 1983 and finally two points, an orange one and a purple one, that match to the mobilities of the atomic and dimer ions of Ar in pure Ar measured by E. C. Beaty [79]. To our knowledge the $CO_2^+.(CO_2)$ has not yet been measured in Ar. G. Schultz *et al* [72] finally measured the reduced mobility of ions in several mixtures of Ar-CO_2. However their results were not taken into account since their experimental work was conducted at atmospheric pressure, and because of this, the formation of single clusters takes only a few ns, which is far faster than that of the total ions drift time, allowing them to grow into clusters with higher masses. Although the authors did not identify the ions measured, their mobilities are much slower than ours indicating that they possibly measured the mobility of large clusters. Thirdly, for 100% of CO_2, there are 3 points plotted. The yellow one corresponds to our experimental value obtained in pure CO_2 for a E/N of 20 Td and a pressure of 8 Torr. The other two points, the grey and the green, match the mobilities of $CO_2^+.(CO_2)$ and CO_2^+ ions. These values were taken from the review article of Y. Kalkan in 2015 [16] and are the result of the arithmetic average of the values of various studies present

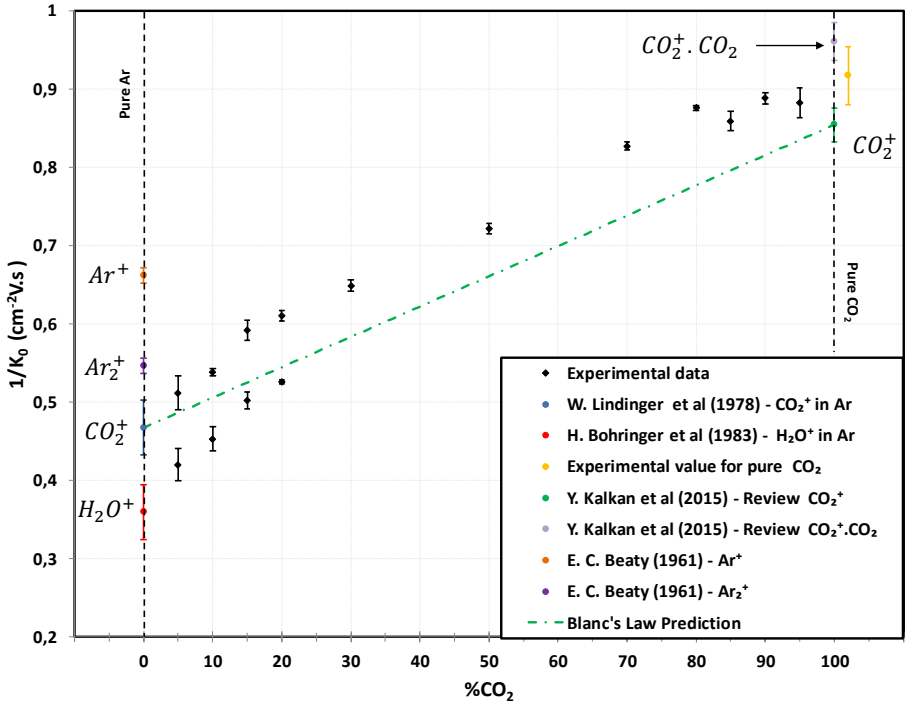

Figure 3.7: Reduced mobility of the ions produced in the Ar-CO_2 mixtures for a pressure range of 8 Torr and for a E/N of 20 Td at room temperature.

in the literature, some of those were extrapolated to 20 Td. Finally, the green dotted line represents Blanc's law result for the ion already measured in Ar, CO_2^+. As can be observed the values predicted by Blanc's law are not in good agreement with the experimental ones. In fact, the experimental values measured are slower than the Blanc's law prediction which also indicates that we are in the presence of $CO_2^+.(CO_2)$. Yet it is possible to notice that for lower concentrations of CO_2 the experimental values seem to be more towards to the dotted line, in the agreement with the hypothesis that a considerable part of the drift distance is travelled as CO_2^+, as already proposed in the reaction paths.

All things considered, it is possible to state that for an E/N value of 20 Td and a pressure of 8 Torr the ion formed in mixtures of Ar-CO_2 for almost all concentrations of CO_2 will be $CO_2^+.(CO_2)$, although CO_2^+ would be the ion expected in an atmosphere close to 100% of Ar (at 8 Torr), because the cluster would not have time to be formed. Adjusting a regression line to the data we obtain a mobility in Ar of 1.95 ± 0.02 $cm^2V^{-1}s^{-1}$ which corresponds to 9% variation relative to the value for CO_2^+ obtained by W. Lindinger [80].

It is important to mention that in the range of pressures used (8-10 Torr) no significant dependence of the mobility with total gas pressure was observed, and regarding

Table 3.5: Mobility of the ions observed for the Ar-CO_2 mixture ratios of 5%, 10%, 15%, 20%, 30%, 50%, 70%, 80%, 85%, 90% and 95% of CO_2, obtained for different E/N and a pressure of 8 Torr at room temperature (298 K) and a voltage across the GEM of 25V.

Mixture	**Mobility ($cm^2V^{-1}s^{-1}$)**		**Ion**
	20 Td	**25 Td**	
5% CO_2 - 95% Ar	$1.95^{+}_{-}0.05$	$1.93^{+}_{-}0.01$	$CO_2^+.CO_2$
	$2.38^{+}_{-}0.05$	$2.38^{+}_{-}0.02$	H_2O^+
10% CO_2 - 90% Ar	$1.85^{+}_{-}0.009$	$1.85^{+}_{-}0.01$	$CO_2^+.CO_2$
	$2.21^{+}_{-}0.03$	$2.21^{+}_{-}0.04$	H_2O^+
15% CO_2 - 85% Ar	$1.69^{+}_{-}0.02$	$1.70^{+}_{-}0.02$	$CO_2^+.CO_2$
	$1.99^{+}_{-}0.02$	$2.00^{+}_{-}0.03$	H_2O^+
20% CO_2 - 80% Ar	$1.64^{+}_{-}0.01$	$1.60^{+}_{-}0.02$	$CO_2^+.CO_2$
	$1.900^{+}_{-}0.005$	$1.85^{+}_{-}0.02$	H_2O^+
30% CO_2 - 70% Ar	$1.54^{+}_{-}0.01$	$1.54^{+}_{-}0.01$	$CO_2^+.CO_2$
50% CO_2 - 50% Ar	$1.385^{+}_{-}0.009$	$1.372^{+}_{-}0.007$	$CO_2^+.CO_2$
70% CO_2 - 30% Ar	$1.209^{+}_{-}0.006$	$1.200^{+}_{-}0.008$	$CO_2^+.CO_2$
80% CO_2 - 20% Ar	$1.141^{+}_{-}0.004$	$1.131^{+}_{-}0.004$	$CO_2^+.CO_2$
85% CO_2 - 15% Ar	$1.16^{+}_{-}0.01$	$1.15^{+}_{-}0.01$	$CO_2^+.CO_2$
90% CO_2 - 10% Ar	$1.125^{+}_{-}0.008$	$1.12^{+}_{-}0.01$	$CO_2^+.CO_2$
95% CO_2 - 5% Ar	$1.13^{+}_{-}0.02$	$1.12^{+}_{-}0.02$	$CO_2^+.CO_2$

the behaviour of the mobility with E/N (from 20 to 25 Td), it was verified a slight dependence with lower mobility for higher E/N as can be observed in table 3.5.

3.2.3 Ne-CO_2

In neon-carbon dioxide (Ne-CO_2) mixtures with CO_2 concentrations higher than 25% only one peak is observed, as seen in figure 3.8. The ion responsible for this peak is the same ion as in pure CO_2.

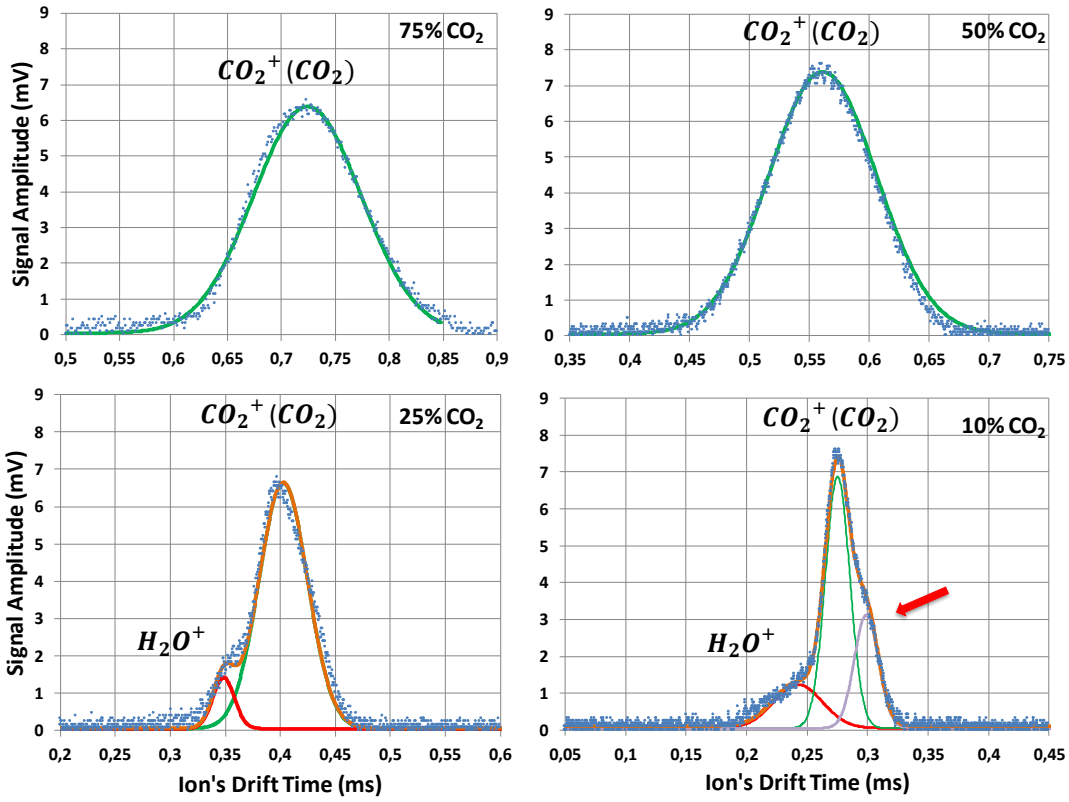

Figure 3.8: Time-of-arrival spectra averaged over 128 pulses for several Ne-CO_2 mixtures (10%, 25%, 50%, 75% of CO_2) at a pressure of 8 Torr, temperature of 298 K and for a reduced electric field of 15 Td with a voltage across the GEM of 25 V (background noise was already subtracted).

Since the total ionization cross section for electron impact (for an energy of 25 eV) in Ne is 0.036×10^{-16} cm^2 [81], much lower than the total cross section of CO_2 (1.18×10^{-16} cm^2 [76]), it is expected that even at low CO_2 concentrations, CO_2 ions are still the ones that are preferentially produced. Additionally, with the increasing availability of Ne in the mixture, Ne^+ ions will be produced more abundantly, and according to the rate constants available, they are more likely to react with CO_2 (equation 3.3) ($k = 0.06\pm0.1\times10^{-9}$cm^{3}s^{-1} [67]), than with Ne via reaction 3.5 ($k = 5.6\times10^{-32}$cm^{6}s^{-1}

[24]) since the reaction time of the latter is higher than any other reaction channel in the pressure conditions used in this experiment. So, in the these conditions the presence of Ne ions will lead to the formation of the same ions as seen in pure CO_2, but through a different reaction channel, first producing CO^+ (equation 3.3) which will further react with CO_2 via reaction 3.4 (k=1.1×10^{-9}cm^{3}s^{-1} [67]) leading to the formation of CO_2^+:

$$Ne^+ + CO_2 \rightarrow CO^+ + \frac{1}{2}O_2 + Ne \tag{3.3}$$

$$CO^+ + CO_2 \rightarrow CO_2^+ + CO \tag{3.4}$$

$$Ne^+ + 2Ne \rightarrow Ne_2^+ + Ne \tag{3.5}$$

In figure 3.8 the time-of-arrival spectra for several Ne-CO_2 mixtures (10%, 25%, 50% and 75% of CO_2) at a pressure of 8 Torr, temperature of 298 K and for a reduced electric field of 15 Td with a voltage across the GEM of 25 V are displayed.

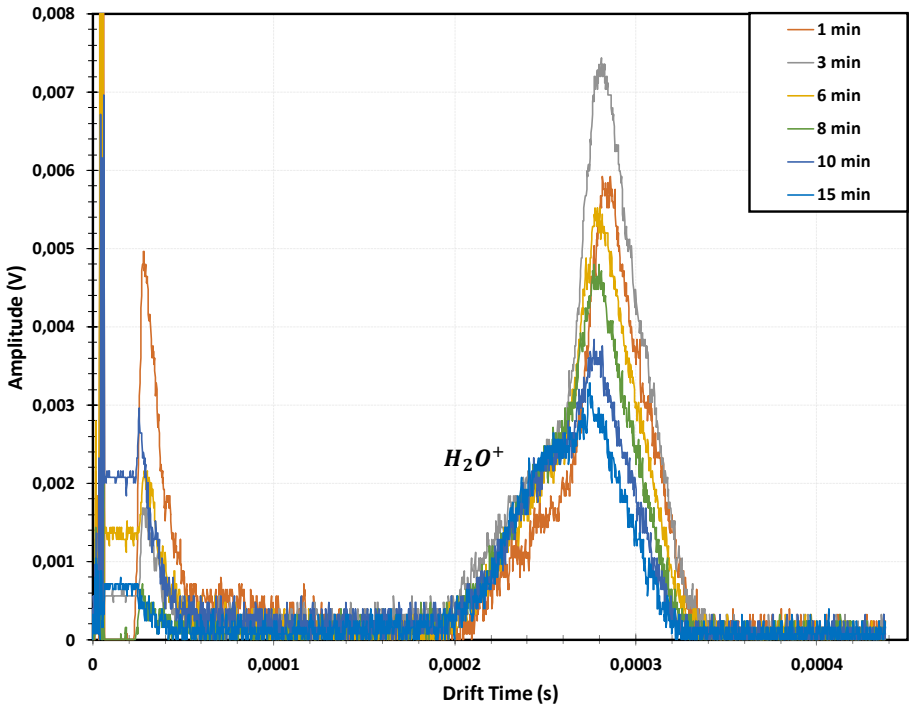

Figure 3.9: Signal degradation study of a time-of-arrival spectra for a mixture of 90% Ne and 10% CO_2 at a pressure of 8 Torr, temperature of 298 K and for a reduced electric field of 15 Td with a voltage across the GEM of 25 V. The ion responsible for the fastest peak is probably H_2O^+ .

Apart from the peak area, that varies with CO_2 concentration in the mixture, which is clearly related to the availability of CO_2, a peak shift to lower drift times with decreasing concentration of CO_2 was also observed. This shift translates into an increase

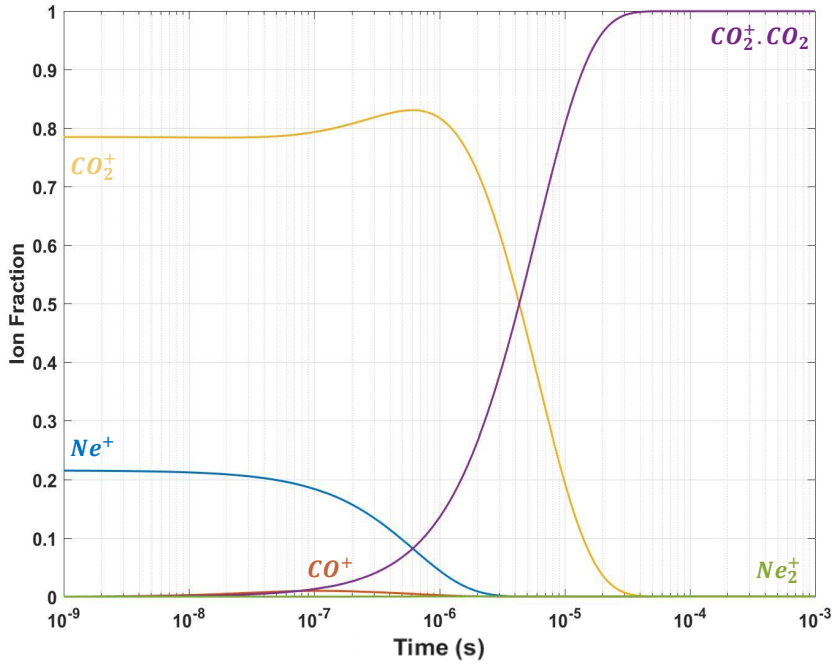

Figure 3.10: Ion abundance with time for a mixture of 90% Ne and 10% CO_2 at a pressure of 8 Torr.

in the ion mobility, and can be caused by two effects: the decreasing availability of CO_2 that will decrease the probability of collision between $CO_2{}^+$ and CO_2 gas molecules, resulting in less resonant charge transfer reactions; and the fact that Ne has a much smaller mass than CO_2 ion species, implying much smaller energy loss.

Besides the decrease in the peak area with the decreasing concentration of CO_2 in the mixture, for CO_2 concentrations below 25% a small bump starts to show up on the left side of the main peak. The possibility of this peak corresponding to O^+ was discarded by lowering the GEM voltage below the ionization energy for this ion formation (19 eV) and observing that the small bump remained visible, for CO_2 concentrations lower than 25%. We attributed this second peak to the presence of water, that result from outgassing processes inside the detector which had already been observed in other mixtures, such as Ar-CO_2 (section 3.2.2). As already done with the previous mixture, we performed a signal degradation study that is shown in figure 3.9. As before it is possible to notice a decrease in the amplitude of the main peak and an increase in fastest peak, supporting the idea of impurities.

For CO_2 concentrations below 10% yet another peak starts to appear. Since there are lack of reaction paths that originate new ions, we were not able to identify the origin of this bump.

Figure 3.10 shows the reaction times of the reactions that take place in a mixture of 90% Ne and 10% CO_2 for a pressure of 8 Torr. A critical analysis of the figure shows that it is required approximately 45 μs to convert 99.9% of the ions into $CO_2^+.(CO_2)$ This reaction time should decrease for higher quantities of CO_2 in the mixture. The transit time of the experimental measurements for an E/N of 15 Td extends between 275 μs and 870 μs at 10% CO_2 and 99% CO_2, respectively. According to this, for a mixture of 90% Ne and 10% CO_2, a maximum 20% of the drift distance is travelled as CO_2^+, influencing the mobility measured for the cluster.

Regarding the formation of Ne dimer (reaction 3.5), comparatively to what happened for Ar, it is unlikely to occur because, at low pressure, Ne^+ preferably transfer its charge to CO_2^+ rather than for Ne.

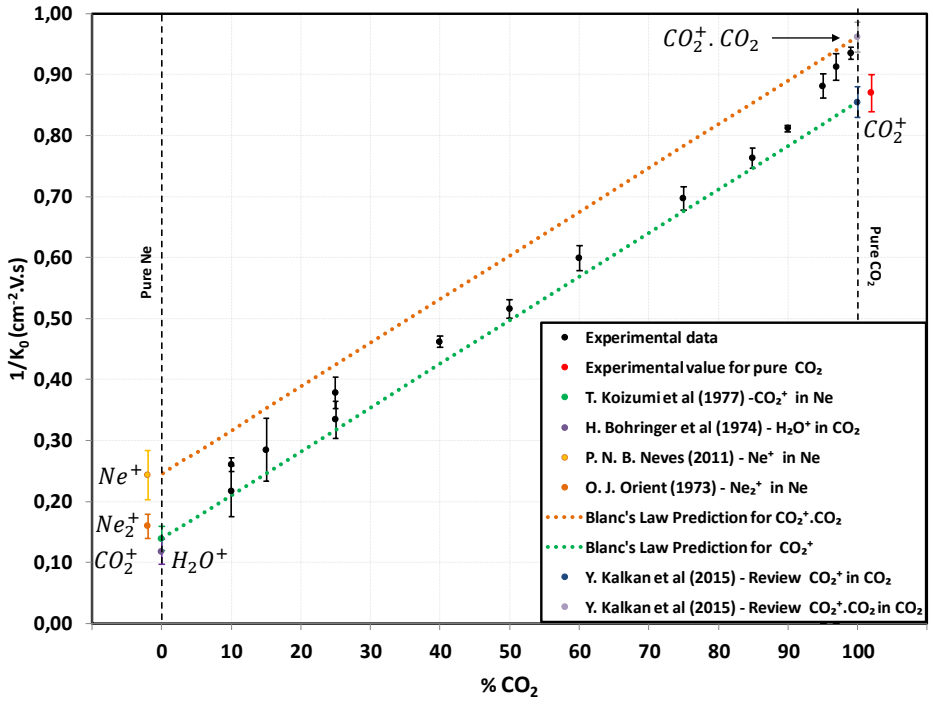

Figure 3.11: Reduced mobility of the ions produced in the Ne-CO_2 mixtures for a pressure of 8 Torr and for an E/N of 15 Td at room temperature.

In figure 3.11 we plot the inverse of the reduced mobility of the ions produced in the Ne-CO_2 mixture as a function of the different mixture ratios studied for a pressure range of 8 Torr and for E/N=15 Td, at room temperature (298 K). There are a few key aspects that are important to highlight in order to better understand this plot.

As in previous sections, our experimental data for Ne-CO_2 are in black and are also shown in table 3.6; regarding the pure Ne line (0% of CO_2) 4 points are shown, a green one that represents the mobility of CO_2^+ in Ne, obtained by T. Koizumi *et al*

in 1977 [82], a red one, which corresponds to the mobility of H_2O^+ in Ne determined by H. Bohringer [78] in 1983 and finally two points, a yellow one and an orange one, that match to the mobilities of the atomic and dimer ions of Ne in pure Ne measured by P.N.B. Neves [24] in the Ne^+ case and by O. J. Orient [83] in the Ne_2^+ case. To our knowledge the $CO_2^+.(CO_2)$ has not yet been measured in Ne. Similarly to the case of Ar-CO_2 the plot shows 2 points in the line corresponding to 100% of CO_2. These two points, the grey and the blue, match to the mobilities of $CO_2^+.(CO_2)$ and CO_2^+ ions and as before, were taken from Y. Kalkan [16].

As mentioned, Blanc's law is used to predict the mobility of the ions in gaseous mixtures. Dotted lines representing Blanc's law for the most probable candidate ions, namely CO_2^+ and $CO_2^+(CO_2)$, are also displayed in order to try to identify the origin of the main peak. The K_{0g1} and K_{0g2} used for the representation of Blanc's law (1.8) were taken from [9] for CO_2^+ in Ne while for $CO_2^+.(CO_2)$ in Ne it was calculated using Langevin's formula (see Equation 1.3). In the case of CO_2^+ in CO_2 and $CO_2^+.(CO_2)$ in CO_2 they represent the average value of different experiments present in [16].

Looking at figure 3.11 it is possible to observe that the ion mobility experimentally obtained stays between the two lines, with the ion detected being slower than the literature values for the CO_2^+ but faster that the prediction for $CO_2^+(CO_2)$ ion. Another aspect that can be noticed is the approaching of the experimental values to the Blanc's law prediction in the case of the cluster, for greater concentrations of CO_2 in the mixture. Under these circumstances, the cluster formation is faster and the time spent as cluster is longer so the CO_2^+ contribution is less important. In contrast, for lower concentrations of CO_2, the experimental data slightly deviates towards the CO_2^+ line. According to these data and the reaction times calculated, we can infer that the final ion detected is $CO_2^+(CO_2)$ for most of the mixtures of Ne-CO_2, however, the mobility of the main peak is affected by the presence CO_2^+ ion, because part of the drift distance that is travelled as CO_2^+ is not negligible.

Due to the high uncertainty on the determination of the centroid of the small bump on the right side of the main one, this one was discarded and its mobility value is not displayed in table 3.6.

From 0 to 100% of CO_2, the peaks observed were seen to vary in position and area, demonstrating that the ion or ions formed and their mobilities depend on the ratio of the two gases used. The mobility values of the ions observed for the Ne-CO_2 mixture for all concentrations studied, at E/N in the range of 10 to 20 Td, pressure of 8 Torr and at room temperature (298 K) are summarized in table 3.6. Also in the same table, a small dependence of the mobility with E/N (from 10 to 20 Td) can be observed .

Table 3.6: Mobility of the ions observed in Ne-CO_2 mixture for different ratios of CO_2, obtained for different E/N and a pressure of 8 Torr at room temperature. *For 5% CO_2 - 95% Ne mixture at E/N of 15-20 Td discharges occurred in experimental system and for this reason mobility values could not be determined.

Mixture	**Mobility ($cm^2V^{-1}s^{-1}$)**			**Ion**
	10 Td	**15 Td**	**20 Td**	
5% CO_2 - 95% Ne	$4.47^{+}_{-}0.03$	*	*	$CO_2^+.CO_2$
	$5.36^{+}_{-}0.15$			H_2O^+
10% CO_2 - 90% Ne	$3.96^{+}_{-}0.01$	$3.85^{+}_{-}0.04$	$3.81^{+}_{-}0.01$	$CO_2^+.CO_2$
	$4.69^{+}_{-}0.04$	$4.61^{+}_{-}0.19$	$4.77^{+}_{-}0.46$	H_2O^+
15% CO_2 - 85% Ne	$3.59^{+}_{-}0.10$	$3.51^{+}_{-}0.18$	$3.59^{+}_{-}0.13$	$CO_2^+.CO_2$
	-	-	$3.17^{+}_{-}0.02$	-
25% CO_2 - 75% Ne	$2.73^{+}_{-}0.02$	$2.65^{+}_{-}0.07$	$2.65^{+}_{-}0.02$	$CO_2^+.CO_2$
	-	$3.00^{+}_{-}0.09$	$2.98^{+}_{-}0.07$	H_2O^+
40% CO_2 - 60% Ne	$2.15^{+}_{-}0.01$	$2.17^{+}_{-}0.03$	-	$CO_2^+.CO_2$
50% CO_2 - 50% Ne	$2.03^{+}_{-}0.01$	$1.94^{+}_{-}0.03$	$1.90^{+}_{-}0.01$	$CO_2^+.CO_2$
60% CO_2 - 40% Ne	$1.72^{+}_{-}0.01$	$1.67^{+}_{-}0.03$	-	$CO_2^+.CO_2$
75% CO_2 - 25% Ne	$1.49^{+}_{-}0.03$	$1.43^{+}_{-}0.03$	$1.42^{+}_{-}0.02$	$CO_2^+.CO_2$
85% CO_2 - 15% Ne	$1.32^{+}_{-}0.02$	$1.31^{+}_{-}0.02$	$1.29^{+}_{-}0.03$	$CO_2^+.CO_2$
90% CO_2 - 10% Ne	$1.27^{+}_{-}0.01$	$1.23^{+}_{-}0.01$	$1.21^{+}_{-}0.01$	$CO_2^+.CO_2$
95% CO_2 - 5% Ne	$1.15^{+}_{-}0.03$	$1.13^{+}_{-}0.03$	$1.13^{+}_{-}0.01$	$CO_2^+.CO_2$
97% CO_2 - 3% Ne	$1.10^{+}_{-}0.01$	$1.10^{+}_{-}0.02$	$1.10^{+}_{-}0.01$	$CO_2^+.CO_2$
99% CO_2 - 1% Ne	$1.08^{+}_{-}0.02$	$1.07^{+}_{-}0.01$	$1.06^{+}_{-}0.01$	$CO_2^+.CO_2$

3.2.4 N_2-CO_2

In nitrogen-carbon dioxide (N_2-CO_2) mixtures, only one peak was observed for CO_2 concentrations ranging from 10% to 100%, while below 10% a second peak starts to emerge from the first one, as can be seen in figure 3.12. In this case the ion responsible for the main peak observed is the ion produced in Ar-CO_2 and Ne-CO_2 mixtures - $CO_2^+.(CO_2)$, while the second peak is attributed to N_4^+.

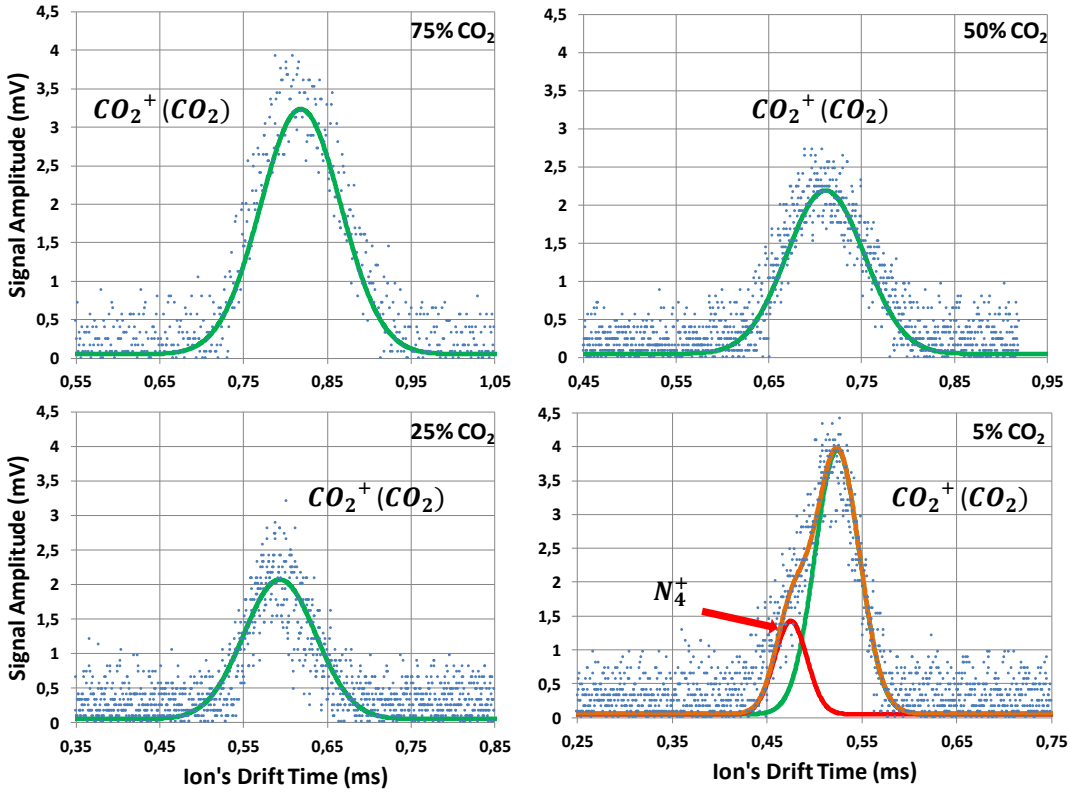

Figure 3.12: Time-of-arrival spectra averaged over 128 pulses for several N_2-CO_2 mixtures (10%, 25%, 50%, 75% of CO_2) at a pressure of 8 Torr, temperature of 298 K and for a reduced electric field of 15 Td with a voltage across the GEM of 25 V (background noise was already subtracted).

In this case, the total electron impact ionization cross section of N_2 for 25 eV is 0.64×10^{-16} cm^2 [84], lower than the total CO_2 ionization cross section (1.18×10^{-16} cm^2 [66]). It is thus expected that even at higher N_2 concentrations, CO_2 ions are the ones preferentially produced. With increasing availability of N_2 in the mixture, N_2^+ ions will be produced more abundantly, and according to the rate constants available, they are more likely to transfer the charge to CO_2 through reaction (3.6) ($k = 0.55\times10^{-9}$cm^{3}s^{-1}), than by reacting with N_2 via the three-body reaction 3.7 ($k = 5\times10^{-29}$cm^{6}s^{-1}) for which the reaction time is higher. As a result, in the N_2-CO_2 mixtures, N_2 ions will lead to the

formation of the same CO_2 ion as in pure CO_2, originating CO_2^+ through the following reaction:

$$N_2^+ + CO_2 \rightarrow CO_2^+ + N_2 \tag{3.6}$$

$$N_2^+ + 2N_2 \leftrightharpoons N_4^+ + N_2 \tag{3.7}$$

Figure 3.13 displays the concentration evolution of the ions species that are produced in a mixture of 95% N_2 and 5% CO_2 for a pressure of 8 Torr. In this figure it is possible to observe that is required approximately 170 μs to convert 72.5% of all ions into $CO_2^+.(CO_2)$, and the competing reaction that converts N_2^+ into N_4^+ only takes 0.66 μs. The total amount of this last ion in the mixture represents 27.5% of ions produced. According to W. Lindinger [80], the N_4^+ ion will eventually transfer the charge to CO_2 (equation 3.8).

$$N_4^+ + CO_2 \rightarrow CO_2^+ + 2N_2 \tag{3.8}$$

but, this reaction channel was discarded due to high uncertainty of the reaction rate and also because, to the best of our knowledge, this reaction has not been reported by other authors.

So, the main ion is $CO_2^+.(CO_2)$, although for greater concentrations of N_2, N_4^+can also appear The transit time of the experimental measurements for an E/N of 15 Td extends between 440 μs and $\approx$1 ms (1% to 99% CO_2, respectively). Also, as in previous mixtures, the mobility of the cluster is probably affected by the mobility of CO_2^+ ion in part of the drift path.

In figure 3.14 we plot the inverse of the reduced mobility of the ions produced in the N_2- CO_2 mixture as a function of the different mixture ratios studied for a pressure of 8 Torr and for an E/N of 15 Td, at room temperature (298 K). The points in black are our experimental data for N_2-CO_2 at the experimental conditions already mentioned. These results are also shown in table 3.6; two points can be found in the pure N_2 line (0% of CO_2), a red one, that corresponds to the mobility of CO_2^+ in N_2 that was determined by I. Dotan *et al* in 1976 [85] and a yellow one, which represents the mobility of N_4^+ in N_2 that is an average value obtained from a few values reported in the literature. The values used are shown in section 3.3.1, where the results of pure nitrogen are explained (table 3.10). To our knowledge, $CO_2^+.(CO_2)$ has not yet been measured in N_2. As in the previous mixtures it is show in figure 3.14 for pure CO_2, the mobilities values for $CO_2^+.(CO_2)$ and CO_2^+ ions that were also taken from Y. Kalkan [16].

Comparatively to the case of Ne-CO_2, Blanc's law was also used to predict the most probable candidate ions for the main peak. Dotted lines, green and orange, represent Blanc's law for CO_2^+ and $CO_2^+(CO_2)$. The K_{0g1} used for the representation Blanc's law (1.8) was taken from [9] for CO_2^+ in N_2 while for $CO_2^+.(CO_2)$ in N_2 it was obtained using

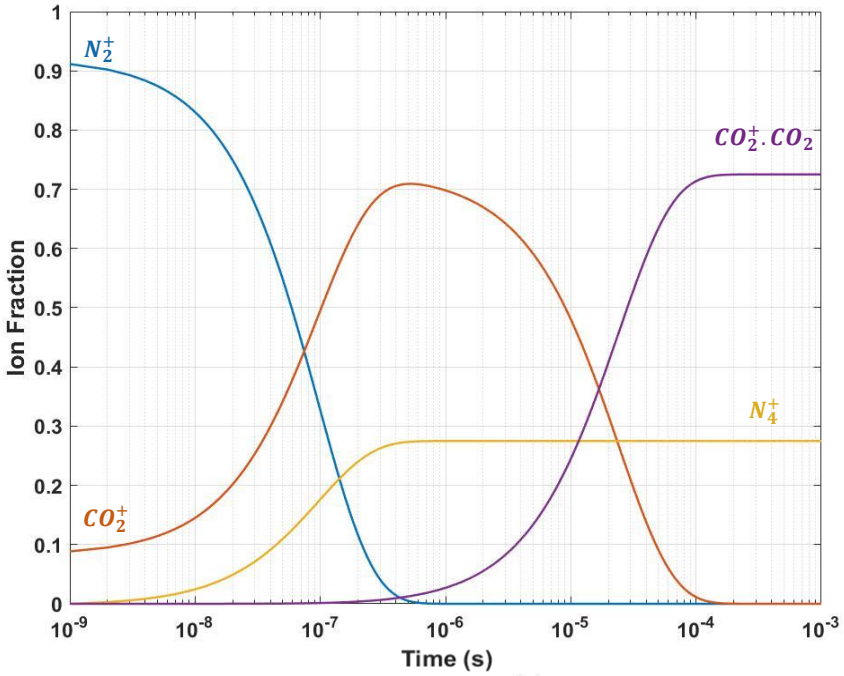

Figure 3.13: Ion abundance with time for a mixture of 95% N_2 and 5% CO_2 at a pressure of 8 Torr and energies of 25 eV.

Langevin's formula (Equation 1.3). In the case of CO_2^+ in CO_2 and $CO_2^+.(CO_2)$ in CO_2 an average value obtained from different experiments present in [16], was used.

Observing figure 3.14 it is possible to confirm that the ion mobility experimentally obtained stays within Blanc's law predictions for CO_2^+ and $CO_2^+.(CO_2)$ throughout the entire mixture range.

In addition, it is possible to see that the experimental mobility values for the main ion, deviate slightly towards the CO_2^+ theoretical line for lower CO_2 concentrations in the mixture, since with lower availability of CO_2, the distance travelled as CO_2^+ will be larger and will have a greater influence on the mobility of $CO_2^+.(CO_2)$, approaching the one reported for CO_2^+ in literature [85].

Regarding the identification of the second peak, due to the known reaction paths we believe that N_4^+ is present at 8 Torr and for low concentrations of CO_2. With this in mind, a regression to the experimental points of the second peak was performed, obtaining a mobility value of 2.27 $cm^2V^{-1}s^{-1}$ for N_4^+ in N_2. This value deviates 2.5% from those reported in literature.

From 0 to 100% of CO_2 the peaks observed were seen to vary, demonstrating that the ion mobility in the mixture depends on the ratio of the two gases. The mobility values of the peaks observed for the N_2-CO_2 mixture ratios studied, for E/N from 10 to

Table 3.7: Mobility of the ions observed in N_2-CO_2 mixture for different ratios of CO_2, obtained for different E/N and a pressure of 8 Torr at room temperature.

Mixture	**Mobility ($cm^2V^{-1}s^{-1}$)**			**Ion**
	15 Td	**20 Td**	**25 Td**	
1% CO_2 - 99% N_2	$2.11^{+}_{-}0.04$	$1.99^{+}_{-}0.01$	$1.98^{+}_{-}0.01$	$CO_2^+.CO_2$
	$2.26^{+}_{-}0.02$	$2.16^{+}_{-}0.03$	$2.13^{+}_{-}0.01$	N_4^+
3% CO_2 - 97% N_2	$2.03^{+}_{-}0.03$	$1.96^{+}_{-}0.01$	$1.97^{+}_{-}0.04$	$CO_2^+.CO_2$
	$2.14^{+}_{-}0.02$	$2.12^{+}_{-}0.01$	$2.12^{+}_{-}0.03$	N_4^+
5% CO_2 - 95% N_2	$1.92^{+}_{-}0.01$	$1.92^{+}_{-}0.01$	$1.93^{+}_{-}0.01$	$CO_2^+.CO_2$
	$2.08^{+}_{-}0.02$	$2.07^{+}_{-}0.03$	$2.11^{+}_{-}0.08$	N_4^+
10% CO_2 - 90% N_2	$1.85^{+}_{-}0.04$	$1.87^{+}_{-}0.04$	$1.83^{+}_{-}0.02$	$CO_2^+.CO_2$
	$1.95^{+}_{-}0.02$	$1.98^{+}_{-}0.02$	$1.95^{+}_{-}0.02$	N_4^+
15% CO_2 - 85% N_2	$1.83^{+}_{-}0.03$	$1.80^{+}_{-}0.02$	$1.78^{+}_{-}0.03$	$CO_2^+.CO_2$
	-	-	$1.90^{+}_{-}0.03$	CO_2^+
25% CO_2 - 75% N_2	$1.71^{+}_{-}0.03$	$1.68^{+}_{-}0.02$	$1.66^{+}_{-}0.03$	$CO_2^+.CO_2$
40% CO_2 - 60% N_2	$1.51^{+}_{-}0.03$	$1.49^{+}_{-}0.02$	$1.49^{+}_{-}0.03$	$CO_2^+.CO_2$
50% CO_2 - 50% N_2	$1.43^{+}_{-}0.03$	$1.40^{+}_{-}0.02$	$1.39^{+}_{-}0.02$	$CO_2^+.CO_2$
60% CO_2 - 40% N_2	$1.37^{+}_{-}0.02$	$1.35^{+}_{-}0.01$	$1.33^{+}_{-}0.02$	$CO_2^+.CO_2$
75% CO_2 - 25% N_2	$1.26^{+}_{-}0.03$	$1.26^{+}_{-}0.04$	$1.24^{+}_{-}0.02$	$CO_2^+.CO_2$
85% CO_2 - 15% N_2	$1.19^{+}_{-}0.04$	$1.17^{+}_{-}0.02$	$1.16^{+}_{-}0.03$	$CO_2^+.CO_2$
90% CO_2 - 10% N_2	$1.17^{+}_{-}0.03$	$1.16^{+}_{-}0.02$	$1.14^{+}_{-}0.03$	$CO_2^+.CO_2$
95% CO_2 - 5% N_2	$1.14^{+}_{-}0.04$	$1.11^{+}_{-}0.03$	$1.10^{+}_{-}0.03$	$CO_2^+.CO_2$
97% CO_2 - 3% N_2	$1.12^{+}_{-}0.03$	$1.14^{+}_{-}0.05$	$1.10^{+}_{-}0.03$	$CO_2^+.CO_2$
99% CO_2 - 1% N_2	$1.10^{+}_{-}0.03$	$1.10^{+}_{-}0.02$	$1.08^{+}_{-}0.03$	$CO_2^+.CO_2$

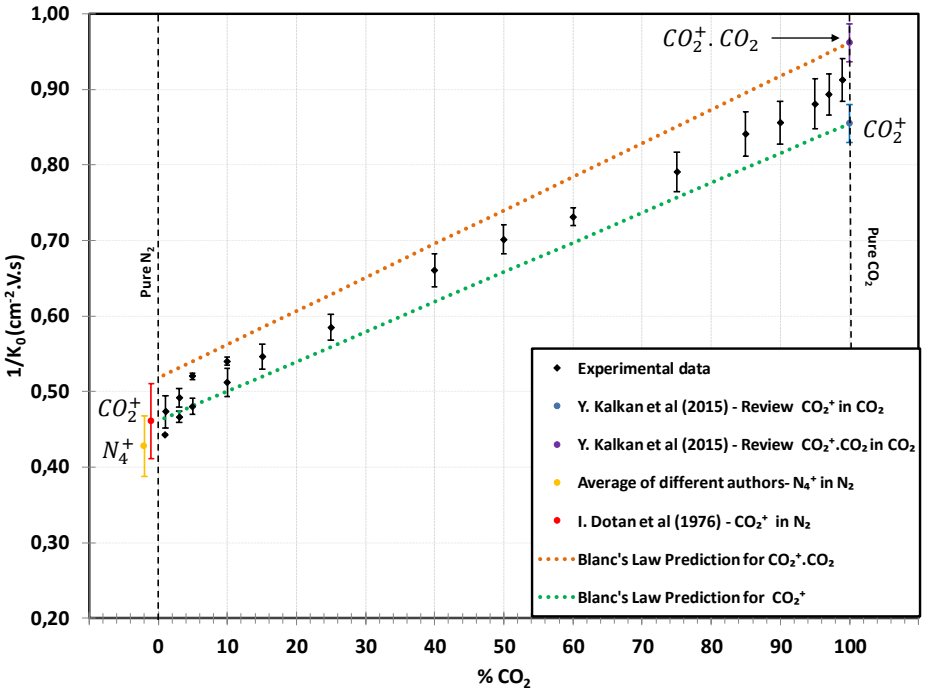

Figure 3.14: Reduced mobility of the ions produced in the N_2-CO_2 mixtures for a pressure of 8 Torr and for an E/N of 15 Td at room temperature.

20 Td, at a pressure of 8 Torr and at room temperature (298 K) are summarized in table 3.7. Identically to the last mixtures, a similar dependence of the mobility with E/N was observed in the range of 15-25 Td. No significantly mobility value dependence on the range of pressures (4 to 16 Torr) studied was verified.

3.3 N_2 Mixtures

3.3.1 Pure N_2

Molecular nitrogen is the most abundant constituent in our planet atmosphere and electron collisions with N_2 molecules play a fundamental role in the upper atmosphere of the Earth. In the field of gas filled radiation detectors, nitrogen is known as a common contaminant in noble gas medium degrading the detection capabilities of the detectors. From the ions formation point of view its behaviour is not well known [25]. However, it is considered a useful buffer, because of its large ionization potential, 15.6 eV, and its high dissociation energy, making it relatively inert with many atoms and molecules [84].

In 2012 A.N.C. Garcia *et al* [25] reported results for pure nitrogen carried out in

the same experimental system that was used in this project. Measurements were performed in N_2 for different reduced electric fields (from 15 to 35 Td) and for different pressures (in the 6 – 16 Torr range). According to the literature, at their working conditions it is expected the presence of only one peak, N_4^+, as was confirmed by their experimental results, although it is perceivable the presence of impurities at the right side of the main peak.

According to the authors the experimental results obtained are in very good agreement with the ones obtained by J. T. Moseley *et al* [7] and M. Saporoschenko [86] that used different techniques (total variation of 1.7%).

Regarding our mobility results for pure nitrogen (N_2), we measured the mobilities of the ions formed in this gas for different reduced electric fields E/N (from 10 Td up to 60 Td), for a pressure range between the 6 to 10 Torr range at room temperature (298 K) and for voltages across the GEM between 25 to 32 V. In several time-of-arrival spectra two peaks were observed. An example of a time-of-arrival spectrum is displayed in figure 3.15. In this particular case the experiment was conducted at 8 Torr, at a reduced electric field of 15 Td, and for a voltage across the GEM, V_{GEM}, of 30 V.

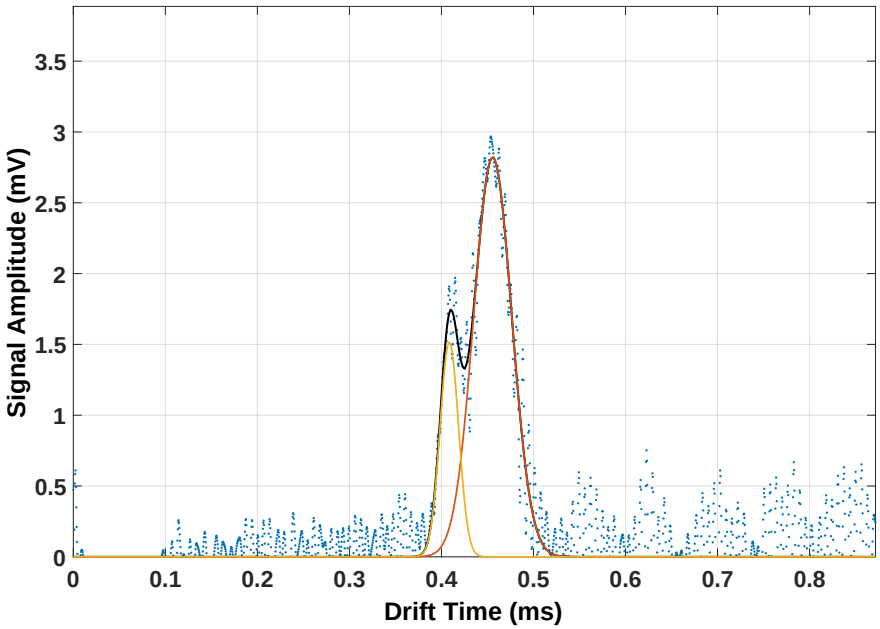

Figure 3.15: Time-of-arrival spectrum of an average of 128 pulses for pure N_2 at a pressure of 8 Torr, and for E/N=15 Td, V_{GEM}=30 V, at room temperature.

The resulting mobilities were determined according to the method already described and were plotted against the reduced electric field, E/N, and an extrapolation was then carried out in order determine the reduced mobilities of these ions when E/N

$\rightarrow$0 - see figure 3.16. Under these circumstances, we obtained an extrapolated mobility value of 2.79 $cm^2\ V^{-1}\ s^{-1}$ for the fastest peak and 2.34 $cm^2\ V^{-1}\ s^{-1}$ for the slowest one.

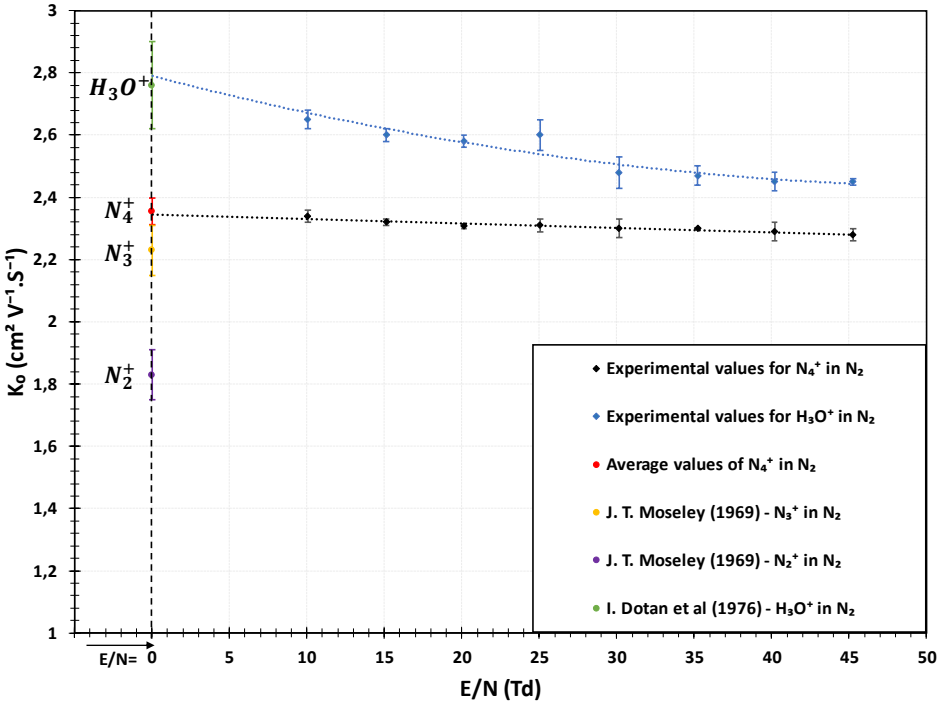

Figure 3.16: Reduced mobility of the ions produced in N_2 for a pressure of 8 Torr and for E/N values in the 10-45 Td range.

This time we used higher voltages in the GEM than usual, thus increasing the variety of primary ions produced in the GEM holes. For a V_{GEM} of typically 30 V, the photoelectrons can gain a maximum energy of 31 eV, since the photoelectrons' initial energy can reach up to 1eV. According to the literature, at this energy both N_2^+ and N^+ can be formed due to electron impact (N^+ is produced due to the dissociation of N_2). Table 3.8 summarizes the possible reactions due to electron impact in N_2 for electron energies of 30 eV, together with the respective cross-sections, appearance energies and the product distribution. The displayed probabilities were obtained using the cross sections for each primary ions of N_2 and the total ionization cross section provided in [87]. These primary ions (N_2^+ and N^+) will rapidly undergo reactions, transforming them into secondary ions. Table 3.9 presents a summary of secondary reactions, product distributions, and reaction rates, for collisions between N_2 and the primary ions from table 3.8, at room temperature.

N_3^+ and N_4^+ ions are formed from primary N^+ and N_2^+ ions by three-body reactions. Each of these reactions is reversible, where the forward reaction is favoured by high pressures and low E/N and the reverse reactions are favoured by high E/N. [7]. Ac-

Table 3.8: Ionization products, ionization cross sections for electron impact (E=30 eV) on N_2, appearance energies (A.E), and respective product distribution [Adapted from 87].

Reaction	**Cross Sec. (10^{-16}cm^2)**	**A. E. (eV)**	**Prod. Dist.**
$N_2 + e^- \rightarrow N_2^+ + e^-$	0.929	15.581	96.6 %
$N_2 + e^- \rightarrow N^+ + N + e^-$	0.0325	24.34	3.4 %

Table 3.9: Secondary reactions, product distribution and forward rate constants for the collisions of the primary ions of N_2.

Reaction	**Rate Const. (k)** (10^{-29} cm^{6}s^{-1})	**Reference**
$N^+ + 2N_2 \leftrightharpoons N_3^+ + N_2$	$5.0^{+}_{-}0.9$	[7]
$N_2^+ + 2N_2 \leftrightharpoons N_4^+ + N_2$	$1.8^{+}_{-}0.2$	

cording to W. Lindinger [80], for reduced electric fields bellow 150 Td the forward reaction is predominant and the products, once formed, are unlikely to dissociate into the reactants. The same author mentioned that the inverse reaction is only meaningful for values of E/N equal to or higher than 200 Td. Taking this into account, and since at the predominance of ion N_2^+ is much larger than of N^+ at our working conditions, it is expected that only N_4^+ ions will be formed, along with residual quantities of N_3^+, in our working conditions.

Similarly to what was calculated for other gases in previous sections, figure 3.17 shows the conversion of the primary into secondary ions over time. In this calculation the presence of impurities (such as water) was not considered and it was adopted the same method as before, using the rate constants described in table 3.9. As can be confirmed in figure 3.17 both reactions in nitrogen are fast, being only required 2 μs to convert 99.9% of N_2^+ into N_4^+ and $\approx$5.4 μs to convert N^+ into N_3^+. The transit times of the experimental measurements varied between 150 μs and 700 μs which are sufficiently large to allow all ions of N^+ and N_2^+ to be converted.

In table 3.10 it is shown a compilation of the mobility extrapolations for $E/N \rightarrow 0$ found in the literature. As it can be seen many authors identified identical mobilities for ions in nitrogen, in spite of the fact that the working pressures of the experiments were different.

In order to keep the table as simple as possible, the mobilities for N^+ are not displayed; we also believe that a comparison with the mobility of this ion is not necessary

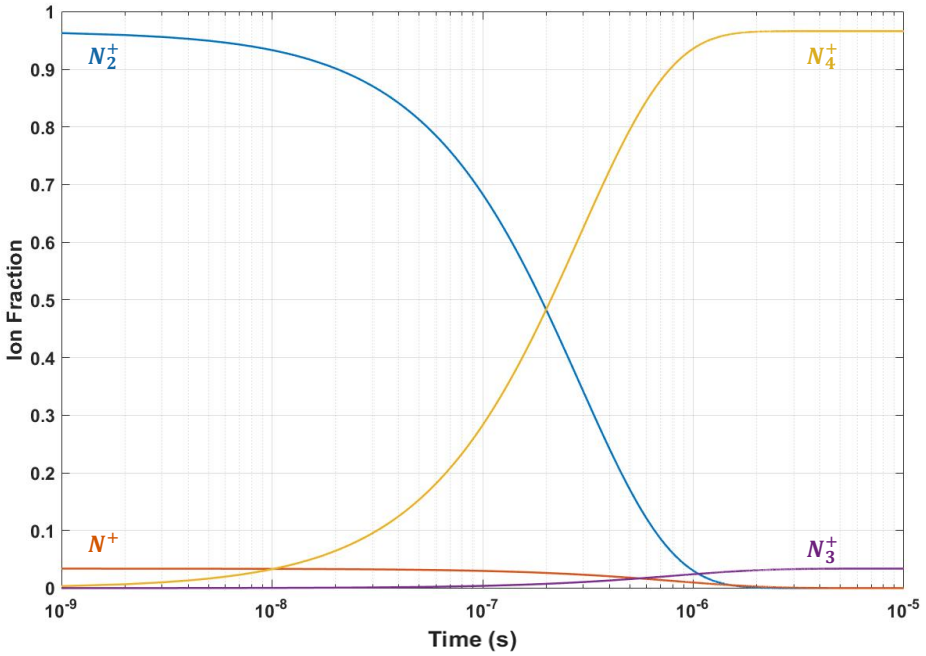

Figure 3.17: Ion abundance with time for pure N_2 at a pressure of 8 Torr and for energies of 30 eV.

since its formation is residual (3.4%) and further, it will quickly convert into N_3^+.

Regarding the peak with slowest mobility, we identified it as N_4^+, not only because the reaction paths show that in our experimental conditions, this ion will be the one that is preferentially produced but also because the mobility obtained for this peak is coherent with the values reported in the literature. The mobility measurement of N_4^+ in N_2 has been largely studied by different authors, although the experimental conditions of the different authors are very distinct they seem to agree in the mobility for this ion. Even the polarization limit given by Langevin formula only differs by less than 3% from the average literature values.

In respect to the second peak four possibilities are left - N^+, N_2^+, N_3^+ and impurities. As mentioned, we exclude the possibility of N^+ because in our pressure and E/N conditions its formation is residual (3.4%) and second, it will quickly convert into N_3^+, not dissociate back according to [7, 88, 89, 86]. Regarding the N_3^+ possibility, its formation is due to the N^+ ion which has a low initial concentration in our working conditions, and for this reason it is expected a residual formation of N_3^+.

In the case the N_2^+, it is expected that, for our experimental conditions, it will convert into N_4^+ and as N_3^+ will not dissociate back [7, 88, 89, 86].

We are then left with the possibility of impurities, more precisely the H_3O^+ ion.

Table 3.10: Zero field mobilities of nitrogen ions in pure N_2

Reference	**Mobility ($cm^2V^{-1}s^{-1}$)**	
	H_3O^+	$N_4{}^+$
J.T. Moseley *et al* (1969) [7]	-	$2.33^{+}_{-}0.08$
M. Saporoschenko(1965)[86]	-	$2.34^{+}_{-}0.05$
W. Lindinger *et al* (1976) [80, 88]	-	$2.38^{+}_{-}0.12$
A. N. C. Garcia *et al* (2012) [25]	-	$2.37^{+}_{-}0.02$
I. Dotan *et al* (1976) [85]	$2.76^{+}_{-}0.14$	-
Polarization Limit	3.11	2.42
This work (2016)	$2.79^{+}_{-}0.02$	$2.34^{+}_{-}0.02$

Table 3.11: Mobility of the ions observed for pure N_2 at room temperature (298 K) for different E/N and a pressure of 8 Torr.

E/N **(Td)**	**Mobility ($cm^2V^{-1}s^{-1}$)**	
	$N_4{}^+$	H_3O^+
$10.06^{+}_{-}0.05$	$2.34^{+}_{-}0.02$	$2.65\ ^{+}_{-}0.03$
$15.12^{+}_{-}0.04$	$2.32^{+}_{-}0.01$	$2.60\ ^{+}_{-}0.02$
$20.14^{+}_{-}0.01$	$2.307^{+}_{-}0.01$	$2.58\ ^{+}_{-}0.02$
$25.06^{+}_{-}0.06$	$2.31^{+}_{-}0.02$	$2.60\ ^{+}_{-}0.05$
$30.16^{+}_{-}0.02$	$2.30^{+}_{-}0.03$	$2.48\ ^{+}_{-}0.05$
$35.22^{+}_{-}0.02$	$2.30^{+}_{-}0.02$	$2.47\ ^{+}_{-}0.03$
$40.20^{+}_{-}0.01$	$2.29^{+}_{-}0.03$	$2.45\ ^{+}_{-}0.03$
$45.26^{+}_{-}0.01$	$2.28^{+}_{-}0.02$	$2.45\ ^{+}_{-}0.01$

This possibility is supported by several causes- first our mobility extrapolation to $E/N \rightarrow 0$ matches in 1% the mobility reported by I. Dotan *et al* [85] who measured the mobility of ions of water in N_2. Additionally, the fact that, after the detector had been clean up and GEM had been properly treated, as described in chapter 2, the spectrum obtained only shows one peak, supporting the idea of impurities. It is worth to point out that the remaining measurements in this document were either held before being introduced in the TMA system that is known to be a dirty gas or were carried out after the detector cleaning.

In table 3.11 are summarized the results obtained in our work for pure N_2.

3.3.2 Ne-N_2

This section aims to show and explain the results for neon-nitrogen (Ne-N_2) mixtures. It is worth pointing out that these results are preliminary and even though they will be discussed in this section, it should be kept in mind that further measurements are necessary in order to withdraw trustworthy conclusions regarding this mixture.

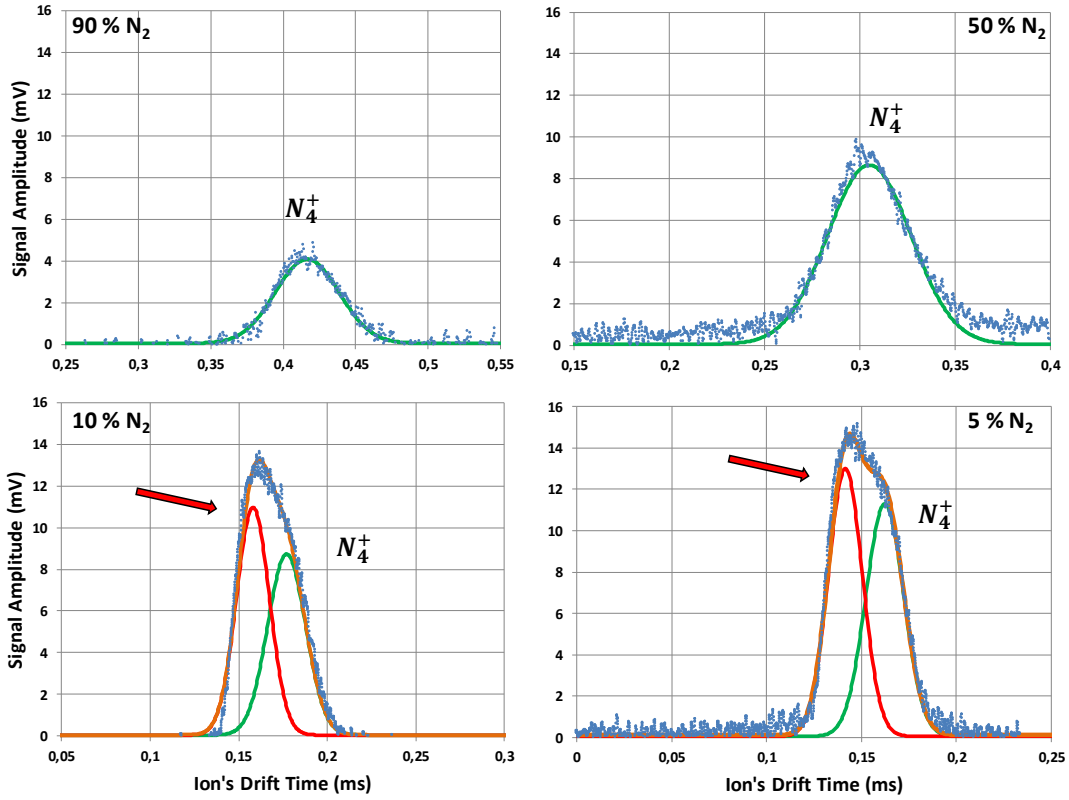

Figure 3.18: Time-of-arrival spectra averaged over 128 pulses for several Ne-N_2 mixtures (5%, 10%, 50%, 90% of N_2) at a pressure of 8 Torr, temperature of 298 K and for a reduced electric field of 15 Td with a voltage across the GEM of 23 V (background noise was already subtracted)

Figure 3.18 shows distinct time-of-arrival spectra for several Ne-N_2 mixtures (5%, 10%, 50% and 90% of N_2) at a pressure of 8 Torr, temperature of 298 K and for a reduced electric field of 15 Td with a voltage across the GEM of 23 V. In neon-nitrogen mixtures with N_2 concentrations higher than 25% only one peak is observed.

Beyond the fact that the peak area varies with the N_2 concentration in the mixture, which is clearly related to the availability of N_2, a peak displacement to lower drift times with decreasing concentration of N_2 was also observed and it is translated into an increase in the ion mobility. It is important to point out that for N_2 concentrations in the mixture bellow 25% a second peak starts to appear at the left side of main peak,

being the most pronounced one obtained for concentrations bellow 10% of N_2.

For an energy of 23 eV the total ionization cross section for electron impact in Ne is 1.66×10^{-18} cm^2 [90], which is much lower than the one for N_2 (0.528×10^{-16} cm^2 [84]). As a result, it is expected that even at low N_2 concentrations the production of N_2 ions will be favoured. Furthermore, for greater concentrations of Ne in the mixture, Ne^+ ions will be produced in larger quantities, and in accordance with the rate constants reported in the literature, they are more probable to react with N_2 through equation 3.9 ($k = 1.1\times10^{-13}$cm^{3}s^{-1} [67]), instead of a third body reaction with Ne described by equation 3.11 ($k = 5.6\times10^{-32}$cm^{6}s^{-1} [24]) once the reaction time of this last one is higher than any other reaction channel in the pressure conditions used in this experiment. Regarding the N_2^+ ions, they will react with N_2 molecules and originate N_4^+ through a three body reaction (equation 3.10 with k=5×10^{-29}cm^{6}s^{-1} [7])

$$Ne^+ + N_2 \rightarrow N_2^+ + Ne \tag{3.9}$$

$$N_2^+ + 2N_2 \leftrightharpoons N_4^+ + N_2 \tag{3.10}$$

$$Ne^+ + 2Ne \rightarrow Ne_2^+ + Ne \tag{3.11}$$

Even though Itikawa [84] provides an excellent review about the different N_2 cross sections for numerous energy values present in the literature, in the case of rare gases, like Ne, the uncertainty on values of the electron-impact ionization cross sections has been a constant fact. Great differences can be found in values reported by different authors [references within 75, 81, 90]. The pioneering total-cross-section measurements of Rapp and Englander-Golden are generally viewed as the most trustworthy results[75].

This ambiguity will influence our reaction path calculation shown in figures 3.19 and 3.20, because the initial ion fraction of each gas is dependent on the total ionization cross section for electron impact. By using different cross sections reported in the literature, we could verify that the relative amount of initial ions formed for each gas could change significantly. Although the initial concentration of the ions will have meaningless impact in the time of reaction, it could lead to wrong conclusions about the final ions formed due their concentrations. For example, by simply changing the cross section value for the formation of Ne^+, the relative amount of Ne^+ ions that can be present initially varies almost 15%.

With this in mind, it should be noted in the analysis of figures 3.19 and 3.20, that the concentrations of each element can be changed according to the values of cross sections used.

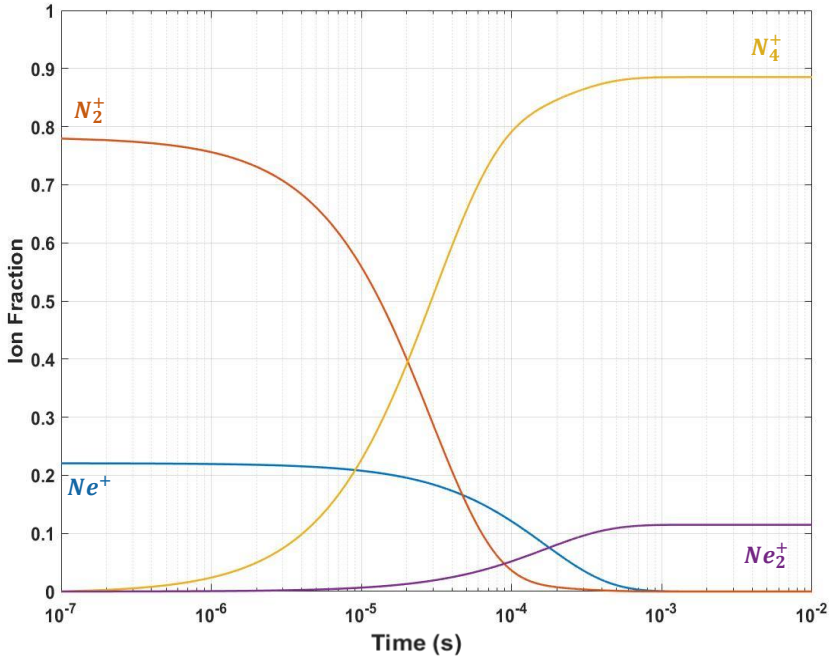

Figure 3.19: Ion abundance with time for a mixture of 90% Ne and 10% N_2 at a pressure of 8 Torr and energy of 23 eV.

Regarding figure 3.19, it is shown the concentration of each ion species in a mixture of 90% Ne and 10% N_2 for a pressure of 8 Torr. It is possible to see a formation of two final ions, N_4^+ and Ne_2^+.

In this particular mixture, the drift times measured range between 114 μs and 260 μs, for reduced electric fields between 10 and 20 Td. As a result, it can be seen that neither reactions will be completed at the time that the ions cross the double grid. In the case of 10% N_2 - 90% Ne, plotted in figure 3.18, we will obtain the following ion distribution- 83.14% of N_4^+; 7% of Ne_2^+; 8.7 % Ne^+ and 1.2% of N_2^+ . Considering this distribution, it is possible to deduced that for this mixture the main peak should be caused by N_4^+. However, it raises questions about the true nature of the second peak that appears that can be caused by Ne ions.

Another aspect important to point out is that the reaction time calculated should decrease with minor quantities of Ne in the mixture. The experimental drift times for a E/N of 15 Td extended between ≈120 μs and ≈440 μs (5% N_2 to 95% N_2, respectively). Consequently, for mixtures with N_2 concentrations higher than 25% only N_4^+ ion has time to form almost entirely as can be confirmed in figure 3.20, that shows the concentration evolution of each possible ion for a mixture of 25% of N_2 and 75% of Ne, allowing us to infer that the main peak (present in all mixtures) should be caused

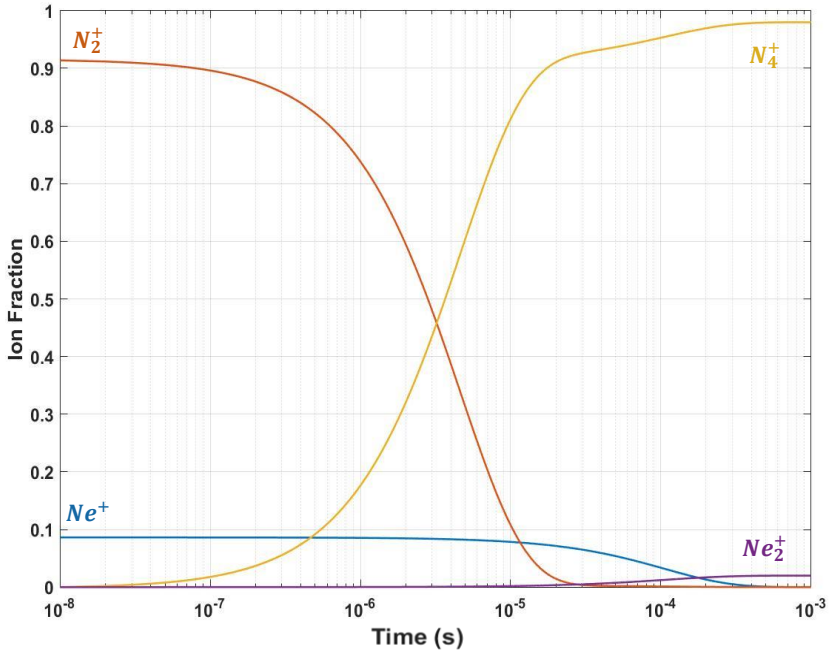

Figure 3.20: Ion abundance with time for a mixture of 75% Ne and 25% N_2 at a pressure of 8 Torr and energy of 23 eV.

by N_4^+.

In figure 3.21 it is plotted the inverse of the reduced mobility of the ions produced in the Ne-N_2 mixture as a function of different mixture ratios studied for a pressure of 8 Torr and for an E/N of 15 Td, at room temperature (298 K). The points in black are our experimental data for Ne-N_2 at the experimental conditions already mentioned; three points can be found in the pure Ne line (0% of N_2), that represent the reduced mobility of Ne^+, Ne_2^+, and N_2^+ ions in Ne (green, blue and red, respectively), which were obtained by P. N. B. Neves *et al* [24], O. J. Orient *et al* [83] and Y. Kondo *et al* [91]. To our knowledge the mobility of N_4^+ ion in Ne has not yet been measured.

In the case of 100% of N_2, 2 points are shown that match the mobilities of N_2^+ and N_4^+ ions. The mobility of the first ion was obtained by J. T Moseley in 1969 [7] and the second corresponds to an average value obtained through a few values reported in the literature. The values used are shown in section 3.3.1, where the results of pure nitrogen are explained (table 3.10).

Analogously to the other mixtures studied, Blanc's law was also used to predict which ions can originate the experimental data obtained. Two dotted lines are visible in figure 3.21, a blue one, that shows the Blanc's law prediction for N_2^+ and an orange, one that represents the prediction for N_4^+. In the case of the N_2^+ prediction, were used

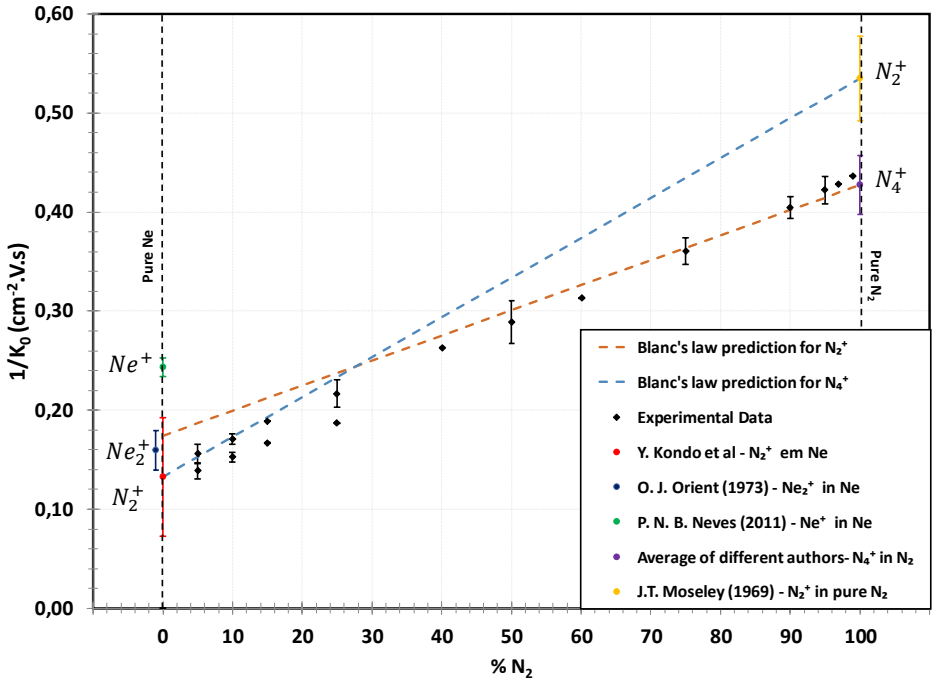

Figure 3.21: Reduced mobility of the ions produced in the Ne-N_2 mixtures for a pressure of 8 Torr and for an E/N of 15 Td at room temperature.

experimental values reported in the literature for the values of K_{0g1} and K_{0g2} in Blanc's law equation (1.8). Regarding N_4^+ an experimental value was used for the case of N_4^+ in N_2 while for N_4^+ in Ne the mobility value was calculated using Langevin's formula (see Equation 1.3).

Observing figure 3.21 it is possible to confirm that the ion mobility experimentally obtained for the main peak obeys the Blanc's law prediction for N_4^+ throughout almost the entire mixture range, starting to fail for mixtures with concentrations of N_2 bellow 25%.

By making a regression to the data obtained for the main peak, the mobility in Ne of the ion that causes this peak is 7.03 $cm^2V^{-1}s^{-1}$. The Langevin formula gives a mobility value for N_4^+ in Ne of 5.71 $cm^2V^{-1}s^{-1}$, which corresponds to a difference of 19% from the one achieved by the extrapolation of the experimental data. However, the mobility value obtained by Langevin formula also fails the prediction for the N_2^+ ion in Ne by 15% according to the value reported by Y. Kondo *et al* [91]. Assuming that the same happens to N_4^+, the experimental values obtained will follow Blanc's law prediction closely in the entire range.

Regarding the identification of the second peak, it is ambiguous. Two ions can be suggested: the peak is created by N_2^+ ions that could not be converted into N_4^+ or is

Table 3.12: Mobility of the ions observed in Ne-N_2 mixture for different ratios of N_2, obtained for different E/N and a pressure of 8 Torr at room temperature.

Mixture	**Mobility ($cm^2V^{-1}s^{-1}$)**			**Ion**
	10 Td	**15 Td**	**20 Td**	
5% N_2 - 95% Ne	$6.78^{+}_{-}0.08$	$6.41^{+}_{-}0.06$	$6.36^{+}_{-}0.01$	N_4^+
	$7.37^{+}_{-}0.07$	$7.20^{+}_{-}0.06$	$7.08^{+}_{-}0.08$	?
10% N_2 - 90% Ne	$6.02^{+}_{-}0.08$	$5.86^{+}_{-}0.03$	$5.64^{+}_{-}0.06$	N_4^+
	6.58	$6.55^{+}_{-}0.03$	$6.4^{+}_{-}0.06$	?
25% N_2 - 75% Ne	$3.47^{+}_{-}0.08$	$4.61^{+}_{-}0.06$	$4.54^{+}_{-}0.07$	N_4^+
	-	5.35	$5.17^{+}_{-}0.07$	?
50% N_2 - 50% Ne	$3.47^{+}_{-}0.13$	$3.46^{+}_{-}0.08$	$3.42^{+}_{-}0.02$	N_4^+
75% N_2 - 25% Ne	$2.81^{+}_{-}0.03$	$2.78^{+}_{-}0.04$	$2.78^{+}_{-}0.03$	N_4^+
90% N_2 - 10% Ne	$2.51^{+}_{-}0.02$	$2.47^{+}_{-}0.03$	$2.49^{+}_{-}0.06$	N_4^+
95% N_2 - 5% Ne	$2.41^{+}_{-}0.02$	$2.37^{+}_{-}0.03$	$2.37^{+}_{-}0.01$	N_4^+

caused by a mixture of Ne ions. In the case of the first hypothesis, we believe that this is not the reason for the second peak appearance because according to the cross sections and reactions rates reported in the literature, the presence of N_2^+ in a mixture of 90% Ne and 10% N_2 will be residual and probably none in a mixture of 75% Ne and 25% N_2, and we have detected a second peak with a considerable amplitude in these mixtures. For the second hypothesis, the main drawback is that the mobilities of Ne^+ and Ne_2^+ in Ne are significantly lower than the extrapolation of the data of the second peak. Unfortunately, a signal degradation study was not performed hence we do not have clues to what is the role of impurities in this mixture.

From 0 to 100% of N_2, ion mobility in the mixture depends on the ratio of the two gases. The mobility values of the peaks observed for the Ne-N_2 mixture ratios studied, obtained for an E/N of 10 Td to 20 Td, with a pressure of 8 Torr at room temperature (298 K) are summarized in table 3.12. The results for concentrations of 15%, 40%, 60%, 97% and 99% of N_2 are not included in table 3.12 because they were measured only once and it has not been possible to carry out additional measures to ensure their reproducibility. Despite that they are presented on the figure 3.21 chart and appear to

have the same trend of those shown in table 3.7.

Identically to the other mixtures already described, it was observed a small dependence of the mobility with E/N in the range of 15-25 Td.

3.4 Ne - CO_2 - N_2 (90 - 10 - 5)

In the present section we show the results and analysis for the 90% Ne, 10% CO_2 and 5% N_2 mixture that is currently used to fill the ALICE TPC. Also, a summary comparison is made with 90% Ne - 10% CO_2 mixture and with 90% Ar - 10% CO_2.

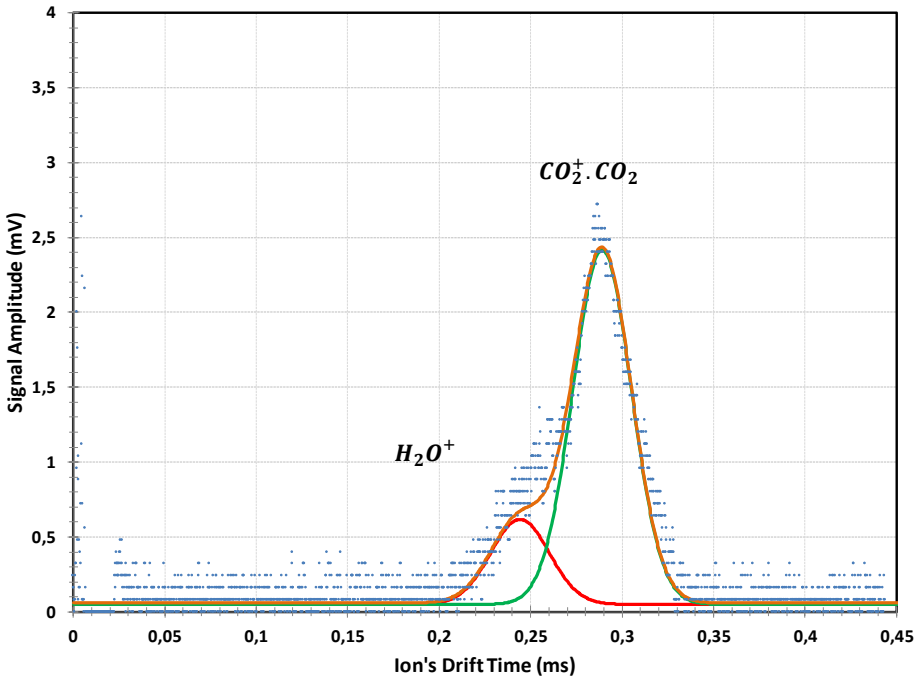

Figure 3.22: Time-of-arrival spectra for 90% Ne, 10% CO_2 and 5% N_2 at a pressure of 8 Torr and for a reduced electric field of 15 Td with a voltage across the GEM of 25 V at room temperature.

In figure 3.22 is displayed the time-of-arrival spectrum for the mixture at a pressure of 8 Torr, temperature of 298 K and for a reduced electric field of 15 Td with a voltage across the GEM of 25 V. As will be further discussed, the ions responsible for the peaks present in the spectrum will be the same as in Ne-CO_2 - the cluster $CO_2^+.(CO_2)$ for the main peak and impurities (probably water ions) for the fastest and smaller peak.

Since studying the nature of the ions present in a mixture of 3 gases can be a little tricky, the gases used for this study were analysed separately in pairs beforehand. The results for this study were exposed in previous sections, and were quite helpful in the

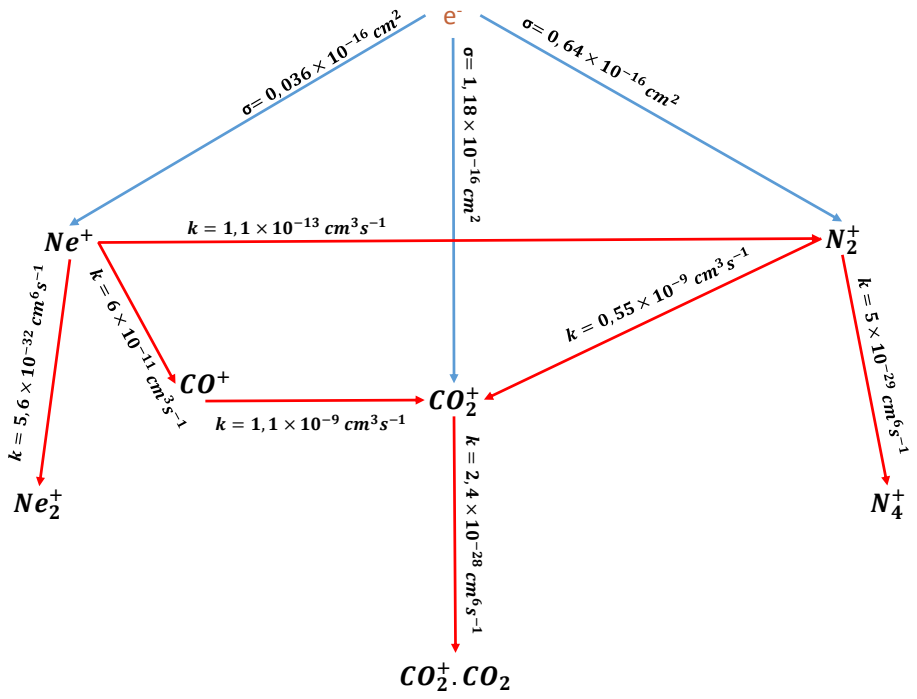

Figure 3.23: Summary of the reaction paths for a mixture of 90% Ne, 10% CO_2 and 5% N_2.

analysis of this mixture. Figure 3.23 shows a summary of the reaction paths that occur in this mixture. In the present analysis it was not considered the formation of primary ions with residuals quantities, like O^+, CO^+ and N_3^+.

The total ionization cross section for electron impact (for an energy of 25 eV) in Ne is 0.036×10^{-16} cm^2 [81] - much lower than the total cross section of CO_2 (1.18×10^{-16} cm^2 [76]) and N_2 (0.64×10^{-16} cm^2 [84]). By making a cross sections comparison of the different gases it is expected that even with only 10% CO_2 concentration, CO_2 ions are still the ones that are preferentially produced. Also, for this mixture there is a production of Ne^+ and N_2^+, in approximately equal amounts, as can be seen in figure 3.23.

The production of the CO_2^+ ion can occur by three channels/paths and then it is converted into $CO_2^+.(CO_2)$. At 8 Torr and for this mixture conditions, the main production of CO_2^+ is due to electron impact ionization. Also, with smaller contributions, Ne^+ and N_2^+ ions will transfer the charge to CO_2 leading to the formation of CO_2^+. In the case of Ne^+ ions, as was described in sections 3.2.3 and 3.3.2, according to the rate constants available, they are more likely to react with CO_2 (equation 3.3 and k =

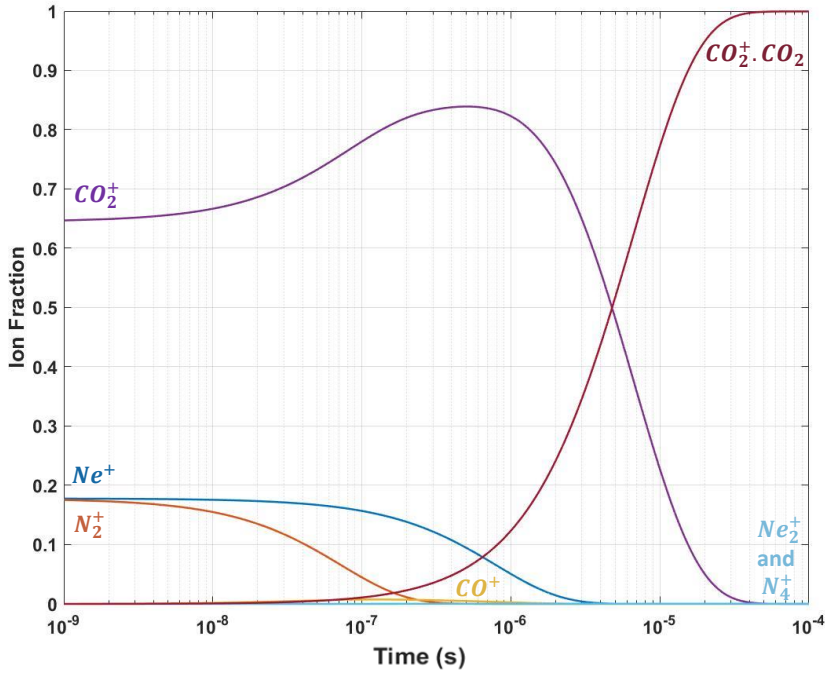

Figure 3.24: Ion abundance with time for a mixture of 90% Ne, 10% CO_2 and 5% N_2 at a pressure of 8 Torr and energies of 25 eV.

$0.06\pm0.1\times10^{-9}$ cm^3s^{-1} [67]), than with Ne via reaction 3.5 ($k = 5.6\times10^{-32}cm^6s^{-1}$ [24]) or with N_2 through equation 3.9 ($k = 1.1\times10^{-13}cm^3s^{-1}$ [67]). Regarding N_2^+ they are more likely to transfer the charge to CO_2 through reaction (3.6) ($k = 0.55\times10^{-9}cm^3s^{-1}$), rather than reacting with N_2 via the three-body reaction 3.7 ($k = 5\times10^{-29}cm^6s^{-1}$) for which the reaction time is higher.

As it can be observed in figure 3.24 it is expected that the final products formed be almost only $CO_2^+.(CO_2)$ (99.95% of total ions formed). An accurate interpretation of this figure shows that it is required ≈ 46 μs to convert the initial distribution of the ions into $CO_2^+.(CO_2)$. The drift times of the experimental measurements for an E/N range of 10 to 20 Td extended between 400 μs and 190 μs. Like what happened to the mixture of 90% Ne and 10 % CO_2, for an E/N of 20 Td almost 20% of the drift distance was travelled as CO_2^+.

We repeated this calculation, this time changing the pressure parameter to the atmospheric pressure as is the case in the ALICE TPC. At these conditions, the $CO_2^+.(CO_2)$ formation (99.9 %) is faster ($\approx$ 36 ns) than in our pressure conditions but in this case, it will occur the formation of residual quantities of Ne_2^+ (3.2%) and N_2^+ (0.9%), according to the cross sections and reaction rates used.

We attributed the second peak to the presence of water, that results from outgassing

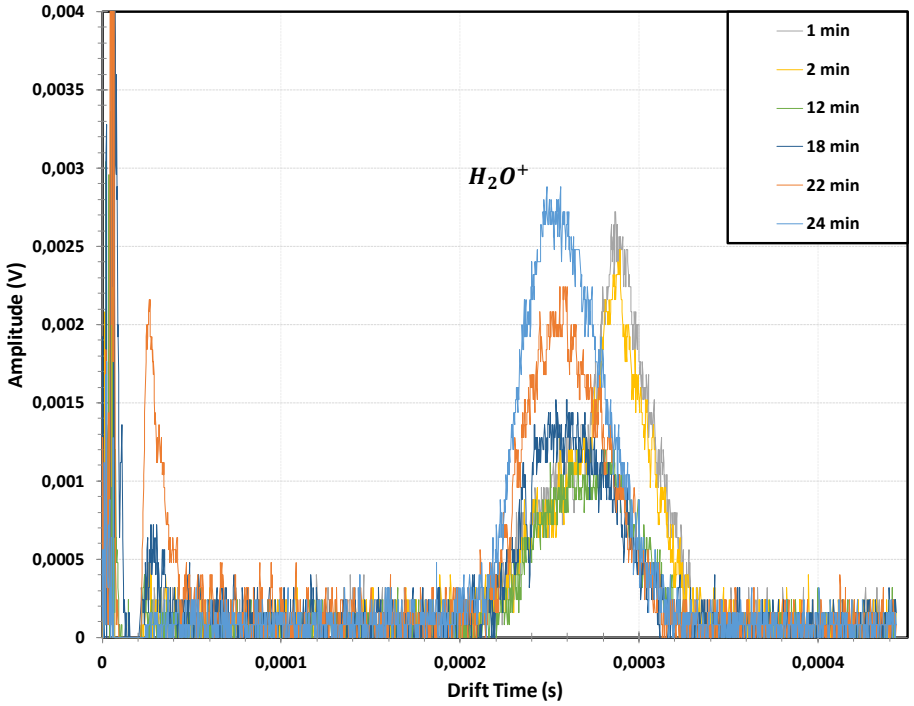

Figure 3.25: Signal degradation study of a time-of-arrival spectra for a mixture of 90% Ne, 10% CO_2 and 5% N_2 at a pressure of 8 Torr, temperature of 298 K and for a reduced electric field of 15 Td with a voltage across the GEM of 25 V. The ion responsible for the fastest peak is probably H_2O^+ .

processes inside the detector and was also observed in other mixtures such as Ar-CO_2 and Ne-CO_2 (sections 3.2.2 and 3.2.3). Comparatively to the previous mixture we performed a signal degradation study that is shown in figure 3.9. As before it is possible to notice a decrease in the amplitude of the main peak and an increase in the fastest peak, supporting the idea of impurities.

A comparison of the mobility values of the ions observed for the 90% Ne-10% CO_2 and 90% Ar-10% CO_2 mixtures at an E/N range of 10 to 20 Td, pressure range of 4 to 10 Torr and at room temperature (298 K) are summarized in table 3.6. As before, we verified a dependence of the mobility with E/N (from 10 to 20 Td), as can be observed in the mentioned table.

In all three mixtures, were detected the presence of impurities, mainly, water (sections 3.2.2 and 3.2.3). In Ne-CO_2, for 20 Td, we could not perform a proper fit to the data obtained for the second peak and therefore it was not compiled in the table.

Of the 3 mixtures, the one with Ar is the slowest of them all. Between the other two mixtures, the mobilities seem to have a constant variation of 0.1 $cm^2V^{-1}s^{-1}$, being the Ne-CO_2 a little faster.

Table 3.13: Mobility of the ions observed for the 90% Ne - 10% CO_2 - 5% N_2 mixture obtained for different E/N between 10 and 25 Td and for a 4 to 10 Torr pressure range at room temperature (298 K).

Mixture	**Mobility ($cm^2V^{-1}s^{-1}$)**		
	10 Td	**15 Td**	**20 Td**
90%Ne - 10%CO_2 - 5%N_2	$3.86^{+}_{-}0.04$	$3.74^{+}_{-}0.05$	$3.67^{+}_{-}0.02$
	$4.38^{+}_{-}0.003$	$4.33^{+}_{-}0.05$	$4.20^{+}_{-}0.06$
90%Ne - 10%CO_2	$3.96^{+}_{-}0.01$	$3.85^{+}_{-}0.05$	$3.77^{+}_{-}0.07$
	$4.69^{+}_{-}0.04$	$4.61^{+}_{-}0.19$	-
90%Ar - 10%CO_2	-	-	$1.850^{+}_{-}0.009$
			$2.21^{+}_{-}0.03$

Chapter 4

Conclusions

The conclusions for each of the mobility studies conducted has already been presented individually in chapter 3, however, here the results obtained for pure gases and the for the mixtures studied are briefly summarized. Also it is performed a general mobility comparison between all mixtures studied in our experimental system, including the ones studied in our laboratory by other authors, namely Xe-N_2 [30], Ar-CH_4 [29] and Ar-C_2H_6 [28].

With respect to the study of ion mobility of ions in their parent gas, CO_2 and N_2 studies were performed. In the first case only one peak was detected for reduced electric fields between 6 and 45 Td at a pressure of 8 Torr. Two possibilities emerged in the process of its identification, CO_2^+ or $CO_2^+.CO_2$. According to the reaction paths and our experimental conditions, the cluster $CO_2^+.CO_2$ will be the most probable candidate. However, due to a small discontinuity present in the experimental data of ion mobility, between 10 and 20 Td, we cannot infer which one is truly behind the nature of the peak. An extrapolation to a zero reduced electric field gives a mobility value of 1.17 $cm^2V^{-1}s^{-1}$. For the N_2, two peaks were detected, that were identified as N_4^+ and H_3O^+, for reduced electric fields between 6 and 60 Td and for a pressure range from 6 to 10 Torr. An extrapolation to a zero reduced electric field yields a mobility value of 2.34 $cm^2V^{-1}s^{-1}$ for N_4^+ and 2.79 $cm^2V^{-1}s^{-1}$ for H_3O^+. The results shown are in good agreement with the ones reported in the literature. The water problem was solved by a proper cleaning of the IDC.

Since the development of the experimental apparatus, eight different studies of ion mobility in mixtures were performed. Figure 4.1 shows a compilation of the mixtures studied at LIP Coimbra. Although other experimental conditions were tested, only the results obtained for a reduced electric field (E/N) of 15 Td, at room temperature and at preassures typically in a range of 6 to 12 Torr were plotted. Error bars were not

included in order to obtain an understandable graphic, however the data shown in 4.1 is available in the references cited throughout this analysis.

From the work presented, a number of conclusions can be withdrawn. Taking a closer look at this figure it is possible to observe a clear dependence on the mass of components of the mixtures. Here, four distinct groups of mixtures can be identified. The Ne group, has the fastest mobilities measured in our experimental system, in which the fastest of them all is Ne-N_2, as expected, due to the small masses of both gases in the mixture, as can be verified in the plot; this group comprehends also Ne-CO_2. The Ar group, which includes mixtures of Ar-CO_2 [31], Ar-C_2H_6 [28] and Ar-CH_4 [29]. There is also the N_2 group, that has mobilities close to the ones obtained for the same additives with Ar - for this reason in figure 4.1 the mixtures with N_2 are plotted as a function of the other mixture component (Ne, Xe and CO_2), so that the experimental data do not overlap with the ones from Ar mixtures. And finally, the Xe group, that shows the slowest mobilities measured in our experimental system, due to the fact that Xe has a large mass; this group comprehends Xe-N_2 and Xe-TMA mixtures.

Concerning the Ar mixtures, the Ar-CH_4 has the highest mobility values of the three Ar mixtures tested and Ar-CO_2 has the lowest, as expected, due the mass of each components of the additives to Ar. In the case of Ar-C_2H_6 the mobilities values reported were slower than the previous mixture. The authors found that for Ar concentrations below 80% only two peaks were observed in the time-of-arrival spectra, which were attributed to ion species with 3-carbons and with 4-carbons. A third peak appears for Ar concentrations above 80% which the authors attribute to the $C_5H_{11}{}^+$ ion. Regarding Ar-CO_2, which is the slowest mixture with Ar, measurements were performed for pressures ranging from 8 to 10 Torr and for reduced electric fields in the 10 Td to 25 Td range. For Ar concentrations bellow 80% we only observed one peak, which was attributed to $CO_2^+.CO_2$ although a peak caused by impurities starts to appear for Ar concentrations above 80% . With regard to the mobilities of $CO_2^+.CO_2$, they varied between K_0=1.95$\pm$0.04 $cm^2V^{-1}s^{-1}$ for 95% of Ar and 1.13$\pm$0.02 $cm^2V^{-1}s^{-1}$ for 5% of Ar at an E/N of 20 Td.

Two mixtures were also tested wherein one of the elements used was Ne. In the first ones, Ne-CO_2 mixtures, only one peak was observed for Ne concentrations bellow 75%, which was attributed to $CO_2^+.(CO_2)$. Above this Ne concentration value a second-small peak appears at the left side of the main peak, and like in Ar-CO_2 it was also attributed to impurities. The mobility values for the $CO_2^+.CO_2$ peak range between 3.51$\pm$0.05 $cm^2V^{-1}s^{-1}$ and 1.07$\pm$0.01 $cm^2V^{-1}s^{-1}$ in the 95%-1% concentration interval for Ne. As for the second case, Ne-N_2 mixtures, the presence of two peaks were de-

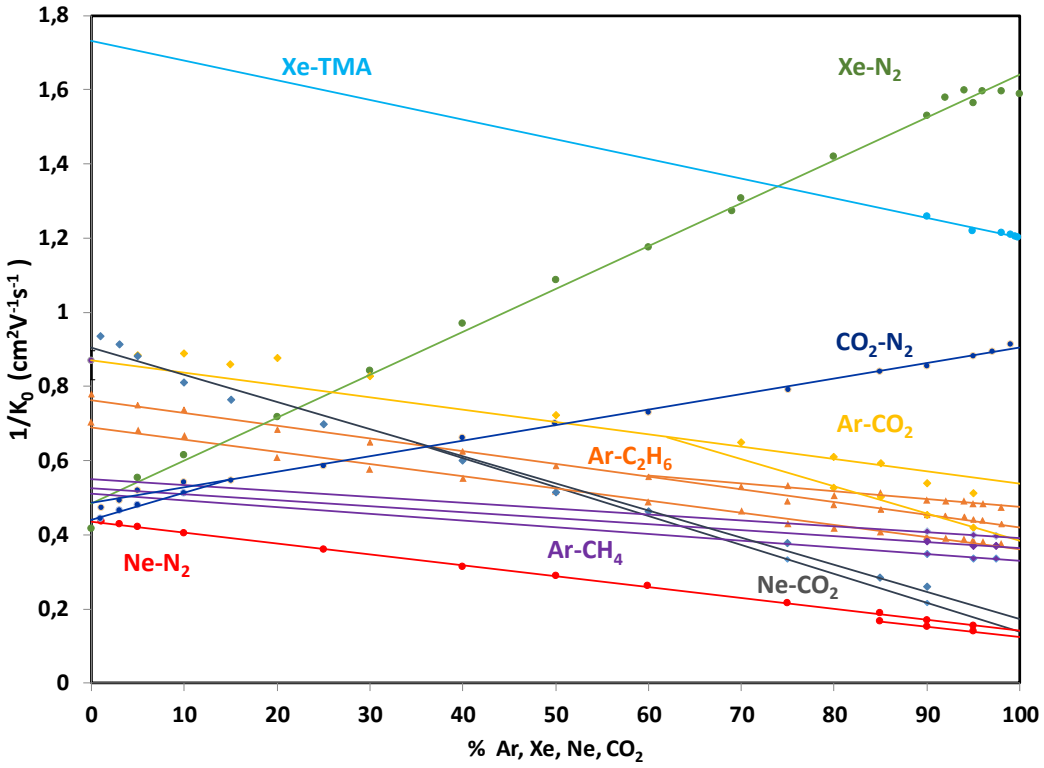

Figure 4.1: Compilation of ion mobility studies on mixtures that were conducted at LIP.

tected, depending on the gas ratios of Ne. The main peak was identified as N_4^+ and the K_0 obtained ranges between 6.41±0.06 $cm^2V^{-1}s^{-1}$ and 2.37±0.03 $cm^2V^{-1}s^{-1}$ at an E/N of 15 Td and N_2 concentration range between 5% to 95%. The second peak appears for Ne concentrations above 75%, and two possibilities were considered for its cause, N_2^+ or Ne_2^+. In this case, K_0 obtained ranges between 7.20±0.06 and 5.35 $cm^2V^{-1}s^{-1}$.

Regarding N_2 mixtures, three different gases were already tested together with this component in our experimental apparatus, namely Xe-N_2, CO_2-N_2 and Ne-N_2. This last one was formerly described in last the paragraph. In the case of Xe-N_2 the authors only detected one peak and concluded that the presence of N_2 drastically increases the mobility of Xe ions in the mixture. Just adding 10% of N_2 in mixture increases Xe ions mobility in roughly 6%. The mobilities these peaks varied between K_0=0.65±0.01 $cm^2V^{-1}s^{-1}$ for 1% of N_2 and 1.81±0.03 $cm^2V^{-1}s^{-1}$ for 95% of N_2. In the CO_2-N_2 case, bellow 90% of N_2 concentration in the mixture, the time-of-arrival spectra revealed only one peak which was attributed to $CO_2^+.CO_2$. A second peak appears for N_2 concentrations above 90%, which has higher mobility and was ascribed to N_4^+. The mobility values of the main peak range between 2.11±0.04 $cm^2V^{-1}s^{-1}$ and

$1.10^{+}_{-}0.03$ $cm^2V^{-1}s^{-1}$ in the 1%-99% interval of CO_2, while for the second they range from $2.26^{+}_{-}0.02$ $cm^2V^{-1}s^{-1}$ and $1.95^{+}_{-}0.04$ $cm^2V^{-1}s^{-1}$ (1% to 10% of CO_2).

An important conclusion to mentioned is that for mixtures in which one of the components is CO_2, Blanc's law does not yield a correct prediction of its mobility because at our pressure conditions, depending on the relative amount of CO_2 in the mixture, a considerable part of the drift distance can be travelled as CO_2^+. As a result of this, for all mixtures studied with CO_2, the experimental results obtained are located between the Blanc's law prediction for CO_2^+ and $CO_2^+.CO_2$, approaching to Blanc's law prediction for $CO_2^+.CO_2$ for higher concentrations of CO_2 .

In the end, we also determined the mobility value of the current filling mixture of ALICE TPC (90% Ne - 10% CO_2 - 5% N_2). We tested this mixture for pressures between 4 and 10 Torr and for a reduced electric field range of 10 to 20 Td. At these working conditions two peaks were detected, where the main peak was also attributed to $CO_2^+.CO_2$ and the other to impurities. The time-of arrival spectra obtained for this mixture were similar to the ones for 90% Ne and 10% CO_2. The K_0 obtained for the main peak ranges between $3.86^{+}_{-}0.04$ $cm^2V^{-1}s^{-1}$ and $3.67^{+}_{-}0.02$ $cm^2V^{-1}s^{-1}$ for E/N within 10 to 20 Td.

Chapter 5

Improvements and Future work

5.1 Mixtures with practical importance

Gas-filled detectors have been used extensively in radiation detection. The resolution, dead time, range of operation and other features of this types of detectors varies with the filling mixture. The gas choice depends on several parameters like high drift velocity of the ions and electrons for different values of E/N, the Townsend coefficient and other parameters such as attachment coefficient and diffusion[92].

By studying the mobility of different mixtures with practical use, we supply experimental data to the scientific community that works with this kind of detectors and specially in large experiments like CMS and ALICE, helping in the choice of a suitable gas mixture. Normally there are simulation programs, like Garfield, that allow to calculate these parameters for a wide range of pressure and E/N. However, experimental data are very important in these cases because it provides a reliable way to validate the simulation tools and results obtained, despite of the fact that our experiment only allows the measurement of one of the parameters and for a lower range of pressure and E/N.

As a suggestion and due to their practical use in gaseous detectors, the following gas mixtures represent a good choice for the next ion mobility studies that may be carried out in our experimental system.

- Ne-CO_2-N_2
- Ar-CO_2-N_2
- Xe-CO_2-N_2
- Ne-CF_4

- Ar-CF_4
- Xe-CF_4
- Xe-CO_2

Regarding the Ne-CO_2-N_2 mixtures, it is very important to complete the study already started, by taking measurements for new electric field and pressure conditions and also by varying the relative amount of quenchers to see how the mobility of the mixture evolves. Additionally, testing the mixtures of Ar-CO_2-N_2 and Xe-CO_2-N_2 for the same conditions could be useful to compare with Ne-CO_2-N_2 (90-10-5), that was the mixture chosen to fill the ALICE TPC.

5.2 Identification of gaps and Future optimization

In science there is a continuous pursuit for improved experimental systems, so that more precise and exact measurements can be obtained, or so that new functions can be added, allowing a deeper and more complex analysis and understanding of physical phenomena.

In this context, it was recognized that certain features could be optimized, whereby the possible flaws were identified and means to solve them were proposed, and potential improvements to this system were also discussed.

One way to enhance the precision of the mobility measurements and of the reaction rates is to try to reduce the amount of impurities present, by performing an appropriate heating of the walls of the detector. However, this is not a viable technique since some of the detector's components, such as glues and solders, are not resistant to a high increase in the temperature.

According to P.N.B. Neves, who calculated the outcome of the space-charge effects for this detector, this effects can be reduced by operating at low VGEM voltages and appropriate levels of reduced drift electric field (E/N), that cannot be too high nor too low. The goal is to produce the smallest amount of ions that can be detected, while ensuring that these ions can be efficiently extracted from the GEM holes. On a practical level, for a pressure of 8 Torr and for a voltage across the GEM of 25 V, we cannot obtain a signal bellow a E/N of 5 Td.

The system described above was designed with the intention of being able to determine the longitudinal diffusion coefficient associated with the diffusion of atomic ions and dimmer ions in rare gases. Until this date, this measurement was not possible to achieve with great precision, since it is affected by the space-charge effects, the

conversion rate of the atomic ion into the dimmer ion and the presence of impurities [4].

Table 5.1: Summary of improvements, gaps and respective solutions to the system.

Gaps/Improvements	**Solution**
Impurities Effects	Perform backing
Detecting lighter ions	Increase the drift distance
Detecting negative ions	Replicate the detection system
Calculate the ions diffusion coefficient in noble gases	Increase the drift distance (Effect of impurities can be determinant)
Resolution Improvement	Increase the drift distance

The introduction of a variable drift distance will promote two important benefits. First of all, it will guarantee that with the current system will attain a stationary state will be obtained, even when working at low pressures and high values of reduced electric fields (E/N), given that by increasing the drift distance, it is assured that the ions will achieve the necessary collisions with the gas atoms/molecules. Also, the detector's resolution will be improved, which will also allow the detection of lighter ions and also faster ions, since these ion's signal will no longer be overlapped with the signal induced by the lamp.

The detection of negative ions will allow the gathering of additional information to help identify the ions present in the sample.

Table 5.1 aims to summarize the improvements and solutions suggested for this system.

Finally, it was concluded that the viable improvements that can be conducted in this system were:

- Variation of the drift distance
- Detection of negative ions

5.2.1 Redesign proposal

According to what has been described in the previous section, two modifications to the structure of our drift detector were designed in Solid Works.

The first is shown in figure 5.1, where the drift structure for the detection of positive ions was replicated for negative ions. Because of this, the GEM that works as an

ion source, is now placed in a central position and two double grids are above and below it.

Regarding the electrical supply of the GEM and of the stainless steel rings responsible to make an uniform electric field along both of these distances , this should not be problematic since there is enough space to insert the connectors and feedthroughs required to perform an adequate electric power supply, using the some chamber.

J. Miyamoto *etal* [93] were the first to report, in 2004, the compatibility of the GEM as an ion source for negative ions. They also reported some results of GEM gain in negative ion drift gases (NI-gases) mixtures for pressures close to the atmospheric one. Their apparatus used a GEM with 50 mm diameter that was assembled 7,5 mm below a mesh electrode. Their detector structure seems to have some similarities to the one that we use for detecting positive ions we expected, the designed structure present in figure 5.1 to be functional.

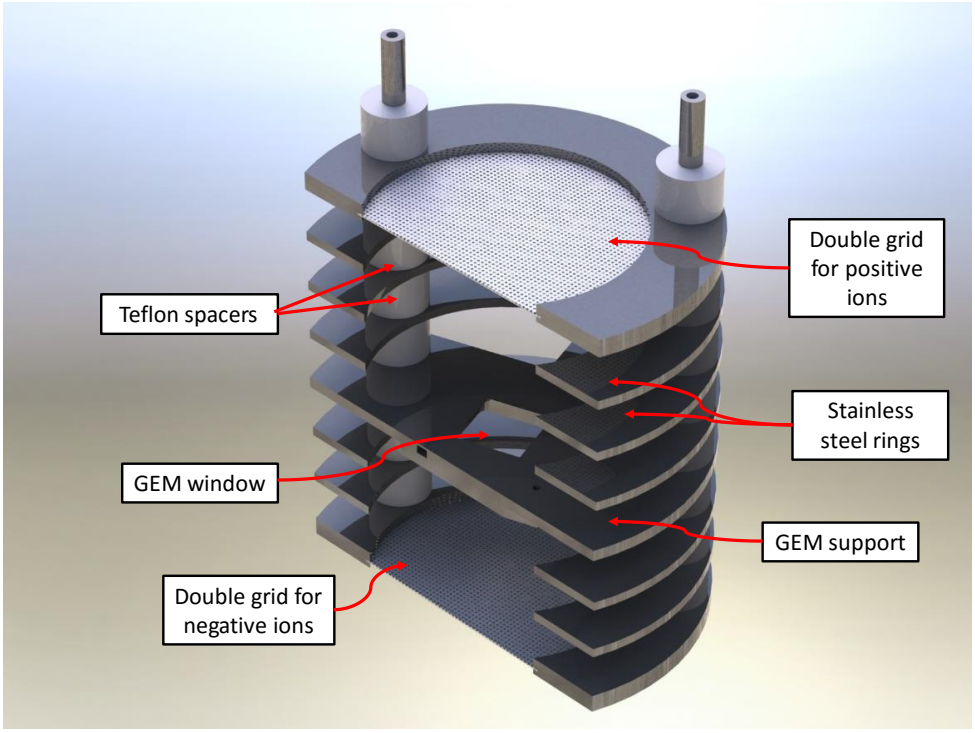

Figure 5.1: Redesign proposal for the detection of negative ions.

Also within the scope of my work, a structure was designed to allow the variation of the drift distance, and similarly to the previous design, it was envisioned to incorporate the current IDC and reuse some of its parts. However, this redesign is not totally complete and for that reason was not included in this chapter. Nevertheless, it is briefly explained in the next paragraphs.

The designed structure is similar to the one in figure 5.1, though in this case the

GEM support is smaller and it is not fixed to the stainless steel ring structure and Teflon spacers, in order to be able to move inside the rings, adopting one of its predefined positions.

The stainless steel rings have a cut with a section of 1 cm so that the support piece of the GEM is connected to a Teflon piece, which will act as a bridge between the inside and the outside of the detector; its function is to align the GEM support with the rings position so that the field is kept uniform.

Several aspects still have to be taken into account, such as which is the effect of the cut on the stainless steel rings in the field uniformity or how the electrical power will be supplied to the GEM and the rings.

Changing the drift distance should not have many limitations on the detector, which should work for different drift distances; lower drift distances than the current one have already been tested, and the main difference noticed was a degradation of the resolution.

References

[1] G. A. Eiceman, Z. Karpas, and H. H. J. Hill, *Ion Mobility Spectrometry*. CRC Press - Taylor & Francis Group, third ed., 2014.

[2] P. Langevin, "Une formule fondamentale de théorie cinetique," *Annal. Chim. Phys.*, vol. 5, p. 245, 1905.

[3] E. A. Mason and E. W. Mcdaniel, *Transport Properties of Ions in Gases*. John Wiley & Sons, Inc., 1988.

[4] P. Neves, *Studies on the mobility of monoatomic and dimer noble gas ions in their parent gases*. PhD thesis, Universidade de Coimbra, 2009.

[5] A. M. Tyndall, "The Mobility of Positive Ions in Gases," *Cambridge University Press*, 1938.

[6] L. B. Loeb, *Basic processes of gaseous electronics*. University of California Press, 1955.

[7] J. T. Moseley, R. M. Snuggs, D. W. Martin, and E. W. McDaniel, "Mobilities, diffusion coefficients, and reaction rates of mass-indentified nitrogen ions in nitrogen," *Physical Review*, vol. 178, no. 1, pp. 240–248, 1969.

[8] H. W. Ellis, R. Y. Pai, E. W. Mcdaniel, and L. A. Viehland, "Transport Properties of gaseous ions over a wide energy range," *Atomic Data and Nuclear Data Tables*, vol. 17, no. 3, pp. 117–210, 1976.

[9] H. W. Ellis, E. W. McDaniel, D. L. Albritton, L. A. Viehland, S. L. Lin, and E. A. Mason, "Transport Properties of Gaseous Ions Over a Wide Energy Range, Part II," *Atomic Data and Nuclear Data Tables*, vol. 22, pp. 179–277, 1978.

[10] H. W. Ellis, M. G. Thackston, E. W. McDaniel, and E. A. Mason, "Transport properties of gaseous ions over a wide energy range. Part III," *Atomic Data and Nuclear Data Tables*, vol. 31, no. 3, pp. 113–151, 1984.

[11] L. A. Viehland and E. A. Mason, "Transport Properties of Gaseous Ions Over a Wide Energy Range, IV," *Atomic Data and Nuclear Data Tables*, vol. 60, pp. 37–95, 1995.

[12] S. Armenta, M. Alcala, and M. Blanco, "A review of recent, unconventional applications of ion mobility spectrometry (IMS).," *Analytica chimica acta*, vol. 703, pp. 114–23, oct 2011.

[13] E. W. Mcdaniel and L. A. Viehland, "The Transport of Slow Ions in Gases: Experiment, Theory, and Applications," *Physics Reports (Physics Letters)*, vol. 110, no. 5/6, pp. 333–367, 1984.

[14] H. E. Revercomb and E. A. Mason, "Theory of Plasma Chromatography/Gaseous Electrophoresis- A Review," *Analytical chemistry*, vol. 47, no. 7, pp. 970–983, 1975.

[15] J. A. Hornbeck, "The Drift Velocities of Molecular and Atomic Ions in Helium, Neon and Argon," *Physical Review Second Series*, vol. 84, no. 4, pp. 610–615, 1951.

[16] Y. Kalkan, "Cluster ions in gas-based detectors," *Journal of Instrumentation*, vol. 10, no. July, p. 07004, 2015.

[17] D. Nygren, "High-pressure xenon gas electroluminescent TPC for 0-ν $\beta\beta$-decay search," *Nuclear Instruments and Methods in Physics Research, Section A: Accelerators, Spectrometers, Detectors and Associated Equipment*, vol. 603, no. 3, pp. 337–348, 2009.

[18] A. Blanc, "Recherches sur le mobilities des ions dans le gaz," *Journal of Applied Physics*, vol. 7, p. 825, 1908.

[19] F. Sauli, "GEM: A new concept for electron amplification in gas detectors," *Nuclear Instruments and Methods in Physics Research, Section A: Accelerators, Spectrometers, Detectors and Associated Equipment*, vol. 386, no. 96, pp. 531–534, 1997.

[20] F. Sauli, "The gas electron multiplier (GEM): Operating principles and applications," *Nuclear Instruments and Methods in Physics Research, Section A: Accelerators, Spectrometers, Detectors and Associated Equipment*, vol. 805, pp. 2–24, 2016.

[21] P. N. B. Neves, C. A. N. Conde, and L. M. N. Távora, "Experimental measurement of the mobilities of argon ions in gaseous argon," *IEEE Nuclear Science Symposium Conference Record*, vol. 2, pp. 668–670, 2006.

[22] P. N. B. Neves, C. A. N. Conde, and L. M. N. Távora, "Experimental measurement of the mobilities of atomic and dimer Ar, Kr, and Xe ions in their parent gases," *Journal of Chemical Physics*, vol. 133, 2010.

[23] P. Neves, C. Conde, and L. Távora, "The X^++2X→X_2^++X reaction rate constant for Ar, Kr and Xe, at 300K," *Nuclear Instruments and Methods in Physics Research Section A: Accelerators, Spectrometers, Detectors and Associated Equipment*, vol. 619, pp. 75–77, 2010.

[24] P. N. B. Neves, A. N. C. Garcia, A. M. F. Trindade, J. A. S. Barata, and L. M. N. Távora, "Experimental Measurement of the Ne^+ and Ne_2^+ mobilities and the reaction rate coefficient for $Ne^+ + 2Ne \rightarrow Ne_2^+ + Ne$," *IEEE Transactions on Nuclear Science*, vol. 58, no. 4, pp. 2060–2063, 2011.

[25] A. N. C. Garcia, P. N. B. Neves, A. M. F. Trindade, F. P. Santos, and C. A. N. Conde, "A new contribution to the experimenal measurement of the N_4^+ ion mobility in N_2 at 298K," *Journal of Instrumentation*, vol. 7, pp. P02012–P02012, 2012.

[26] A. M. F. Trindade, "Experimental measurements of the mobility of methane ions in methane," *Journal of Instrumentation*, vol. 7, p. P06010, 2012.

[27] A. F. V. Cortez, A. N. C. Garcia, P. N. B. Neves, F. P. Santos, F. I. G. M. Borges, J. A. S. Barata, and C. A. N. Conde, "Experimental measurement of the mobility of ions originated in ethane in their parent gas," *Journal of Instrumentation*, vol. 8, no. 07, p. P07013, 2013.

[28] A. F. V. Cortez, A. N. C. Garcia, P. N. B. Neves, F. P. Santos, F. I. G. M. Borges, J. A. S. Barata, and C. A. N. Conde, "Experimental ion mobility measurements in Ar-C_2H_6 mixtures," *Journal of Instrumentation*, vol. 8, p. P12012, 2013.

[29] A. M. F. Trindade, A. Cortez, P. N. B. Neves, A. N. C. Garcia, J. Escada, F. P. Santos, F. I. Borges, J. A. S. Barata, and C. A. N. Conde, "Experimental study on ion mobility in Ar-CH_4 mixtures," *Journal of Instrumentation*, vol. 9, p. P06003, 2014.

[30] A. N. C. Garcia, P. N. B. Neves, A. M. F. Trindade, A. F. V. Cortez, F. P. Santos, and C. Conde, "Experimental ion mobility measurements in Xe-N_2 mixtures," *Journal of Instrumentation*, vol. 9, pp. P07008–P07008, 2014.

[31] P. M. C. C. Encarnação, A. F. V. Cortez, M. G. A. Pinto, P. N. B. Neves, A. M. F. Trindade, F. P. Santos, F. I. G. M. Borges, J. A. S. Barata, and C. A. N. Conde,

"Experimental ion mobility measurements in Ar-CO_2 mixtures," *Journal of Instrumentation*, vol. 10, pp. P01010–P01010, 2015.

[32] P. M. C. C. . Encarnação, A. F. V. Cortez, R. Veenhof, P. N. B. Neves, F. P. Santos, A. M. F. Trindade, F. I. G. M. Borges, and C. A. N. Conde, "Experimental Ion Mobility measurements in Ne-CO_2 and CO_2 -N_2 mixtures," *Journal of Instrumentation*, vol. 11, no. 05, pp. P05005–P05005, 2016.

[33] G. F. Knoll, *Radiation Detection and Measurement*. John Wiley, New York, fourth ed., 2010.

[34] A. Garcia, *Gaseous Mixtures/Detection Media Studies for NEXT Experiment: A contribution*. Msc thesis, Universidade de Coimbra, 2012.

[35] S. Bachmann, A. Bressan, L. Ropelewski, F. Sauli, A. Sharma, and D. Mo, "Charge amplification and transfer processes in the gas electron multiplier," *Science*, vol. 438, pp. 376–408, 1999.

[36] "WRG-S-NW25 [online]." Available at https://shop.edwardsvacuum.com/products/ d14701000/view.aspx [Accessed 17 May 2016].

[37] "Edwards Barocel Pressure Sensor 600AB Trans 1000TR [Online]." Available at: http://saba.kntu.ac.ir/eecd/ecourses/instrumentation/projects/reports/Poly 20Vaccum/BEdwards/Barocel_600.pdf [Accessed 14 May 2016].

[38] "Argon Gas Cylinder [online]." Available at http://www.lindegas.pt/internet.lg.lg.prt/en/images/Argon AP_082015303_41538.pdf [Accessed 15 May 2016].

[39] "Nitrogen Gas Cylinder [online]." Available at http://www.lindegas.pt/internet.lg.lg.prt/en/images/Azot AltaPureza_082015303_41541.pdf [Accessed 15 May 2016].

[40] "Neon Gas Cylinder [online]." Available at http://www.lindecanada.com/ internet.lg.lg.can/en/images/neon-pure-gas135_88303.pdf [Accessed 15 May 2016].

[41] "Xenon Gas Cylinder [online]." Available at: http://www.lindecanada.com /internet.lg.lg.can/en/images/linde-xenon135_28248.pdf [Accessed 15 May 2016].

[42] "Carbon Dioxide Gas Cylinder [online]." Available at http://www.praxair.com/~/media/praxairus/Documents/Specification Sheets and Brochures/Gases/Carbon Dioxide/Carbon Dioxide CO2 Spec Sheet SS P4574.pdf?la=en [Accessed 15 May 2016].

[43] "Trimethylamine Gas Cylinder [Online]." Available at http://p110018. mittwald-server.info/pdf/Trimethylamine.pdf [Accessed 15 May 2016].

[44] A. Breskin, "CsI UV photocathodes: History and mystery," *Nuclear Instruments and Methods in Physics Research, Section A: Accelerators, Spectrometers, Detectors and Associated Equipment*, vol. 371, no. 1-2, pp. 116–136, 1996.

[45] B. Hoeneisen, D. F. Anderson, and S. Kwan, "A CsI-TMAE photocathode with low-pressure readout for RICH," *Nuclear Instruments and Methods in Physics Research, Section A: Accelerators, Spectrometers, Detectors and Associated Equipment*, vol. 302, pp. 447–454, 1991.

[46] V. D. A. B. R. Chechik, "Progress in ultrafast Csl-photocathode gaseous Imaging photomultipllers," *Nuclear Instruments and Methods in Physics Research, Section A: Accelerators, Spectrometers, Detectors and Associated Equipment*, vol. 308, pp. 519–532, 1991.

[47] J. Va'vra, A. Breskin, A. Buzulutskov, R. Chechik, and E. Shefer, "Study of CsI photocathodes: Volume resistivity and ageing," *Nuclear Instruments and Methods in Physics Research, Section A: Accelerators, Spectrometers, Detectors and Associated Equipment*, vol. 387, no. 1-2, pp. 154–162, 1997.

[48] T. C. Chi, "Electrical resistivity of alkali elements," *Journal of Physical and Chemical Reference Data*, vol. 8, no. 2, pp. 339–438, 1979.

[49] A. Bressan, J. C. Labbé, P. Pagano, L. Ropelewski, and F. Sauli, "Beam tests of the gas electron multiplier," *Nuclear Instruments and Methods in Physics Research, Section A: Accelerators, Spectrometers, Detectors and Associated Equipment*, vol. 425, no. 1, pp. 262–276, 1999.

[50] R. Cohen, *Signal Denoising Using Wavelets*. PhD thesis, Technion, Israel Institute of Technology, 2012.

[51] D. L. Donoho and I. M. Johnstone, "Threshold selection for wavelet shrinkage of noisy data," *Proceedings of 16th Annual International Conference of the IEEE Engineering in Medicine and Biology Society*, pp. 24a–25a, 1994.

[52] D. L. Donoho, "Nonlinear wavelet methods recovery of signal, densities, and spectra from indirect and noisy data," tech. rep., Departament of statistics, Santford University, 1993.

[53] S. Dangeti, *Denoising Techniques - A Comparison*. Msc thesis, Faculty of the Louisiana State University and Agricultural and Mechanical College in, 2003.

[54] D. L. Donoho and I. M. Johnstone, "Ideal Spatial Adaption by Wavelet Shrinkage," *Biometrika*, vol. 81, no. 3, pp. 425–455, 1994.

[55] D. L. Donoho and I. M. Johnstone, "Adapting to Unknown Smoothness via Wavelet Shrinkage," *Journal of American Statistical Association*, vol. 90, no. 432, pp. 1200–1224, 1995.

[56] I. Daubechies, *Ten lectures on wavelets*. Philadelphia, Pennsylvania: Society for Industrial and Applied Mathematics, 1992.

[57] E. Schneiders, "Wavelets in control engineering Dynamics and Control Technology Wavelets in control engineering," no. August, 2001.

[58] "Least-Squares Fitting [Online]." Available at http://www.mathworks.com/help/curvefit/least-squares-fitting.html [Accessed at 25 05 2016].

[59] "Trust-Region-Reflective Least Squares [online]." Available at: http://www.mathworks.com/help/optim/ug/least-squares-model-fitting-algorithms.html [Data Accessed 25 05 16].

[60] H. P. Garnir, Y. Baudinet-Robinet, and P. D. Dumont, "Error in the determination of Gaussian peak centroids," *Nuclear Inst. and Methods in Physics Research, B*, vol. 28, no. 1, pp. 146–153, 1987.

[61] A. C. Atkinson, *Plots, Transformations and Regression. An Intoduction to Graphical Methods of Diagnostic Regrssion Analysis*. Oxford statistical science series, 1988.

[62] J. Forrestal, "A compilation of Outgassing Data on Vacuum Materials," tech. rep., Princeton, 1982.

[63] J. Wiechula, P. Braun-Munzinger, H. Daues, U. Frankenfeld, C. Garabatos, J. Hehner, R. Renfordt, H. Schmidt, H. Stelzer, and D. Vranić, "High-precision measurement of the electron drift velocity in Ne–," *Nuclear Instruments and Methods in Physics Research Section A: Accelerators, Spectrometers, Detectors and Associated Equipment*, vol. 548, no. 3, pp. 582–589, 2005.

[64] C. Garabatos, "The ALICE TPC," *Nuclear Inst. and Methods in Physics Research, A*, vol. 535, no. 1-2, pp. 197–200, 2004.

[65] J. Alme et al, "The ALICE TPC, a large 3-dimensional tracking device with fast readout for ultra-high multiplicity events," *Nuclear Instruments and Methods in Physics Research, Section A: Accelerators, Spectrometers, Detectors and Associated Equipment*, vol. 622, no. 1, pp. 316–367, 2010.

[66] Y. Itikawa, "Cross sections for electron collisions with carbon dioxide," *Journal of Physical and Chemical Reference Data*, vol. 31, no. 3, pp. 749–767, 2002.

[67] V. G. Anicich, "Evaluated Bimolecular Ion-Molecular Gas Phase Kinetics of Positive Ions for Use in Modeling Planetary Atmospheres, Cometary Camae, and Interstellar Clouds," 1993.

[68] B. M. Smirnov, *Cluster Ions and Van der Waals Molecules*. Gordon and Breach Science Publishers, 1992.

[69] W. T. J. Huntress, "Ion Cyclotron Resonance Power Absorption: Collision Frequencies for CO_2^+, N_2^+ , and H_3^+ Ions in Their Parent Gases," *Chemical Physics Letters*, vol. 55, p. 2146, 1971.

[70] M. Saporoschenko, "Drift Velocities of O_2^+ , CO_2^+, and CO_4^+ions in CO_2 gas," *Phys. Rev. A*, vol. 8, p. 1044, 1973.

[71] P. A. Coxon and J. L. Moruzzi, "Positive Ion Mobilities in Carbon Dioxide," *Le Journal de Physique Colloques*, vol. 40, pp. C7–117–C7–118, 1979.

[72] G. Schultz, "Mobilities of Positive Ions in Some Gas Mixtures Used in Proportional and Drift Chambers," *Revue De Physique Appliquée*, vol. 12, no. January, pp. 67–70, 1977.

[73] H. W. Ellis, R. Y. Pai, I. R. Gatland, E. W. McDaniel, R. Wernlund, and M. J. Cohen, "Ion identity and transport properties in CO2 over a wide pressure range," *The Journal of Chemical Physics*, vol. 64, no. 1976, p. 3935, 1976.

[74] S. Rokushika, H. Hatano, and H. H. Hill, "Ion mobility spectrometry in carbon dioxide," *Analytical Chemistry*, vol. 58, pp. 361–365, 1986.

[75] R. Rejoub, B. G. Lindsay, and R. F. Stebbings, "Determination of the absolute partial and total cross sections for electron-impact ionization of the rare gases," *Physical Review A*, vol. 65, no. 4, p. 042713, 2002.

[76] C. Tian and C. R. Vidal, "Electron impact dissociative ionization of CO_2: Measurements with a focusing time-of-flight mass spectrometer," *The Journal of Chemical Physics*, vol. 108, no. 3, p. 927, 1998.

[77] W. Lindinger and D. L. Albritton, "Mobilities of various mass–identified positive ions in helium and argon," *J. Chem. Phys.*, vol. 62, p. 3517, 1975.

[78] H. Bohringer, M. Durup-Fergunson, and D. W. Fahey, "Mobilities of various mass–identified positive ions in helium, neon, and argon," *J. Chem. Phys.*, vol. 79, p. 1974, 1983.

[79] E. C. Beaty, "No Title," in *Fifth Int. Conf. Ionization Phenomena Gases*, (Munich), p. 183, 1961.

[80] W. Lindinger, I. Dotan, D. L. Albritton, and F. C. Fehsenfeld, "Reactions of N_4^+ with O_2, CO_2, H_2, and D_2 and mobilities of N_4^+ in nitrogen," *The Journal of Chemical Physics*, vol. 68, no. 6, p. 2607, 1978.

[81] K. Stephan, H. Helm, and T. D. Märk, "Mass spectrometric determination of partial electron impact ionization cross sections of He, Ne, Ar and Kr from threshold up to 180 eV," *J. Phys. Chem.*, vol. 73, no. 8, p. 3763, 1980.

[82] T. Koizumi, N. Kobayashi, and Y. Kaneko, "Mobilities of CO_2^+ and N_2O^+ Ions in Ne Gas," *Journal of Physical Society of Japan*, vol. 43, pp. 1817–1818, 1977.

[83] O. J. Orient, "Mobility of Mass-Identified Ions in Neon and Reaction Rate coefficient for $Ne^+ + 2Ne \rightarrow Ne_2^+ + Ne$," *Chemical Physics Letters*, vol. 23, no. 4, pp. 579–581, 1973.

[84] Y. Itikawa, "Cross sections for electron collisions with nitrogen molecules," *Journal of Physical and Chemical Reference Data*, vol. 35, pp. 31–53, 2006.

[85] I. Dotan, D. L. Albritton, W. Lindinger, and M. Pahl, "Mobilities of CO_2^+, N_2H^+, H_3O^+, $H_3O^+.H_2O$ and $H_3O^+.(H_2O)_2$," *J. Chem. Phys.*, vol. 65, no. 11, pp. 5028–5029, 1976.

[86] M. Saporoschenko, "Mobility of Mass-Analyzed N^+, N_2^+, N_3^+, and N_4^+ Ions in Nitrogen Gas," *Physical Review A*, vol. 139, no. 2A, pp. A352–A356, 1965.

[87] Y. Itikawa, "Cross sections for electron collisions with nitrogen molecules," *Journal of Physical and Chemical Reference Data*, vol. 35, no. 1, pp. 31–53, 2006.

[88] W. Lindinger, "Reactions of N_3^+ with NO and O_2 and mobility of N_3^+ in nitrogen," *The Journal of Chemical Physics*, vol. 64, no. 9, p. 3720, 1976.

[89] L. G. McKnight, K. B. McAfee, and D. P. Sipler, "Low-field drift velocities and reactions of nitrogen ions in nitrogen," *Physical Review*, vol. 164, no. 1, pp. 62–70, 1967.

[90] D. Rapp and P. Englander-Golden, "Total Cross Sections for Ionization and Attachment in Gases by Electron Impact. I. Positive Ionization," *The Journal of Chemical Physics*, vol. 43, no. 1965, p. 1464, 1965.

[91] I. Kondo and J. L. Moruzzi, "Mobilities of O_2^+, N_2^+ and CO^+ in Ar, Ne and Kr," *International Journal of Mass Spectrometry and Ion Physics*, vol. 38, pp. 1–10, 1981.

[92] A. Sharma and R. Veenhof, "Properties of some gas mixtures used in tracking detectors," *SLAC Journal, ICFA*, 1998.

[93] J. Miyamoto, I. Shipsey, C. J. Martoff, M. Katz-Hyman, R. Ayad, G. Bonvincini, and a. Schreiner, "GEM operation in negative ion drift gas mixtures," *Nuclear Instruments and Methods in Physics Research, Section A: Accelerators, Spectrometers, Detectors and Associated Equipment*, vol. 526, pp. 409–412, 2004.

Appendix A

Wavelets theory

The thresholded wavelet coefficients are obtained using either soft and thresholding rule given respectively the following equations and can be observed in figure A.1:

$$\eta_s(\omega,\mathrm{t}) = \begin{cases} \omega - t, & \omega \geq t \\ 0, & |\omega| < t \\ \omega + t, & \omega \leq -t \end{cases} \tag{A.1}$$

$$\eta_H(\omega,\mathrm{t}) = \begin{cases} \omega, & |\omega| \geq t \\ 0, & |\omega| < t \end{cases} \tag{A.2}$$

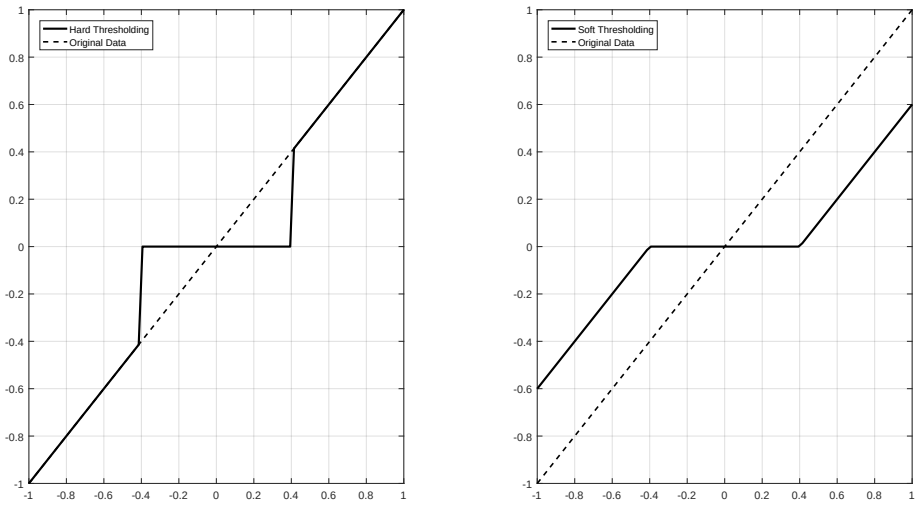

((a)) Hard thresholding ((b)) Soft thresholding

Figure A.1: Different types of thresholding

Appendix B

Data Compilation

B.1 Ar-CO_2

Table B.1: Mobility of the ions observed for the Ar-CO_2 mixture ratios of 70%, 80%, 85%, 90% and 95% of CO_2, obtained for different E/N and a pressure of 8 Torr at room temperature (298 K) and a voltage across the GEM of 18V.

Mixture	**Mobility ($cm^2V^{-1}s^{-1}$)**		**Ion**
	15 Td	**20 Td**	
5% CO_2 - 95% Ar	$1.858^{+}_{-}0.003$	$1.858^{+}_{-}0.005$	$CO_2^+.CO_2$
	$2.025^{+}_{-}0.003$	$2.05^{+}_{-}0.01$	H_2O^+
10% CO_2 - 90% Ar	$1.85^{+}_{-}0.009$	$1.85^{+}_{-}0.01$	$CO_2^+.CO_2$
	$2.21^{+}_{-}0.03$	$2.21^{+}_{-}0.04$	H_2O^+
15% CO_2 - 85% Ar	$1.635^{+}_{-}0.005$	$1.624^{+}_{-}0.004$	$CO_2^+.CO_2$
	$1.848^{+}_{-}0.006$	$1.81^{+}_{-}0.02$	H_2O^+
20% CO_2 - 80% Ar	$1.72^{+}_{-}0.01$	$1.71^{+}_{-}0.02$	$CO_2^+.CO_2$
	$1.90^{+}_{-}0.02$	$1.89^{+}_{-}0.03$	H_2O^+
30% CO_2 - 70% Ar	$1.546^{+}_{-}0.007$	$1.538^{+}_{-}0.003$	$CO_2^+.CO_2$

Table B.2: Mobility of the ions observed for the Ar-CO_2 mixture ratios of 5%, 10%, 15%, 20%, 30%, 50%, 70%, 80%, 85%, 90% and 95% of CO_2, obtained for different E/N and a pressure of 10 Torr at room temperature (298 K) and a voltage across the GEM of 25V.

Mixture	**Mobility ($cm^2V^{-1}s^{-1}$)**		**Ion**
	15 Td	**20 Td**	
5% CO_2 - 95% Ar	$1.883^{+}_{-}0.002$	$1.89^{+}_{-}0.02$	$CO_2^+.CO_2$
	$2.21^{+}_{-}0.01$	$2.23^{+}_{-}0.02$	H_2O^+
10% CO_2 - 90% Ar	$1.811^{+}_{-}0.002$	$1.802^{+}_{-}0.005$	$CO_2^+.CO_2$
	$2.10^{+}_{-}0.02$	$2.10^{+}_{-}0.02$	H_2O^+
15% CO_2 - 85% Ar	$1.746^{+}_{-}0.002$	$1.738^{+}_{-}0.003$	$CO_2^+.CO_2$
	$2.015^{+}_{-}0.004$	$2.010^{+}_{-}0.004$	H_2O^+
20% CO_2 - 80% Ar	$1.666^{+}_{-}0.007$	$1.663^{+}_{-}0.009$	$CO_2^+.CO_2$
	$1.91^{+}_{-}0.01$	$1.91^{+}_{-}0.01$	H_2O^+
30% CO_2 - 70% Ar	$1.547^{+}_{-}0.009$	$1.543^{+}_{-}0.009$	$CO_2^+.CO_2$
50% CO_2 - 50% Ar	$1.359^{+}_{-}0.004$	$1.354^{+}_{-}0.003$	$CO_2^+.CO_2$
70% CO_2 - 30% Ar	$1.24^{+}_{-}0.01$	$1.231^{+}_{-}0.009$	$CO_2^+.CO_2$
80% CO_2 - 20% Ar	$1.171^{+}_{-}0.003$	$1.164^{+}_{-}0.003$	$CO_2^+.CO_2$
85% CO_2 - 15% Ar	$1.134^{+}_{-}0.002$	$1.141^{+}_{-}0.002$	$CO_2^+.CO_2$
90% CO_2 - 10% Ar	$1.117^{+}_{-}0.004$	$1.109^{+}_{-}0.002$	$CO_2^+.CO_2$
95% CO_2 - 5% Ar	$1.094^{+}_{-}0.002$	$1.085^{+}_{-}0.002$	$CO_2^+.CO_2$

B.2 N_2-CO_2

Table B.3: Mobility of the ions observed for the 90% N_2 - 10% CO_2 obtained for different E/N and pressures at room temperature (298 K).

Mixture	Mobility ($cm^2V^{-1}s^{-1}$)			Ion
	15 Td	20 Td	25 Td	
4 Torr	$1.95^{+}_{-}0.03$	$1.95^{+}_{-}0.03$	$1.93^{+}_{-}0.05$	CO_2^+
	2.11	2.09	-	?
8 Torr	$1.85^{+}_{-}0.03$	$1.87^{+}_{-}0.04$	-	$CO_2^+.CO_2$
	$1.95^{+}_{-}0.02$	$1.98^{+}_{-}0.02$	-	CO_2^+
12 Torr	-	$1.89^{+}_{-}0.05$	$1.87^{+}_{-}0.02$	$CO_2^+.CO_2$
	$1.94^{+}_{-}0.03$	$1.93^{+}_{-}0.02$	$1.95^{+}_{-}0.02$	CO_2^+
16 Torr	$1.94^{+}_{-}0.02$	$1.91^{+}_{-}0.05$	$1.90^{+}_{-}0.05$	$CO_2^+.CO_2$ or CO_2^+?
20 Torr	$1.92^{+}_{-}0.03$	$1.89^{+}_{-}0.05$	-	$CO_2^+.CO_2$?

B.3 TMA

Table B.4: Mobility of the ions observed for pure TMA at room temperature (300 K) for different E/N and pressures between 0.5 to 3 Torr.

E/N (Td)	Mobility ($cm^2V^{-1}s^{-1}$)
$10.0^{+}_{-}0.2$	$0.96^{+}_{-}0.02$
$14.6^{+}_{-}0.2$	$0.80^{+}_{-}0.06$
$19.8^{+}_{-}0.4$	$0.75^{+}_{-}0.04$
$24.5^{+}_{-}0.1$	$0.68^{+}_{-}0.06$
$29.6^{+}_{-}0.3$	$0.65^{+}_{-}0.06$
$34.4^{+}_{-}0.1$	$0.64^{+}_{-}0.05$
$39.0^{+}_{-}0.5$	$0.63^{+}_{-}0.03$
$44.3^{+}_{-}0.1$	$0.61^{+}_{-}0.05$
$50^{+}_{-}1$	$0.60^{+}_{-}0.04$

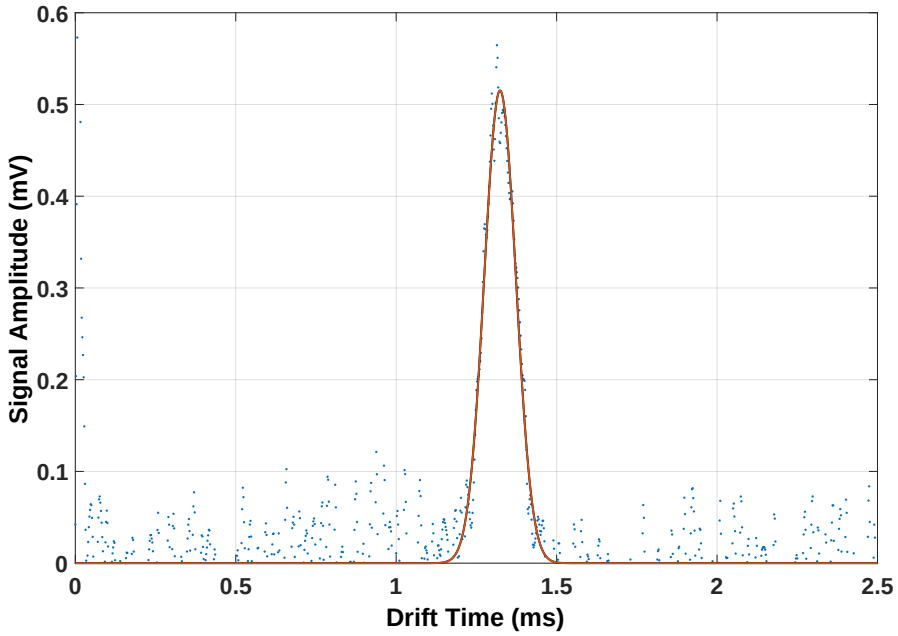

Figure B.1: Time-of-arrival spectra for pure TMA at a pressure of 2 torr and for a reduced electric field of 15 Td with a voltage across GEM of 36 V at room temperature

B.4 Xe-TMA

Table B.5: Mobility of the ions observed for the Xe-TMA mixtures obtained for different E/N between 10 and 15 Td and for pressure of 8 Torr pressure at room temperature (298 K). In the case of pure TMA the mobilities values were obtained for pressure between 0.5 and 3 Torr

Mixture	**Mobility ($cm^2V^{-1}s^{-1}$)**		**V_{GEM}**	**Ion**
	$10^{+}_{-}0.2$	**$15^{+}_{-}0.2$**		
100% TMA	$0.96^{+}_{-}0.02$	$0.80^{+}_{-}0.06$	36 V	?
90% Xe - 10% TMA	$0.795^{+}_{-}0.005$	0.78	19 V	?
95% Xe - 5% TMA	$0.82^{+}_{-}0.01$	$0.80^{+}_{-}0.01$		
98% Xe - 2% TMA	$0.823^{+}_{-}0.005$	$0.813^{+}_{-}0.005$		
99% Xe - 1% TMA	$0.827^{+}_{-}0.008$	$0.813^{+}_{-}0.004$		
99.5% Xe - 0,5% TMA	$0.831^{+}_{-}0.02$	$0.82^{+}_{-}0.01$		
99.8% Xe - 0.2% TMA	$0.832^{+}_{-}0.007$	$0.817^{+}_{-}0.006$		
100 % Xe	$0.661^{+}_{-}0.007$	$0.653^{+}_{-}0.007$	19 V	Xe_2^+ [4]

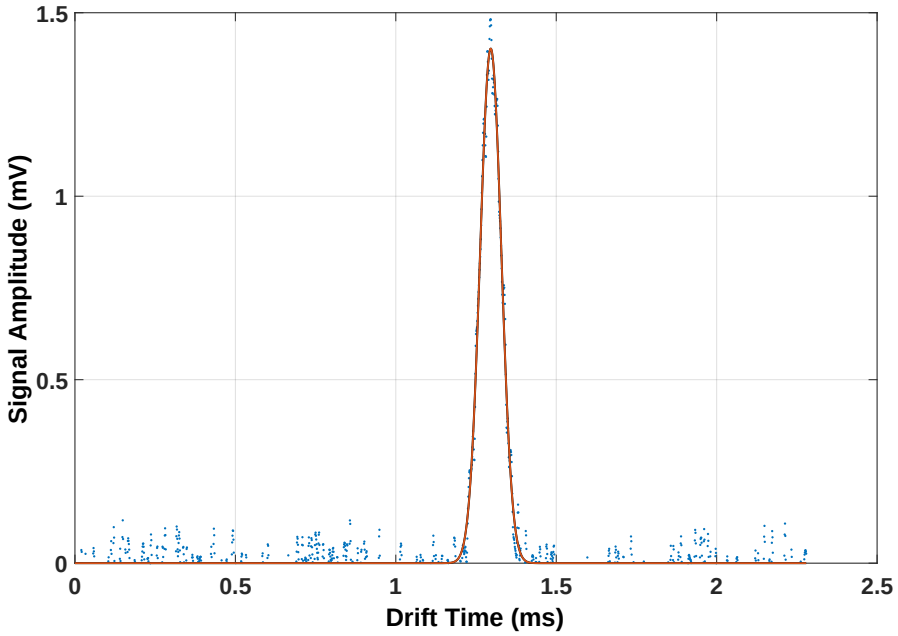

Figure B.2: Time-of-arrival spectra for 95% Xe - 5% TMA at a pressure of 8 Torr and for a reduced electric field of 15 Td with a voltage across GEM of 19 V at room temperature